Search for Randall-Sundrum Gravitons in Dielectron and Diphoton Final States with 5.4 fb^{-1} of DØ Data

Ning Zhou

Advisor: Professor John Parsons

Submitted in partial fulfillment of the
requirements for the degree
of Doctor of Philosophy
in the Graduate School of Arts and Sciences

COLUMBIA UNIVERSITY

2010

ABSTRACT

Search for Randall-Sundrum Gravitons in Dielectron and Diphoton Final States with 5.4 fb^{-1} of DØ Data

Ning Zhou

A search for the lightest Kaluza-Klein mode of the graviton in the Randall-Sundrum model with a warped extra dimension is performed in the dielectron and diphoton channels. The data set used for the search corresponds to 5.4 fb^{-1} of data from $p\bar{p}$ collisions at a center-of-mass energy of 1.96 TeV, collected with the DØ detector at the Fermilab Tevatron between July 2002 and Summer 2009. We search for resonances in the invariant mass spectrum of two electromagnetic showers from the decay of the graviton to either electron-positron pairs or photon pairs. To optimise the sensitivity, the dielectron and diphoton channels are analyzed separately, then the results are combined together in the end. We also investigate whether, due to the unique spin-2 nature of the graviton, the angular distribution of the final state particles can be used to significantly enhance the sensitivity of the search. We set 95% confidence level upper limits on the graviton production cross section times branching fraction into electron-positron pairs of between ~ 7 fb and ~ 0.5 fb for a range of graviton masses from 220 GeV and 1050 GeV, respectively. Compared with Randall-Sundrum model predictions, these results correspond to lower limits on the lightest graviton mass between 440 GeV and 1040 GeV, for the dimensionless graviton coupling to the Standard Model fields $k/\overline{M}_{\mathrm{Pl}}$ in the range from 0.01 to 0.1. In addition, for coupling $k/\overline{M}_{\mathrm{Pl}}$ of 0.01, gravitons with masses between 460 GeV and 560 GeV are also excluded at 95% confidence level. These results represent the most sensitive limits to date.

Table of Contents

1 Introduction 2

1.1 The Standard Model 2

1.1.1 Fermions 3

1.1.2 Gauge Bosons 6

1.1.3 Fundamental Interactions 6

1.2 Limitations of the Standard Model 8

2 The Randall-Sundrum Model 10

2.1 The Hierarchy Problem and Extra Dimension Models 10

2.2 Randall-Sundrum model 11

2.3 Graviton Kaluza-Klein modes 13

2.4 Collider Signals 14

2.5 Current Constraints 18

3 Apparatus 22

3.1 The Tevatron 22

3.2 The DØ Detector 25

3.2.1 Coordinate System 26

3.2.2 Tracking System 28

3.2.3 Preshower Detectors 31

3.2.4 Calorimeter 33

3.2.5 Intercryostat Detector 37
3.2.6 Muon Spectrometer 38
3.2.7 Luminosity Monitor 38
3.2.8 Trigger and Data Acquisition System 39

4 Data Reconstruction **41**
4.1 Track Reconstruction 41
4.2 Vertex Reconstruction 44
4.3 Electromagnetic Object Reconstruction 44
4.4 Jet Reconstruction 50
4.5 Muon Reconstruction 51
4.6 Missing Transverse Energy 51

5 Data Samples and Event Selection **52**
5.1 Dataset 52
5.2 Simulated Samples 54
5.3 Event Selection 61
5.4 Primary Vertex Selection 71

6 Graviton Signal Studies **75**

7 Background Estimation and Systematic Uncertainties **85**
7.1 Shapes of the Physics Background Distributions 86
7.2 Shapes of the Instrumental Background Distributions 88
7.3 Normalization of the Backgrounds 91
7.4 Systematic Uncertainties 96

8 Results **104**

9 Summary and Conclusions **111**

Bibliography **112**

A Test of Two-Dimensional Reweighting to DIPHOX Events **120**

B Backup Plots **124**

C Other Versions of the Limit Plots **133**

D Angular distribution **136**

List of Figures

2.1 Schematic view of Randall-Sundrum model. 12
2.2 Leading order Feynman diagrams for virtual graviton exchange in e^+e^- and $\gamma\gamma$ channels. 14
2.3 Contributions of quark-antiquark annihilation and gluon-gluon fusion to RS graviton production at the Tevatron. 15
2.4 RS graviton production at the Tevatron. 15
2.5 Graviton branching fractions in the Randall-Sundrum model. 17
2.6 Angular distributions for graviton production and decay. 19
2.7 Previous DØ published 95% CL limits. 19
2.8 Previous CDF published 95% CL limits. 21

3.1 Schematic of Fermilab accelerator chain. 23
3.2 The DØ detector side-view. 26
3.3 The DØ coordinate system. 27
3.4 Side view of the central tracking system. 28
3.5 3-D view of the silicon microstrip tracker. 30
3.6 Diagrams illustrating the layers of scintillating fibers in the CFT. . . 30
3.7 DØ preshower detector. 32
3.8 3-D view of the DØ calorimeter. 34
3.9 Diagram showing calorimeter towers in η. 35
3.10 Readout chain of the calorimeter. 37
3.11 Side view of the luminosity monitor. 38

3.12 Overview of the DØ trigger and data acquisition systems. 40

4.1 Schematic view of the calorimeter isolation. 46
4.2 Normalized distributions of iso and $emfrac$ variables. 47
4.3 Normalized distributions of $IsoHC4$, $sigphi$, $HMx7$, $NN7$, $NN5$ variables. 49

5.1 Trigger efficiency for v15 and v16 diEM triggers. 54
5.2 Invariant mass distribution of PhiFiducial and NonPhiFiducial events. 62
5.3 Scale factor of “MLoose1” selection for electrons. 65
5.4 Two-body and three-body invariant mass distributions for p17 $\mu\mu\gamma$ events. 66
5.5 Two-body and three-body invariant mass distributions for p20 $\mu\mu\gamma$ events. 66
5.6 Electron “notrk” efficiency and scale factor in p17. 69
5.7 Electron “notrk” efficiency and scale factor in p20. 70
5.8 Electron “notrk” efficiency as a function of physics η in p20. 71
5.9 Data/MC scale factors for $NN5 > 0.1$ cut in p17 and p20. 72
5.10 Three vertex selection algorithms in 500 GeV $G^* \to \gamma\gamma$ MC sample. . 74

6.1 The generated and reconstructed invariant mass spectra for RS graviton of 500 GeV and $k/\overline{M}_{\rm Pl} = 0.02$. 77
6.2 Various distributions for 500 GeV $G^* \to e^+e^-$ events. 78
6.3 Various distributions for 500 GeV $G^* \to \gamma\gamma$ events. 79
6.4 Signal acceptance and EM ID efficiency 80
6.5 Saturation effects in different calorimeter layers of electrons from 1 TeV graviton decay. 82
6.6 Saturation effects on dielectron invariant mass distribution for 500 GeV, 700 GeV and 1050 GeV gravitons. 83

6.7 A Gaussian fitted mean and sigma of the reconstructed diEM invariant mass distribution with and without corrections for saturation effects. 84

7.1 The SM $\gamma\gamma$ and e^+e^- production Feynman diagrams simulated in PYTHIA. 85
7.2 The NNLO k-factor used for the DY e^+e^- process. 86
7.3 Differential cross sections for SM $\gamma\gamma$ production from PYTHIA and DIPHOX. 87
7.4 Variation of $\gamma\gamma$ invariant mass from different scale choices in DIPHOX calculations. 89
7.5 Systematic uncertainty from DIPHOX scale choices on the total expected background. 90
7.6 Comparison between RESBOS and DIPHOX predictions for the SM $\gamma\gamma$ invariant mass spectrum. 90
7.7 Ratio between fraction of jet-faked clusters passing electron ID cuts and that of failing H-matrix cut from p17 data. 91
7.8 Ratio between fraction of jet-faked clusters passing electron ID cuts and that of failing H-matrix cut from p20 data. 92
7.9 Ratio between fraction of jet-faked cluster passing photon ID cuts and that of failing $NN5$ cut from p17 data. 92
7.10 Ratio between fraction of jet-faked cluster passing photon ID cuts and that of failing $NN5$ cut from p20 data. 93
7.11 Results of the fit of the backgrounds to the data in the control region for Category I. 95
7.12 Results of the fit of the backgrounds to the data in the control region for Category II. 97
7.13 95% CL expected exclusion limit from 1.1 fb^{-1} of data, as compared to the previous published results. 98
7.14 Variation of background estimate in Category I p17 and p20. 101

7.15 Variation of background estimate in Category II p17 and p20. 103

8.1 Invariant mass spectrum for data and expected total background in Category I and II. 105
8.2 95% CL upper limit on $\sigma \cdot BR(p\bar{p} \to G^* \to e^+e^-)$ and $k/\overline{M}_{\rm Pl}$ versus graviton mass 109

9.1 RS graviton discovery potential of ATLAS experiment. 113

A.1 2D weighting ($M_{\gamma\gamma}$) vs $p_T^{\gamma\gamma}$, and DIPHOX/PYTHIA comparison after mass only weighting or mass-p_T 2D weighting. 121
A.2 Leading and subleading p_T, $q_T^{\gamma\gamma}$ and $\Delta\phi^{\gamma\gamma}$ distributions for p17 Category II events after the 2-D weighing. 122
A.3 Leading and subleading p_T, $q_T^{\gamma\gamma}$ and $\Delta\phi^{\gamma\gamma}$ distributions for p20 Category II events after the 2-D weighing. 123

B.1 p17 Category I invariant mass spectrum. 125
B.2 Various distributions for p17 Category I events. 126
B.3 p17 Category II invariant mass spectrum. 127
B.4 Various distributions for p17 Category II events. 128
B.5 p20 Category I invariant mass spectrum. 129
B.6 Various distributions for p20 Category I events. 130
B.7 p20 Category II invariant mass spectrum. 131
B.8 Various distributions for p20 Category II events. 132

C.1 95% CL exclusion limit from 1.1 fb^{-1} of data, as compared to the previous published results. 133
C.2 95% CL exclusion limit from 5.4 fb^{-1} of data for Category I, Category II separately and the combination of the two categories. 134
C.3 95% CL exclusion limit from 5.4 fb^{-1} of data separately for statistical errors only and for full (i.e. statistical plus systematic) errors. 134

C.4 95% CL exclusion limit from 5.4 fb^{-1} of data separately for including saturation effects and for neglecting saturation effects. 135

D.1 Angular distribution for CC-CC events in Category I and II. 137
D.2 95% CL exclusion limit for using only invariant mass distribution and for using both the mass and angular distributions. 138

List of Tables

1.1 Properties of leptons. 4

1.2 Properties of quarks. 5

1.3 Properties of gauge bosons. 6

2.1 Angular distributions in graviton production and decay. 18

3.1 Properties of CC layers 36

5.1 Dataset definitions used in this analysis. 53

5.2 Integrated luminosity for different trigger versions. 53

5.3 Calorimeter-only diEM triggers for RunIIa used in this analysis. . . . 55

5.4 Calorimeter-only diEM triggers used for RunIIb in this analysis. . . . 56

5.5 DØ official MC signal samples used in the analysis. 56

5.6 List of graviton MC samples simulated. 58

5.7 DØ official p17 MC background samples used in the analysis. 59

5.8 DØ official p20 MC background samples used in the analysis. 60

5.9 Fraction of CC-CC, CC-EC and EC-EC events. 63

5.10 Efficiency and scale factor for photon in Category I selection. 66

5.11 Efficiencies and scale factors of electron and photon Calo and IsoTrk cuts for p17 and p20. 67

5.12 Efficiency and scale factor for photon “NoTrk” after Calo and TrkIso Cuts. 68

5.13 Efficiencies and scale factors of photon NN cut for p17 and p20. . . . 68

5.14 Efficiency and scale factor for electron “NoTrk” after Calo and TrkIso Cuts. 69
5.15 Efficiencies and scale factors of electron NN cut for p17 and p20. . . . 70

6.1 Natural width and mass resolution for signal samples. 76
6.2 Selection efficiency for a 500 GeV graviton for p17. 77
6.3 Selection efficiency for a 500 GeV graviton for p20. 80

7.1 Number of events in the data in the low-mass control region and the fitted normalization of the various backgrounds for both Category I and Category II. 96
7.2 Sources of systematic uncertainties for signal and expected background 98
7.3 Uncertainty of signal acceptance and cross section due to pdf’s for the various graviton mass points 99

8.1 Number of data and background events for various mass windows for Category I and II. 104
8.2 Number of data and background events for Category I and II. 106
8.3 95% CL expected and observed upper limits on cross section × branching ratio and coupling. 108

Acknowledgments

I would like to thank my adviser John Parsons for his invaluable guidance, insights, great ideas, patience, and constant support and motivation. It was a pleasure to work under his supervision, and I learned a lot from him, and I'm sure this knowledge will help me in my professional career. I am grateful to Gustaaf Brooijmans, for his help and fruitful discussions during my graduate study. I would also like to extend my thanks to the other Columbia professors on the ATLAS and DØ experiments, Michael Tuts, Emlyn Hughes, for their help and guidance.

I am grateful to Columbia University faculty members and staff for their support and help. In particular, I would like to thank my physics group colleagues at Columbia - Kamal Benslama, Seth Caughron, Mark Cooke, Katherine Copic, Dominik Dannheim, Thomas Gadfort, Heather Gray, Andrew Haas, Zach Marshall, David Lopez Mateos, Michael Mulhearn, Alex Penson, Kerstin Perez, Valeria Perez Reale, Francesco Spano, Dustin Urbaniec, Eric Williams, Evan Wulf and Lidija Živković.

Much thanks is owed to the ATLAS and DØ Collaborations and staffs for supplying the resources that made this research possible. I would like to express my gratitude to all my ATLAS and DØ colleagues that I have closely worked with in the past years.

I would like to thank all my friends I met throughout these years at Columbia, CERN and FNAL (too many to mention all their names here). Without them my life in these three places would not be that memorable.

Finally, I would like to thank my parents for their everlasting love, support and guidance.

To my parents.

Foreword

I joined the Columbia ATLAS group in 2005. As hardware work, I participated in the assembly and testing of the Front End Boards for the readout of the ATLAS Liquid Argon Calorimeters at Nevis Labs, which is documented in Publications [1; 2; 3]. At the same time, I studied in the ATLAS e/γ combined performance group, mainly working on electron identification algorithms and performances, electron energy resolution, the development of electromagnetic object identification in the ATLAS forward region beyond the inner detector acceptance, and the extrapolation of electron identification to very high transverse energies. These developments are documented in ATLAS Note [4; 5; 6]. In terms of ATLAS physics analysis, I studied the ATLAS sensitivity for Randall-Sundrum gravitons decaying to electron pairs at 14 TeV and 10 TeV center-of-mass energies, the results of which are documented in ATLAS Note [7].

In February 2009, I moved to the DØ experiment to perform a search for Randall-Sundrum gravitons in electron pairs and photon pairs. The results obtained are the most sensitive to date, and this work is documented in DØ Note [8] and in a paper about to be submitted for publication in Physical Review Letters, and is the topic of this thesis. During this peroid, I worked within the EM ID group and took part in measuring the photon identification efficiency from the data and determining the corresponding scale factors between the data and the Monte Carlo simulation, this work is documented in DØ Note [9].

Chapter 1

Introduction

Particle physics is a branch of physics that studies the elementary constituents of matter and the interactions between them. The idea that all matter is composed of elementary particles dates back to ancient times. The current knowledge of elementary particles and their interactions is summarized in the so-called *Standard Model* (SM). However, the SM is not a complete theory for many reasons, which stimulates the ongoing efforts in finding and understanding what physics may lie beyond the SM. This dissertation contains the results of a search for evidence of the possible existence of extra dimensions, one possible extension to the SM.

1.1 The Standard Model

The SM [10; 11; 12; 13] of particle physics, formulated in the 1970s, is a theory of elementary particles and their fundamental interactions except for gravity: electromagnetic interactions, weak interactions and strong interactions. In the SM, elementary particles are classified into two categories: fermions and bosons. Fermions have half integer intrinsic spin and make up all the visible matter in the universe (leptons and quarks). Each fermion has its corresponding anti-particle with the same mass and opposite electric charge. Interactions between these particles are mediated by gauge bosons carrying integer spin. The SM contains two major theories - quantum electroweak and quantum chromodynamics, which provide internally consistent theories describing the electroweak force (unification of electromagnetic force and weak force) and strong force. Technically, quantum field theory provides the mathematical framework and the SM is a non-abelian gauge theory with a symmetry group $\mathrm{SU}(3)\otimes\mathrm{SU}(2)\otimes\mathrm{U}(1)$. Each type of particles is described in terms of a mathematical field, and mass is generated in the so-called "Higgs Mechanism" by introducing a scalar field (the Higgs boson). To date, many experimental tests of the three forces described by the SM have agreed with its predictions. However, the Higgs boson has not been observed yet. Moreover, recent experiments show that the neutrino leptons have non-zero masses, while they are described as massless in the SM.

1.1.1 Fermions

In particle physics, fermions are particles which obey Fermi-Dirac statistics. The known elementary fermions are divided into two groups: leptons and quarks. Leptons include the electron and similar, heavier particles (the muon and tau); they also include neutrinos. Quarks make up protons, neutrons and other baryons, which are composite fermions; they also comprise mesons, which are composite bosons.

1.1.1.1 Leptons

Leptons are spin-1/2 elementary particles, carrying integral electric charge in units of the elementary electric charge (the negative of the electric charge carried by a single electron, denoted e). Leptons are subject to the electromagnetic force, gravitational force and weak force, but do not participate in the strong interaction. There are six flavors of leptons, falling into three generations. Each generation is composed of a massive charged lepton and a massless neutral lepton, the neutrino, and is associated with a lepton flavor number. The properties of the leptons are summarized in Table 1.1. The first generation consists of the electron (e^-) and electron neutrino (ν_e)

Table 1.1: Properties of leptons, showing the charge (e), mass (MeV/c^2) and anti-particle [16].

	Particle	Charge (e)	Mass (MeV/c^2)	Anti-particle
1st generation	e^-	-1	0.511	e^+
	ν_e	0	< 0.000002	$\bar{\nu}_e$
2nd generation	μ^-	-1	105.7	μ^+
	ν_μ	0	< 0.19	$\bar{\nu}_\mu$
3rd generation	τ^-	-1	1776.8	τ^+
	ν_τ	0	< 18.2	$\bar{\nu}_\tau$

with electron number L_e, the second generation of the muon (μ^-) and muon neutrino (ν_μ) with muon number L_μ, the third generation of the tau (τ^-) and tau neutrino (ν_τ) with tau number L_τ. In the SM, each lepton flavor number L_e, L_μ, L_τ is strictly conserved, +1 for each lepton and -1 for each antilepton of the appropriate flavor. Of all the fundamental fermions, neutrinos ν are unique in that there are no right-handed neutrinos, they are massless particles corresponding to the pure helicity state $H = -1$. Their antiparticle, the antineutrinos $\bar{\nu}$, are right-handed. (The helicity of a particle is the direction of its spin relative to its momentum; particles with spin in the same direction as their momentum are called "right-handed" and otherwise they are called "left-handed".) Recent experiments indicate that the neutrinos do have non-zero mass [14; 15] and there is mixing in the neutrino sector, which implies that there may exist right-handed neutrinos and lepton flavor numbers are not exactly conserved in weak interactions.

1.1.1.2 Quarks

Quarks carry fractional charges, of $+2/3$ or $-1/3$ of the elementary electric charge. They have spin 1/2, and they are the only particles in the SM to experience all four fundamental forces. There are six flavors of quarks known as the up quark (u),

Table 1.2: Properties of quarks showing the charge (e), current mass (MeV/c^2) and anti-particle [16].

	Particle	Charge(e)	Flavor Number	Mass(MeV/c^2)	Anti-particle
1st generation	u	$+2/3$	–	$1.5 - 3.3$	$\bar{u}$
	d	$-1/3$	–	$3.5 - 6.0$	$\bar{d}$
2nd generation	c	$+2/3$	$C = +1$	1270	$\bar{c}$
	s	$-1/3$	$S = -1$	104	$\bar{s}$
3rd generation	t	$+2/3$	$T = +1$	171200	$\bar{t}$
	b	$-1/3$	$B = -1$	4200	$\bar{b}$

down quark (d), strange quark (s), charm quark (c), bottom quark (b), top quark (t), grouped into three generations, (u, d), (c, s), (t, b). The properties of the quarks are given in Table 1.2. In strong interactions between the quarks, the flavor quantum number, denoted by the initial of the quark name in capitals S (strangeness), C (charmness), B (bottomness), T (topness) is conserved. Particles in higher generations generally have greater mass and are less stable, tending to decay into lower-generation, less massive particles via weak interactions, which is also true for the lepton generations.

Unlike leptons, quarks are always found in bound states referred to as *hadrons*. There are two types of combinations established as existing in nature: baryons qqq (three quark state) and mesons $q\bar{q}$ (quark-antiquark pair). This phenomenon is described as quark confinement. Besides the spin, there exists a second internal quantum number, “color”, which is the “charge” of the strong interaction. Quarks exist in three colors (red r, green g and blue b), baryons and mesons have zero net color, i.e. they are color singlets.

Table 1.3: The elementary gauge bosons in the SM [16].

Gauge Boson	Force	Spin	Mass (GeV/c^2)	Charge (e)
Photon (γ)	Electromagnetic	1	0	0
$W^{\pm}$	Charged Weak	1	80.398 ± 0.025	± 1
Z^0	Neutral Weak	1	91.1876 ± 0.0021	0
Gluon (g)	Strong	1	0	0

1.1.2 Gauge Bosons

The interactions of elementary particles are described in quantum language in terms of the exchange of characteristic bosons, the quanta of the gauge fields. There are three kinds of gauge bosons: photon, W and Z bosons and gluons, each corresponding to one of the three SM interactions. The properties of the gauge bosons are summarized in Table 1.3. For the electromagnetic interaction described by Quantum Electrodynamics, the photon (γ) is the mediator corresponding to the generator of the U(1) gauge group. The $W^{\pm}$ and Z^0 bosons correspond to the three generators of SU(2) of the weak interaction. In Quantum Chromodynamics with the SU(3) symmetry, there are eight generators, gluons (g), carrying the strong interaction. The photon and gluons are massless particles, therefore the forces that they describe are long-ranged. The weak force is short-ranged due to the non-zero masses of $W^{\pm}$ and Z^0 bosons. According to the SM, the $W^{\pm}$ and Z^0 bosons gain mass via the Higgs mechanism.

1.1.3 Fundamental Interactions

Quantum electrodynamics (QED) describes the interaction of charged particles by the exchange of photons with symmetry group $\mathrm{U}(1)_{\mathrm{em}}$. The coupling constant specifying the strength of the interaction between charged particles and photons is the dimensionless quantity

$$\alpha = \frac{e^2}{4\pi\epsilon_0\hbar c} = \frac{1}{137.0360\ldots} \tag{1.1}$$

called the fine structure constant, where $\hbar = h/(2\pi)$ is the reduced Planck constant, c is the speed of light in vacuum and ϵ_0 is the electric constant. Since the coupling constant $\alpha \ll 1$, the magnitude of these interactions can be computed using perturbation theory. Predictions of QED agree with experiments to an accuracy of $\sim 10^{-12}$ limited by some theoretical and experimental errors, which makes QED the most accurate physical theory constructed so far.

In the SM, the electromagnetic interaction and the weak interaction are unified into the electroweak model. Although these two forces appear different at low energy, they are two different aspects of the same force, and above the unification energy ($\sim 10^3$ GeV) they merge into a single electroweak force. Mathematically, the unification is accomplished under an $\mathrm{SU}(2)\otimes\mathrm{U}(1)$ gauge group. The corresponding gauge bosons are the photon of QED and the $\mathrm{W}^{\pm}$ and Z^0 bosons of the weak interaction. The weak gauge bosons get their masses from the spontaneous symmetry breaking of the electroweak symmetry caused by the Higgs mechanism. However, the existence of the Higgs boson associated in this theory has not been verified yet. Thus far experimental searches for the SM Higgs boson have provided a lower limit on its mass $m_H > 114.4$ GeV/c^2 at 95% confidence level (CL) [16].

Quantum Chromodynamics (QCD) is the gauge field theory describing the strong interactions of the quarks and gluons. A three-fold color degree of freedom is introduced to explain the hadron spectroscopy, and QCD is based on $\mathrm{SU}(3)_{color}$ non-Abelian gauge symmetry group, which introduces eight massless vector fields, the gluons. A quark of specific flavor comes in 3 colors, red, blue or green; and antiquarks carry anticolor. The mediator of the strong interaction, gluons, carry a color and an anticolor. Since they are themselves colored, gluons have self-interaction (the non-Abelian nature of QCD), which marks a crucial difference from QED. Emission of a gluon may lead to a quark changing color, but the color of the entire system is conserved.

1.2 Limitations of the Standard Model

The SM describes the physics of strong, weak and electromagnetic interactions with precision to energies of order 100 GeV, or distances as small as 10^{-17} cm. In spite of all the successes of the SM, it is unlikely to be the final theory, since it leaves many unanswered questions. Gravitational interactions are not included. In the SM, neutrinos are assumed to be massless, but recent experiments show that neutrinos do have finite masses. Moreover, the SM fails to answer questions such as why fermions have the masses they do, the origin of flavor, what makes up dark matter, and the large matter-antimatter asymmetry of the universe. The SM has 19 arbitrary parameters; their values are chosen to fit the data. Also the SM only unifies two of the four interactions. It is widely believed that the SM is an effective theory, a low-energy approximation of a more complete theory.

In the SM, there is a so-called "Hierarchy Problem" about different energy scales, namely the question of why there exists a large disparity between the electroweak symmetry breaking scale (~ 1 TeV, related to Fermi's constant G_F) and the Planck scale ($\sim 10^{16}$ TeV, related to Newton's constant G_N), or equivalently why the weak force is 10^{32} times stronger than gravity, $G_F/G_N = 10^{32}$. In the calculation of quantum corrections to Fermi's constant, Fermi's constant is unnaturally large unless there is a delicate cancellation between the bare value of Fermi's constant and the quantum corrections to it.

Traditionally, new symmetries, particles, or interactions have been introduced at the electroweak scale to stabilize this hierarchy. For instance, supersymmetry removes the power-law divergences of the quantum corrections by postulating "superpartners" for all the SM particles which have contribution with opposite sign to that from their SM partners. Other proposals for resolving the SM hierarchy problem include extra dimensional models, which postulates the existence of additional spacetime dimensions. These models are described in more detail in the next chapter.

Chapter 2

The Randall-Sundrum Model

2.1 The Hierarchy Problem and Extra Dimension Models

Recently it was realized that extra dimensions with a fundamental scale of order TeV^{-1} could address the hierarchy problem. If spacetime is fundamentally higher dimensional with $4+n$ spacetime where n is the number of extra spatial dimensions, the four-dimensional view of gravity does not represent nature and the Planck scale we observe is not truly fundamental, but only an effective four-dimensional value. The effective four-dimensional reduced Planck scale, $\overline{M}_{\text{Pl}} = M_{\text{Pl}}/\sqrt{8\pi} = 2.4 \times 10^{18}$ GeV, is determined by the fundamental $(4+n)$-dimensional Planck scale M and the geometry of the extra dimensions. These scenarios include models with flat extra dimensions and warped extra dimensions.

For instance, in flat compactified extra dimensional spacetime with finite volume V_n, the apparent hierarchy is generated by

$$\overline{M}_{\text{Pl}}^2 = \overline{M}^{n+2} V_n, \tag{2.1}$$

where M is considered as the fundamental $4+n$-dimensional Planck mass. Setting $M \sim$ TeV to remove the hierarchy, we would have a very large compact space, with the compactification scale $\mu_c = 1/r_c \sim 1/V_n^{1/n}$ at eV-MeV for $n = 2 - 7$. In this framework, gravity is weak because it is diluted in a large space ($r_c \gg M^{-1}$).

Randall and Sundrum (RS) proposed a warped extra dimensional scenario [17], where the universe is described as $4+n$-dimensional non-factorizable spacetime with warped geometry. The hierarchy is generated by a warp factor, an exponential function of the compactification radius.

2.2 Randall-Sundrum model

In the minimal RS model, a five-dimensional geometry is assumed, in which the fifth dimension is compactified with length πr_c, where r_c is the compactification radius of the extra dimension. Each end-point of the segment (the “fixed-points” of the orbifold projection) is the location of a three-dimensional brane. The two branes have equal but opposite tensions. The negative-tension brane is referred as the infrared (IR) brane or “weakbrane”, where the SM fields are assumed to be localized. Gravity originates from the other 3-brane, with positive tension, referred as the ultraviolet (UV) brane or “gravitybrane”. In this configuration, the 5-dimensional Einstein equations permit a solution which preserves 4-dimensional Poincaré invariance with the metric

$$ds^2 = e^{-2k|y|}\eta_{\mu\nu}dx^\mu dx^\nu - dy^2, \tag{2.2}$$

where x^μ denote coordinates for the ordinary 4-dimensional spacetime, $y = r_c\phi$ is the 5^{th} coordinate, and the UV and IR branes are located at $y = 0$ and $y = \pi r_c$. Here k is the curvature scale , which is of order the Planck scale.

Examination of the action in the 4-dimensional effective theory yields the relation

$$\overline{M}^2_{\mathrm{Pl}} = \frac{M_5^3}{k}(1 - e^{-2kr_c\pi}) \tag{2.3}$$

for the reduced 4-dimensional Planck scale, where M_5 is the 5-dimensional Planck scale. Any mass parameter m_{IR} on the IR brane will correspond to a physical mass

$$m_{IR} = e^{-kr_c\pi} m_{UV} \tag{2.4}$$

in the fundamental higher-dimensional theory. TeV scales are thus generated from fundamental scales of order $M_{\rm Pl}$ via this warp factor and the scale of physical processes on the weakbrane is then $\Lambda_\pi \equiv \overline{M}_{\rm Pl} e^{-kr_c\pi}$. The observed scale hierachy is reproduced if $kr_c \simeq 11 - 12$. It has been demonstrated [18] that such a value of kr_c can be stabilized without fine tuning of parameters by minimizing the potential for the modulus field which describes the relative motion of the two branes. In this approach, the graviton ground state wave function is peaked around the UV brane and it has an exponentially small overlap with the IR brane where we live, as shown schematically in Figure 2.1, which produces the Planck scale.

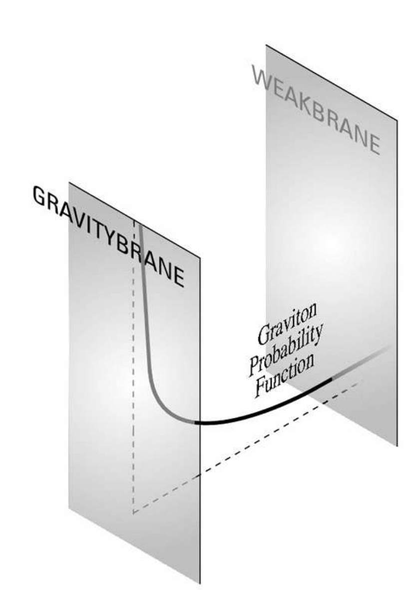

Figure 2.1: Schematic view of Randall-Sundrum model where the graviton is the only particle propagating in the extra dimension.

The four-dimensional phenomenology of this model is governed by only two parameters, given by the curvature k and Λ_π. Additionally, the 5^{th} dimensional curvature is restricted to be small compared to M_5 with $M_5 \sim \overline{M}_{\rm Pl}$ and the solution for the bulk metric can be trusted. This implies that the ratio $k/\overline{M}_{\rm Pl}$ cannot be too large, $k/\overline{M}_{\rm Pl} \leq 1$. Using string theoretic arguments, one could estimate the natural size of this parameter, $k/\overline{M}_{\rm Pl} \sim 10^{-2}$ [19]. These considerations suggest the range of graviton coupling $0.01 \leq k/\overline{M}_{\rm Pl} \leq 0.1$.

2.3 Graviton Kaluza-Klein modes

In the extra compactified dimension, a Kaluza-Klein (KK) [20] [21] tower is expected, as an analogy of standing waves. With an extra dimension of radius R, the energy of such a standing wave would be $E = n\hbar c/R$, with n an integer, $\hbar$ Planck's constant and c the speed of light. More specifically, in the construction of the RS model considered here, only gravity could propagate in the 5th-dimension. The masses of the graviton KK excitations are yielded as

$$m_n = k x_n e^{-kr_c\pi}, \tag{2.5}$$

where x_n is the $n^{\rm th}$ root of the Bessel function J_1 ($x_1 = 3.83$, $x_2 = 7.02$ and for large n, $x_n = (n + 1/4)\pi$). Note that the masses are not equally spaced. All the massive KK states are only suppressed by Λ_π^{-1}, which is of order the weak scale.

KK graviton production cross-sections and decay width are set by the first KK mass m_1 and the graviton-matter interaction scale Λ_π of order the weak scale, which implies that these KK states can be separately produced on resonance with observed rates at high energy colliders.

In this paper, we choose m_1 and $k/\overline{M}_{\rm Pl}$ as the independent parameters. The relationships between these parameters are

$$\frac{m_n}{\Lambda_\pi} = \frac{k x_n}{\overline{M}_{\rm Pl}}, \qquad \Lambda_\pi = \overline{M}_{\rm Pl}\rm exp(-kr_c\pi) \tag{2.6}$$

2.4 Collider Signals

The KK excitations of the gravitons are strongly coupled at the weak scale with a mass gap of $\sim$ TeV size. They can be produced resonantly at the Tevatron through quark-antiquark annihilation or gluon-gluon fusion, and would subsequently decay to pairs of SM fermions or bosons. For example, the Feynman diagrams for virtual graviton exchange in the dielectron and diphoton channels considered in this analysis are shown in Figure 2.2.

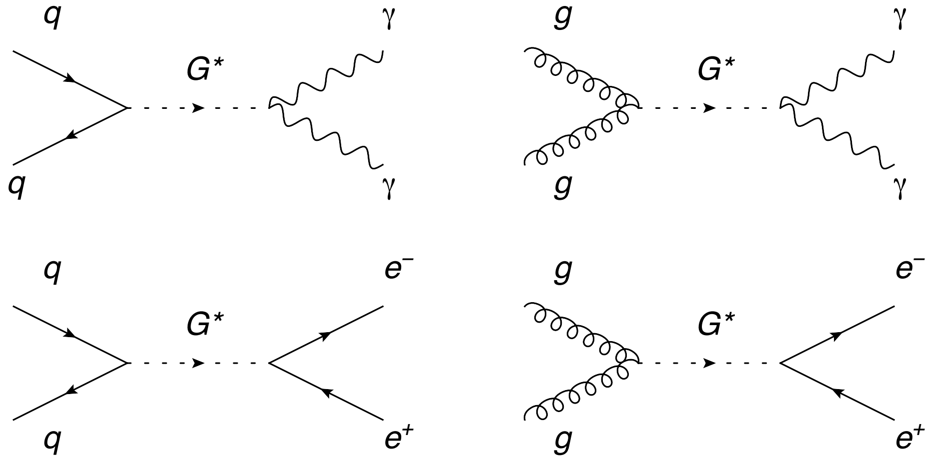

Figure 2.2: Leading order Feynman diagrams for virtual graviton exchange in the dielectron and diphoton channels.

The contributions from quark-antiquark annihilation and gluon-gluon fusion at the Tevatron proton-antiproton collider are shown in Figure 2.3. Quark-antiquark annihilation dominates the cross section for graviton masses above 200 GeV, since the gluon parton distribution function $f(x)$ is smaller than that of the valence quarks for the larger values of the momentum fraction x that are required to produce heavy gravitons.

The graviton signature is a series of heavy resonances, Kaluza-Klein excitations with separation among each other of order TeV. Figure 2.4 shows the first excitation of 700 GeV as would be seen at the Tevatron.

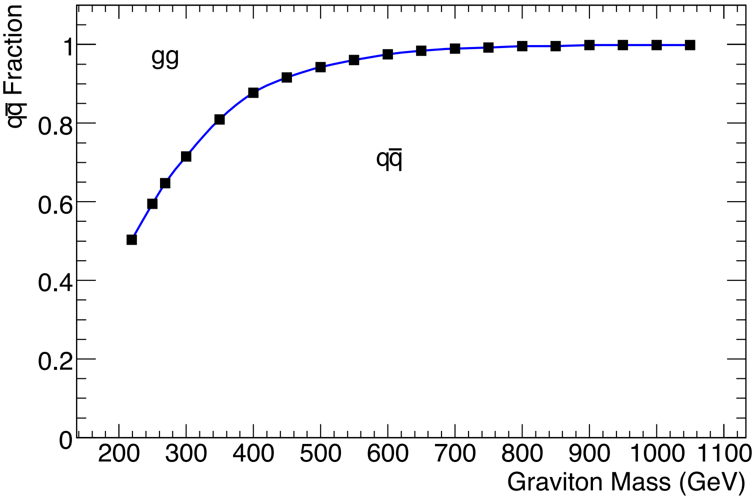

Figure 2.3: Contributions of quark-antiquark annihilation and gluon-gluon fusion to RS graviton production at the Tevatron, as a function of graviton mass, simulated in Pythia [22].

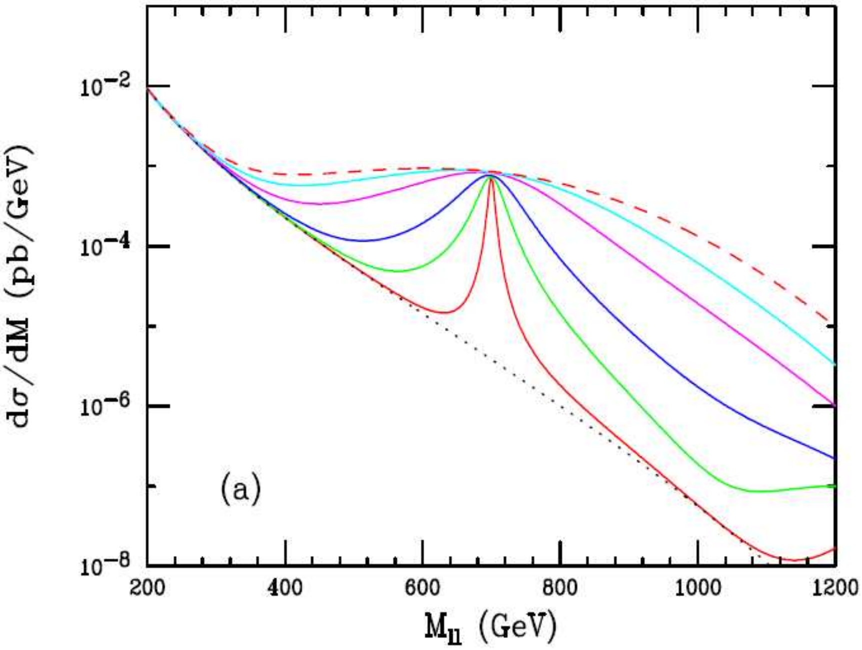

Figure 2.4: Production cross-section for 700 GeV RS graviton at the Tevatron with $k/\overline{M}_{\rm Pl}$=1.,0.7,0.5,0.3,0.2 and 0.1 respectively from top to bottom [23].

As described, the masses (m_n) of the resonances depends on the parameter m_1 with $m_n = x_n/x_1 \cdot m_1$. The graviton natural width is a function of m_1 and $k/\overline{M}_{\mathrm{Pl}}$. For the first excitation, the lightest mode, the model assumes that it only decays into the SM states, with width given by

$$\Gamma_1 = \rho m_1 x_1^2 (k/\overline{M}_{\mathrm{Pl}})^2, \tag{2.7}$$

where ρ is a constant depending on the number of decay channels available, a fixed value. Equation 2.7 shows that the resonance width increases with graviton mass and is proportional to the coupling squared. For the range of widths considered ($0.01 \leq k/\overline{M}_{\mathrm{Pl}} \leq 0.1$), the resolution of the DØ detector dominates the intrinsic width of the first excitation in dielectron and diphoton decay channels. For instance, the intrinsic width of a RS graviton with mass of 500 GeV and coupling of 0.02 is ~ 300 MeV, while the mass resolution reconstructed in the dielectron channel is 11.2 ± 0.1 GeV.

A striking property of the KK graviton is its universal couplings to all types of matter and gauge fields. The KK graviton decay branching fractions are shown in Figure 2.5. These predictions are rather model-independent, depending only on the universality of the coupling. The decays into quark and gluon jets are predominant due to the high multiplicity of color, spin and flavor states. In this paper, the decay channels $G^* \rightarrow e^+e^-$ and $G \rightarrow \gamma\gamma$ are chosen for study, considering the good energy and angular resolution for high energy electromagnetic objects. As seen in Figure 2.5, the diphoton branching ratio is twice that of dileptons. This arises from the different spins of bosons and fermions and the fact that the graviton has a spin of 2.

The spin-2 nature of the graviton can be used to distinguish it from the SM backgrounds and other possible new physics, such as a Z' boson. The expected decay angular distributions are shown in Table 2.1. β represents the velocity of the decay products, $\beta = \sqrt{1 - 4m^2/m_G^2}$ for particles of mass m. One defines θ^* as the angle in the center-of-mass (CM) reference frame between the outgoing particle and the incident quark or gluon. Parity-violating couplings for the Z' can lead to a forward-

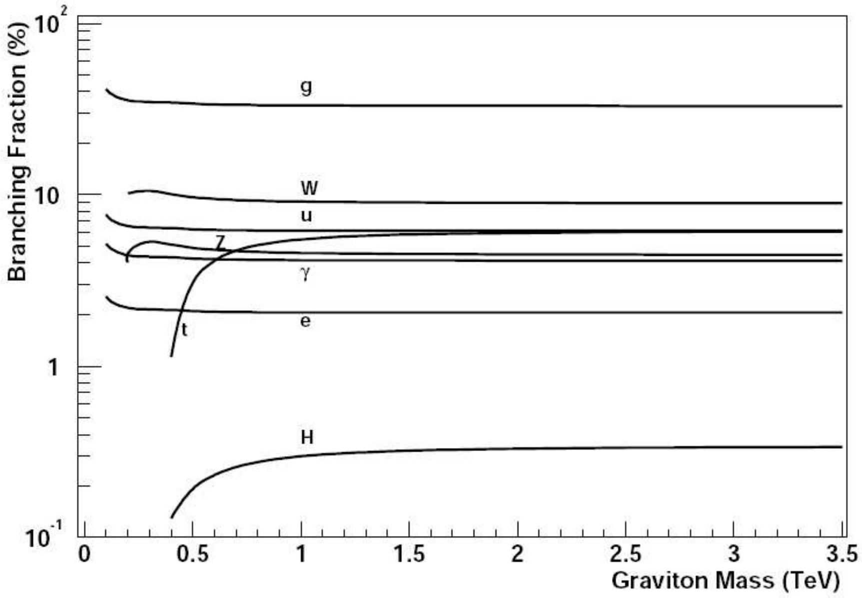

Figure 2.5: Graviton branching fractions in the Randall-Sundrum model, as a function of the graviton mass [24].

backward asymmetry due to a non-zero coefficient of cosθ^* in the angular distribution. In this analysis, we focus on the information contained in terms with even powers of cosθ^*. In Table 2.1, the plot letters refer to Figure 2.6, which shows the distributions in the limit of negligible decay particle mass ($\beta = 1$). The angular distribution is strongly related to the production mechanism. For instance, at the Tevatron, which is a proton-antiproton collider, the main irreducible background in the dielectron channel is Drell-Yan (DY) production via a vector boson γ^*/Z with

$$\frac{\mathrm{d}\sigma}{\mathrm{d}\ \mathrm{cos}\theta^*} \sim 1 + \cos^2\theta^*. \tag{2.8}$$

In the diphoton channel, the main irreducible background is QCD direct diphoton production, for which the leading order contribution is given by the Born level process $q\bar{q} \rightarrow \gamma\gamma$. The spin-1/2 quark propagator in this process produces a characteristic behavior

$$\frac{\mathrm{d}\sigma}{\mathrm{d}\ \mathrm{cos}\theta^*} \sim \frac{1}{1 - |\mathrm{cos}\theta^*|}. \tag{2.9}$$

The graviton production which is dominated by quark-antiquark annihilation gives

$$\frac{\mathrm{d}\sigma}{\mathrm{d}\ \cos\theta^*} \sim 1 + \cos^2\theta^* - 4\sin^2\theta^*\cos^2\theta^* \tag{2.10}$$

for the dielectron channel and

$$\frac{\mathrm{d}\sigma}{\mathrm{d}\ \cos\theta^*} \sim 1 - \cos^4\theta^* \tag{2.11}$$

for the diphoton channel.

Table 2.1: Angular distributions in graviton production and decay, where θ^* is the polar angle of the outgoing decay particles in the graviton rest frame. The letters in the “plot” columns refer to the curves in Figure 2.6.

Process	Distribution	Plot
$gg \to G^* \to f\bar{f}$	$\sin^2\theta^*(2 - \beta^2\sin^2\theta^*)$	a
$q\bar{q} \to G^* \to f\bar{f}$	$1 + \cos^2\theta^* - 4\beta^2\sin^2\theta^*\cos^2\theta^*$	b
$gg \to G^* \to \gamma\gamma$	$1 + 6\cos^2\theta^* + \cos^4\theta^*$	c
$q\bar{q} \to G^* \to \gamma\gamma$	$1 - \cos^4\theta^*$	a
$q\bar{q} \to \gamma^*/Z^0/Z' \to f\bar{f}$	$1 + \cos^2\theta^*$	d

2.5 Current Constraints

Constraints on the RS model come from theoretical restrictions, as previously mentioned and from direct searches. Direct graviton searches with proton-antiproton collisions were performed by the DØ and CDF experiments. Figure 2.7 shows the previous DØ limits on RS graviton production, as a function of graviton mass and coupling $k/\overline{M}_{\mathrm{Pl}}$. The solid line is the experimental limit obtained from the combination of the dielectron and diphoton channels using 1 fb^{-1} of data. Lower limits on the mass of the first massive RS graviton are set at 95% CL at 300 GeV for $k/\overline{M}_{\mathrm{Pl}} = 0.01$ and 900 GeV for $k/\overline{M}_{\mathrm{Pl}} = 0.10$ [25].

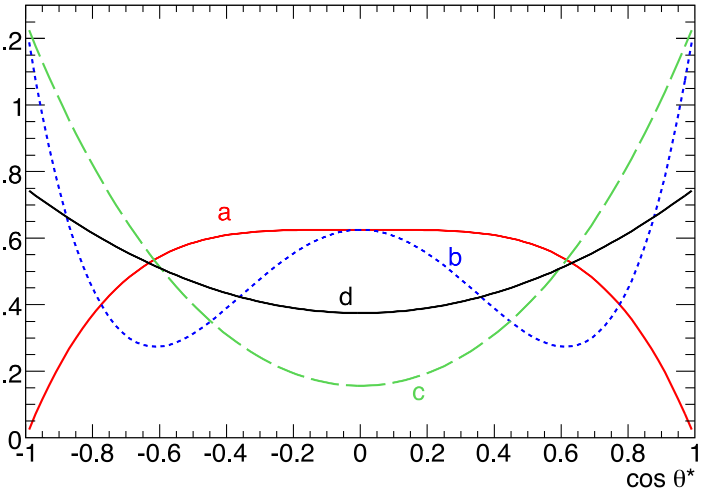

Figure 2.6: Angular distributions for graviton production and decay in the limit of negligible decay particle mass $\beta = 1$, normalized to 1.

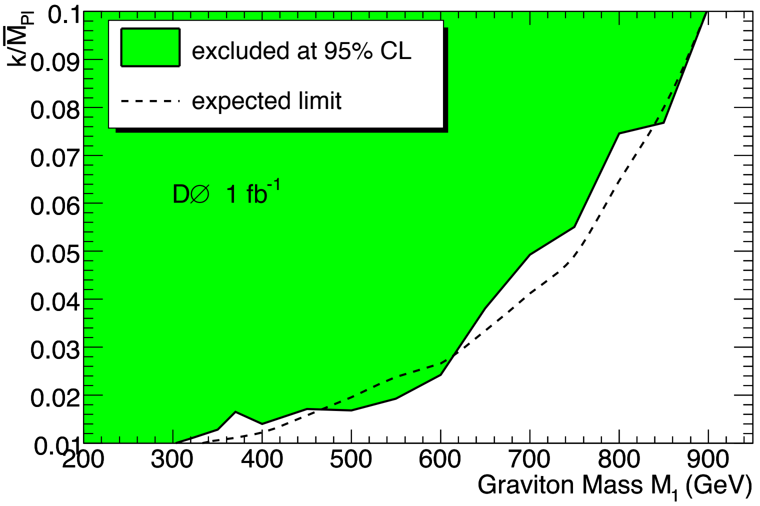

Figure 2.7: 95% CL upper limits from the DØ on $k/\overline{M}_{\mathrm{Pl}}$ versus graviton mass M_1 from 1 fb^{-1} of data compared with the expected limit.

The previous CDF experimental constraints are shown in Figure 2.8. These limits are from dielectron (2.5 fb^{-1}) [26] and diphoton (1.2 fb^{-1}) [27] channels respectively. In the diphoton channel, lower limits on the graviton mass of 230 GeV and 850 GeV at 95% CL were set for coupling parameters $k/\overline{M}_{\text{Pl}}$ of 0.01 and 0.1 respectively. In the dielectron channel, the lower graviton mass limit is 850 GeV for a coupling of 0.1.

This analysis extends the search in dielectron and diphoton channel, using 5.4 fb^{-1} of data at DØ experiment.

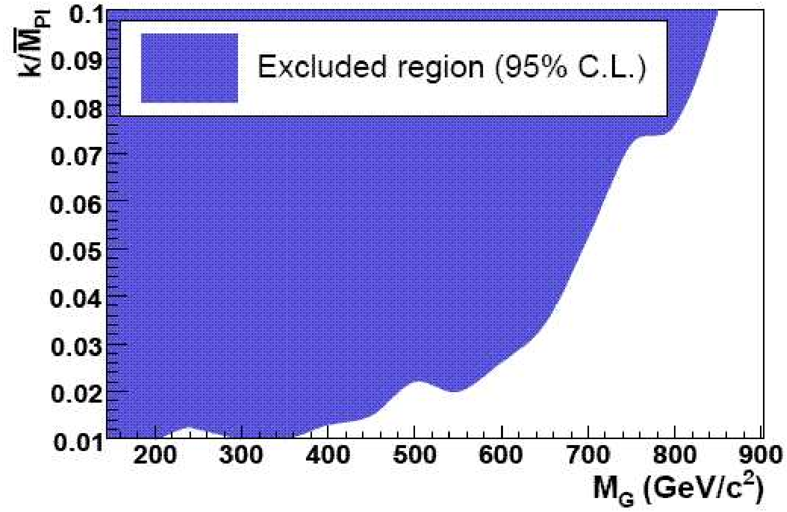

(a) dielectron

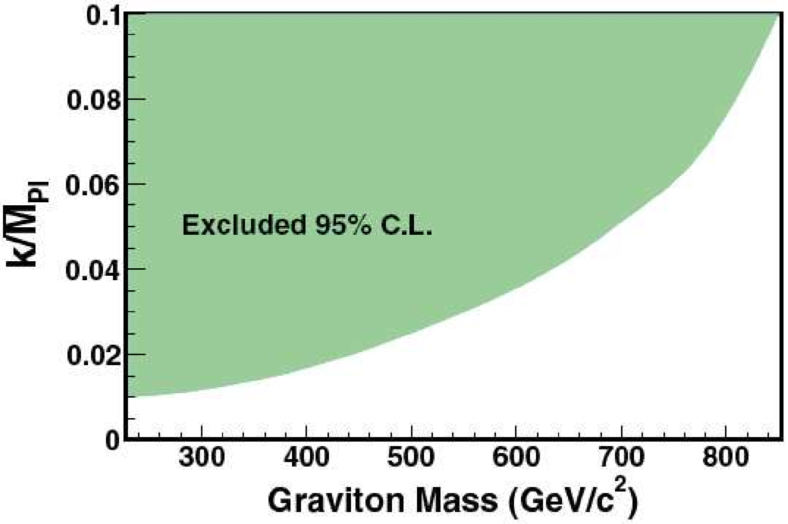

(b) diphoton

Figure 2.8: 95% CL upper limits from the CDF on $k/\overline{M}_{\mathrm{Pl}}$ versus graviton mass M_1 from 2.5 fb^{-1} of data in dielectron channel (a) and 1.2 fb^{-1} of data in diphoton channel (b).

Chapter 3

Apparatus

The Fermi National Accelerator Laboratory (Fermilab) [28] hosts the Tevatron Accelerator [29][30], a proton-antiproton ($p\bar{p}$) collider designed to produce high energy collisions at a center of mass energy of approximately 1.96 TeV [30]. There are two multipurpose detectors designed to study the secondary particles coming from these proton-antiproton collisions, DØ and CDF. This analysis is based on the data collected by the DØ experiment, which is described in detail below.

3.1 The Tevatron

The Tevatron Accelerator Complex is made of several different accelerator systems. The Cockcroft-Walton, Linac and Booster are collectively known as the Proton Source. The Debuncher and Accumulator are referred to as the Antiproton Source. The Main Injector and the Tevatron, which are the largest systems, complete this machine. An illustration of the integrated system is shown in Figure 3.1.

The first stage of the acceleration complex is the Cockcroft-Walton accelerator, where negatively ionized hydrogen gas (H^-) is produced and accelerated to an energy of 750 KeV with high positive voltage. The 750 keV hydrogen ions then enter a linear accelerator (LINAC), in which the oscillating electric fields in the radio frequency

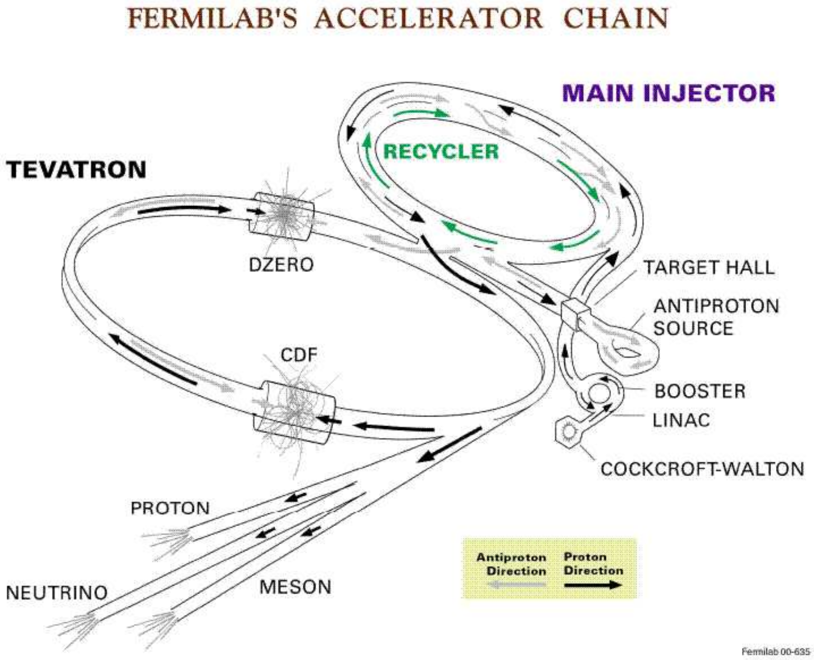

Figure 3.1: Schematic of Fermilab accelerator chain.

(RF) cavities accelerate the ions to 400 MeV. The first five RF stations use drift tube technology and the last seven use Klystron amplifiers. With the length of the LINAC of about 150 meters, the acceleration gradient is roughly 2.7 MeV per meter. The ions then pass through a thin carbon foil at the end of the LINAC, that strips off two electrons from the ions, and leaves only protons.

The protons from the LINAC are sent to the Booster, a circular accelerator that uses magnets to keep the protons in a circular orbit. With each of about 20,000 revolutions, protons pass through the electric field that gradually boosts their energy until the protons reach an energy of about 8 GeV. The Booster is the first synchrotron in the chain of accelerators, and consists of a series of magnets arranged around a 75 m radius circle, with 18 RF cavities interspersed. The Main Injector (MI) is the second largest accelerator at Fermilab. It is a circular synchrotron with a circumference seven times larger than that of the Booster. With its 18 accelerating cavities, the MI can accelerate 8 GeV protons from the Booster to 120 GeV or 150 GeV, depending on whether the protons are used to stack antiprotons or to inject beam into the Tevatron synchrotron.

When creating antiprotons, protons in the MI are accelerated to 120 GeV and are sent to the antiproton source where they collide with a nickel target, which produces a spray of all sorts of secondary particles, including some antiprotons. Magnets are used to select antiprotons that have an energy of approximately 8 GeV, and the antiprotons are directed to the Debuncher. The main purpose of the Debuncher is to capture pulses of antiprotons coming off the target and reduce their momentum spread by using an RF manipulation scheme called bunch rotation and adiabatic debunching. After about 100 ms the Debuncher produces a continuous beam of antiprotons with a small spread in energy around 8 GeV. The antiproton beam is then transferred to the Accumulator which stores and cools 8 GeV antiprotons. The Accumulator is the second synchrotron of the antiproton source and is housed in the same tunnel as the Debuncher. After many transfers from the Debuncher the Accumulator fills up to the point where adding more antiprotons to the Accumulator becomes increasingly inefficient. Once full, the Accumulator empties the antiprotons into the Recycler and begins accumulating again. The Recycler is an antiproton storage ring located along the ceiling of the MI tunnel, which is used only to store antiprotons at a constant kinetic energy of 8 GeV. When it comes time for a new store (round of collisions), the antiprotons are transfered from the Recycler to the MI where they are accelerated from 8 GeV to 150 GeV.

36 bunches of protons and antiprotons, each consisting of more than 10^{10} particles, are injected into the Tevatron ring in opposite directions and are accelerated to the energy of 980 GeV, traveling at almost the speed of light. Powerful dipole magnets bend the particles' trajectories in the beam pipe to keep them in the circular orbits, and quadrupole magnets are used to focus the beams and compress them to about 30 microns in radius. Both types of magnets are cooled down to the temperature of liquid helium to sustain the multi-thousand amperes currents flowing through their

coils, i.e. are superconducting. With the circumference of the Tevatron ring of 6.28 km, the proton and antiproton bunches collide in the two high-luminosity interaction points every 396 ns. Low beta magnets installed at both ends of the two collider detectors are used to focus the beams and create the collisions in the middle of the detectors: the CDF and DØ detectors.

The instantaneous luminosity is the measure of the collision rate per unit area per unit time, usually measured in $\mathrm{cm}^{-2}\mathrm{s}^{-1}$. It is proportional to the number of particles in two colliding bunches n_1 and n_2, the collision rate f, and inversely proportional to the overlapping transverse area of the beams $\sigma_x\sigma_y$:

$$L = f \cdot \frac{n_1 n_2}{4\pi\sigma_x\sigma_y}. \tag{3.1}$$

The highest achieved instantaneous luminosity to date at the Tevatron is roughly 360×10^{30} $\mathrm{cm}^{-2}\mathrm{s}^{-1}$, and is the world's highest instantaneous luminosity ever achieved at a hadron collider. The integrated luminosity is defined as the instantaneous luminosity summed over time, and is measured in units of cm^{-2}, or more commonly, in inverse barns, b^{-1}, where $1\mathrm{b}^{-1} = 10^{-24}$ cm^{-2}. The analysis described here uses a data set corresponding to 5.4 fb^{-1} of integrated luminosity.

3.2 The DØ Detector

The DØ detector [31][32][33] operating at the Tevatron is a multipurpose system with dimensions of approximately 18 m × 12 m × 10 m. Figure 3.2 shows a side-view of the detector with all the main components.

The central tracking system includes a silicon microstrip tracker and a scintillating-fiber tracker located within a 2 T solenoidal magnet. The tracker provides the capability for precise measurements of particles' positions along their path from the interaction point. The next layer of detectors are the preshower system and liquid-argon-uranium calorimeter, which accurately measure the energy of most particles.

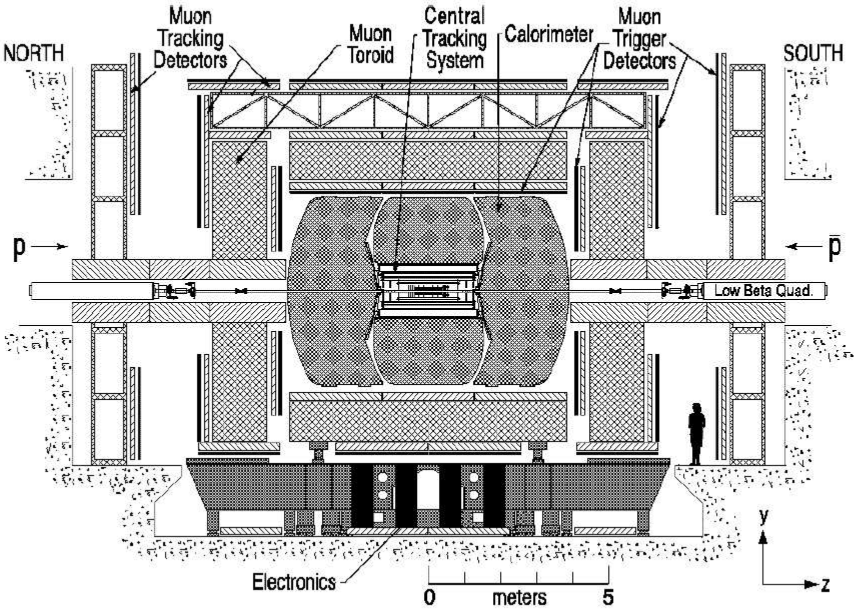

Figure 3.2: The DØ detector side-view.

The muon spectrometer lies outside the calorimeter and uses drift tubes and scintillation counters, as well as a 1.8 T toroidal magnet, to identify and measure the momentum of muons.

To measure the luminosity, the luminosity monitor measures the inelastic $p\bar{p}$ cross section in order to determine the total integrated luminosity to which the DØ detector has been exposed.

3.2.1 Coordinate System

The DØ experiment uses a right-handed coordinate system, shown in Figure 3.3, which is defined such that the protons move along the z-axis and the antiprotons move in the opposite direction. The center of the detector is used as the origin of the coordinate system. The z coordinate is defined as the distance along the beam line, with the y-axis pointing upwards. The azimuthal angle, ϕ, is measured with respect to the x-axis of the detector in the $x-y$ plane, and varies from 0 to 2π. The polar

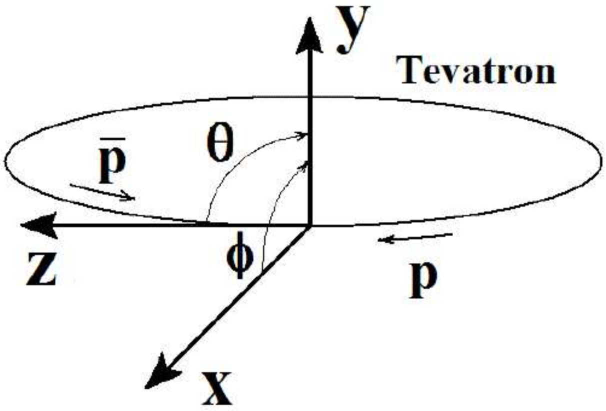

Figure 3.3: The DØ coordinate system.

angle, θ, is measured with respect to the z-axis in the $z - y$ plane. Additionally, the rapidity, y is another common way to describe the kinematics of a particle and is defined as:

$$y = \frac{1}{2}\ln\frac{E + p_L}{E - p_L} = \tanh^{-1}(\beta_L), \tag{3.2}$$

where E is the energy of the particle, p_L is the longitudinal component of the momentum along the z-axis, and the β_L is the longitudinal component of the speed of the particle relative to the speed of light. When the momentum of the particle is large enough to neglect the mass of the particle, rapidity transforms into another variable, called *pseudorapidity*, η:

$$\eta = \frac{1}{2}\ln\frac{|\vec{p}| + p_L}{|\vec{p}| - p_L} = -\ln[\tan(\frac{\theta}{2})], \tag{3.3}$$

where $\vec{p}$ is the total momentum of the particle. Rapidity and pseudorapidity are dimensionless functions, and the main advantage of their usage is that the difference in the rapidity of two particles is independent of the Lorentz boost along the beam axis. Another Lorentz boost invariant variable is the spatial separation of two particles, ΔR, defined as:

$$\Delta R = \sqrt{\Delta\phi^2 + \Delta\eta^2}, \tag{3.4}$$

where $\Delta\phi$ and $\Delta\eta$ are the differences of the corresponding variables of the two particles.

The transverse energy and momentum, E_T and p_T, of particles are defined as:

$$E_T = E\sin\theta, \text{ and } p_T = \sqrt{p_x^2 + p_y^2}. \tag{3.5}$$

The coordinates calculated using the detector origin (0,0,0) are referred to as "detector coordinates". Proton-antiproton collisions do not usually coincide exactly with the center of the detector coordinate system. Additionally, the magnetic fields in the detector will curve the paths of charged particles. The coordinates defined with respect to the location of the actual interaction point are called "physics coordinates".

3.2.2 Tracking System

The tracking system is comprised of the silicon microstrip tracker (SMT), central fiber tracker (CFT), and 2 T superconducting solenoid, as shown in Figure 3.4. The main purpose of the tracking system is to provide momentum measurements and vertexing.

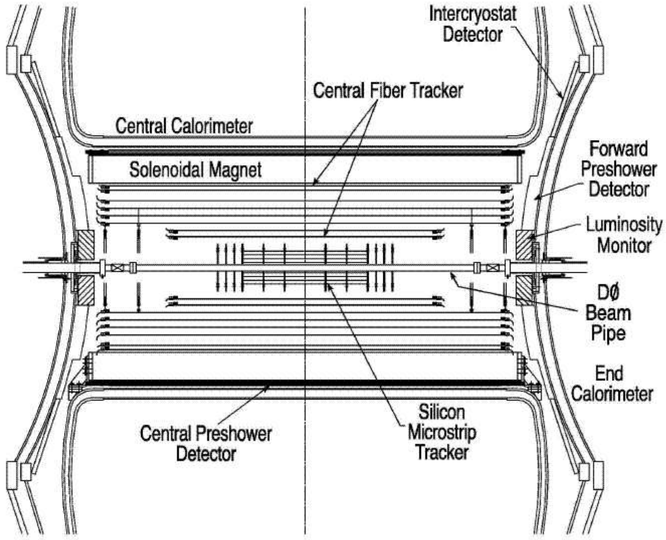

Figure 3.4: Side view of the central tracking system.

The SMT [34][35] is the closest to the beam pipe of the central tracking system, it is a collection of doped silicon detectors. When charged particles pass through the doped silicon, ionizing radiation produces free electrons and holes. Under the influence of an electric field, electrons and holes travel to the electronodes, where they result in a pulse that can be measured in an outer circuit.

The SMT consists of several modules: six barrels and twelve F-disks in the central region, and four H-disks in the forward region, as shown in Figure 3.5. The inner (outer) radii of the barrels, F-disks and H-disks are: 2.7 (10.5) cm, 2.6 (10.0) cm, and 9.5 (26.0) cm, respectively. Each barrel segment is 12 cm long and contains four concentric cylindrical layers of microstrip detectors, two single-sided layers and two double-sided layers. The double-sided layers have one axial side (microstrips oriented parallel to the beam line) giving the azimuthal position of tracks, and one stereo side making an angle of 2^o or 90^o with respect to the beam line and providing a measurement of track pseudorapidity. The single-sided barrel layers are axial. The centers of the barrels are located at $|z|$ = 6.2, 19.0 and 31.8 cm. At higher $|z|$, each barrel is capped with an F-disk. The F-disks are made from 12 wedges of double-sided microstrip detectors, with each side offset by an angle of 15^o from radial. The centers of the F-disks are located at $|z|$ =12.5, 25.3, 38.2, 43.1, 48.1, and 53.1 cm. The H-disks are made from two layers of 12 single-sided microstrip detectors with each layer offset by 7.5^o from radial, located at $|z|$ = 100.4 and 121.0 cm. With the H-disks, the SMT provides precise tracking and vertexing for pseudorapidity up to $|\eta| < 3$. The typical resolution of the track position measurement is on the order of 10 μm. The SMT is kept at temperatures below 5^o C to minimize radiation damage to the silicon.

The CFT [36] combines with the SMT detector to provide charged particle tracking. The CFT is composed of eight concentric cylinders ranging in radius from 20 cm to 52 cm. The two innermost cylinders are 1.66 m long, and the other six are 2.52 m long. Such a design allows the large-diameter SMT H-disks to be inside the CFT

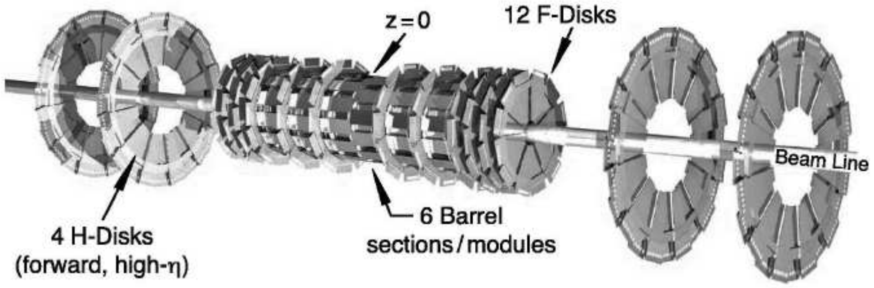

Figure 3.5: 3-D view of the silicon microstrip tracker.

cylinders. Each cylinder has two double-layers of scintillating fibers, an axial double-layer on the inside and a stereo double-layer on the outside, as shown in Figure 3.6. Fibers in the stereo double-layers make an angle of 3^o relative to the axial layers. Each double-layer is composed of 835 μm diameter scintillating fibers arranged in adjacent, parallel layers with the second layer overlapping the gaps of the first layer.

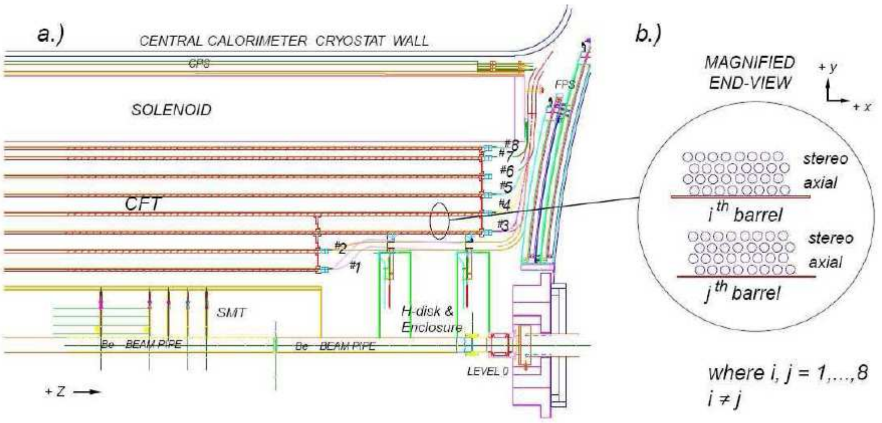

Figure 3.6: Diagrams illustrating the layers of scintillating fibers in the CFT.

The principle of operation of the fiber detector is based on the emission of photons by charged particles when they pass through the scintillating fiber. The peak emission wavelength of the fibers used in the CFT is approximately 540 nm. One of the end of the scintillating fibers is coated with aluminum so most of the light is collected by clear waveguides on the other end. Photons from the scintillating fibers are then carried by the waveguides to silicon avalanche photodetectors, or visible light photon counters (VLPC), which convert the photons into electric signals. The VLPCs are kept at 9 K for high efficiency and low noise. With the position of each fiber known to better than 50 μm, the spatial resolution of the CFT is on the order of 100 μm. The CFT covers the pseudorapidity range of up to $|\eta| < 1.7$.

The central tracking system is surrounded by a 2 T superconducting solenoid. The solenoid is enclosed in a cryostat which is 2.73 m long and 1.4 m in diameter, and is cooled by liquid helium to sustain the operating current of 4,749 A. The thickness of the solenoid is 0.87 radiation lengths (X_0) at $\eta = 0$. The solenoid is designed to provide a uniform magnetic field in the inner volume of the solenoid with the magnetic field lines parallel to the beam line. The magnetic field in the tracking system allows measurement of the charged particles' momentum, curvature of the track, and the charge to transverse momentum ratio.

Besides providing a measurement of momentum, the central tracking system is important for particle identification. Charged particles such as electrons and muons will leave isolated tracks. Neutral particles such as photons and neutrinos will leave no tracks. Particles produced with color charge such as quarks and gluons will produce a shower or “jet” of particles that result in a group of many tracks.

3.2.3 Preshower Detectors

The preshower detectors (PS) possess features of both the calorimeter and tracking detectors. By providing a position measurement, they can improve the quality of the match between tracks in the tracking detectors and clusters in the calorimeter. Photon identification also benefits from the PS, as the information about the position of the cluster in the PS is used in the pointing algorithm. This allows one to reconstruct the direction of flying of a photon candidate, which can be used to select the primary vertex for which the photon was produced, and to estimate how far the photon was produced from the beam line in the $r - \phi$ plane. Pointing information can also be used to estimate and suppress backgrounds. The energy deposited in the calorimeter, degraded mainly by the presence of the solenoid, can also be corrected using information from the preshower detectors. Their fast measurement of position and energy, and the distinctive shape of their clusters, allow the PS information to be included in the Level 1 trigger.

The preshower detectors are composed of the central (CPS) and two forward (FPS) sections, which use scintillator with 835 μm-diameter wavelength shifting fibers (WLS) with a triangular cross section arranged in layers, as shown in Figure 3.7.

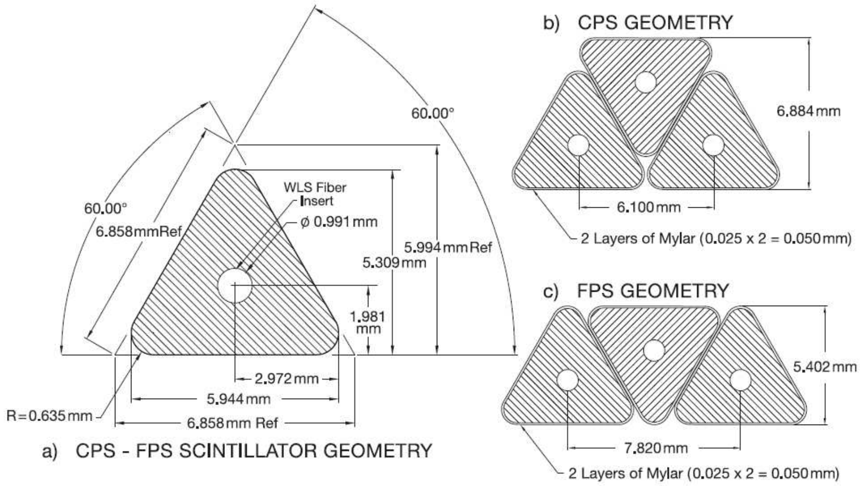

Figure 3.7: (a) Cross section diagram of a scintillating fiber used in the preshower detectors. (b) Diagram showing how fibers are stacked in each layer of the CPS. (c) Diagram showing how fibers are stacked in each layer of the FPS.

The CPS [37] is located between the solenoid magnet and the calorimeter, covering $|\eta| < 1.31$. A lead radiator, approximately 1 X_0 thick, sits in front of the CPS system. Particles pass through roughly two radiation lengths of material (one in the solenoid and inner detector and one in a thin lead layer on the outside of the solenoid) before striking the CPS. Electromagnetic particles will have started to shower and will deposit energy in several strips in each layer of the CPS. The CPS is built with three concentric cylindrical layers. When a charged particle crosses a layer, the ionization energy is collected in the form of light by the WLS and transported to the end of the detector. Light is then transmitted for readout to the same VLPC system used by the CFT through clear fibers. The triangular shape of the strips and the nested geometry typically allows a particle to pass through multiple strips, making strip-to-strip interpolations possible, which improves the precision of the position measurement.

The strips in the innermost (axial) layer are parallel to the beam pipe while the additional layers, u-stereo and v-stereo, are arranged at angles of 23.774° and 24.016°, respectively. Such a geometry allows reconstruction of 3-D clusters in the central preshower. Each layer is formed from eight octant modules with the WLS fibers split at $z = 0$ and read out from each end. There are, in total, 2560 readout channels per layer.

The two FPS [38] detectors are situated on the calorimeter endcaps with total coverage of $1.5 < |\eta| < 2.5$, but they are not used in this analysis.

3.2.4 Calorimeter

The DØ calorimeter is a liquid argon/uranium sampling calorimeter [31], which measures the incident particle energy and position, as well as helps in particle identification through the determination of the shower shape topology of different electromagnetic and strongly interacting particles. A 3-D view of calorimeter is shown in Figure 3.8. The calorimeter is divided into three separate pieces, a Central Calorimeter (CC) covering $|\eta| < 1.1$, and two endcap calorimeters (EC) with $1.3 < |\eta| < 4.0$. All three calorimeters are enclosed in separate cryostats and cooled to 90 K. Longitudinally the calorimeter is divided into the Electromagnetic (EM) section of high granularity, and two Hadronic (HAD) sections - fine and coarse.

DØ sampling calorimeter consists of alternating layers of absorber and active medium.Particles entering the calorimeter interact with the absorber and initiate showers of secondary particles. EM showers are produced by the particles such as

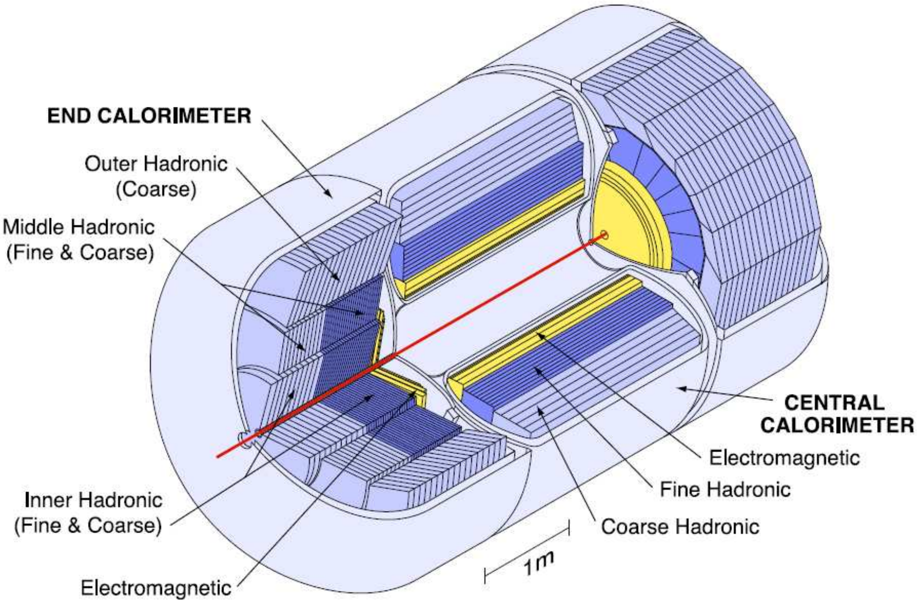

Figure 3.8: 3-D view of the DØ calorimeter.

electrons and photons that interact mostly via the electromagnetic force. The development of an EM shower is governed by the production of electron-positron pairs and bremsstrahlung. HAD showers are initiated by hadrons, either charged and neutral. The development of a HAD shower is governed by interactions between the particle and the nuclei via strong force. In addition, a typical HAD shower also contains an EM component from the EM interactions of charged hadrons. In both EM and HAD cases, the charged particles then ionize the liquid argon active medium. Electric charge from ionization is collected by the high voltage pads, and is proportional to the energy deposited in the active medium. Usually, EM showers are detected with higher response, than the HAD showers. This effect is known as *noncompensation*, and leads to a non-linear hadronic response as a function of energy. This can be prevented by either decreasing the EM calorimeter sensitivity, or increasing the HAD calorimeter sensitivity. At DØ, compensation is achieved by using uranium absorbers in the EM and fine HAD sections of the calorimeter.

The calorimeter cells are arranged in four EM layers, three fine hadronic (FH) layers (four in the EC), and one coarse hadronic (CH) layer. These layers form pseudo-projective towers, as seen in Figure 3.9. The inner four layers of the CC and ECs are the EM layers. The next three layers in the CC are the FH layers and the outer most layer is the CH layer. The hadronic layers in the ECs are separated into inner fine hadronic (IFH), inner coarse hadronic (ICH), middle fine hadronic (MFH), middle coarse hadronic (MCH), and outer hadronic (OH).

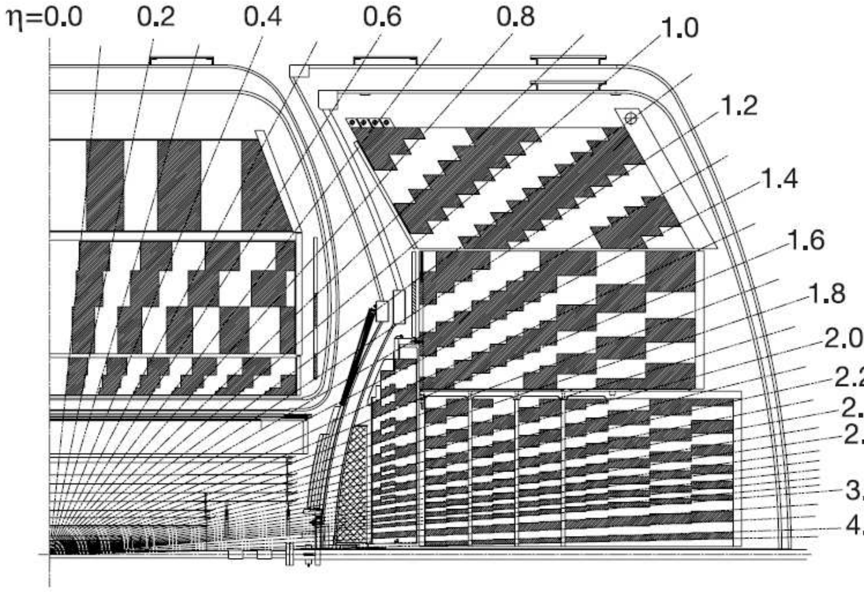

Figure 3.9: Diagram showing calorimeter towers in η.

Each layer is segmented transversely into cells of approximately 0.1×0.1 in $\eta \times \phi$. The two exceptions are the third EM layer, which has 0.05×0.05 segmentation, and the ECs with $|\eta| > 3.2$, which has reduced granularity due to space constraints. The maximum of EM showers is located in the third layer of the EM calorimeter, hence this layer has a finer granularity, $\Delta\eta \times \Delta\phi = 0.05 \times 0.05$, compared to 0.1×0.1 in the other three layers. A summary of the properties of the various calorimeter CC layers is given in Tables 3.1.

In total, the calorimeter has around 50,000 readout cells. With so many cells there is a significant chance for a false signal from electronics noise and/or uranium

Table 3.1: Properties of CC layers

	EM	FH	CH
Number of readout layers	4	3	1
Signal boards per readout layer	2,2,7,10	20,16,14	9
Absorber material	Uranium	Uranium-Niobium	Copper
Radiation lengths (X_0)	20.5	96.0	32.9
Nuclear interaction lengths (λ_A)	0.76	3.2	3.2

decay in the calorimeter. Therefore, before object reconstruction the so called “T42” zero-suppression algorithm [39] is used to reduce the effects of noise by removing cells that do not measure an energy significantly higher than the noise level. Specifically, cells are removed unless they have an energy at least four standard deviations above the noise ($E_{cell} \geq 4\sigma_{noise}$), or have $E_{cell} \geq 2.5\sigma_{noise}$ and are adjacent to a cell with $E_{cell} \geq 4\sigma_{noise}$.

In order to accommodate the beam crossing occurring every 396 ns, and taking into account the electron drift time across the liquid-argon gap of approximately 450 ns, a base line subtraction (BLS) system is implemented to handle the effects of pile-up. The readout chain shown in Figure 3.10 starts with the charge being collected at the cell pads. The charge is then transported to the readout electronics via coaxial cables and integrated in a preamplifier system. The output signal is shaped and filtered in the BLS circuitry. The BLS uses switched capacitor arrays (SCA) to store the signal until Level 1 and Level 2 trigger decisions are made. The SCAs store two gain paths separately (gain x1 and gain x8) in order to extend the analog to digital converters (ADC) readout dynamic range. Upon a positive trigger decision, the precision analog signals from the BLS are transmitted to the ADCs for digitization. These signals are then subject to a Level 3 decision and are recorded to tape alongside the rest of the event information if the event is accepted.

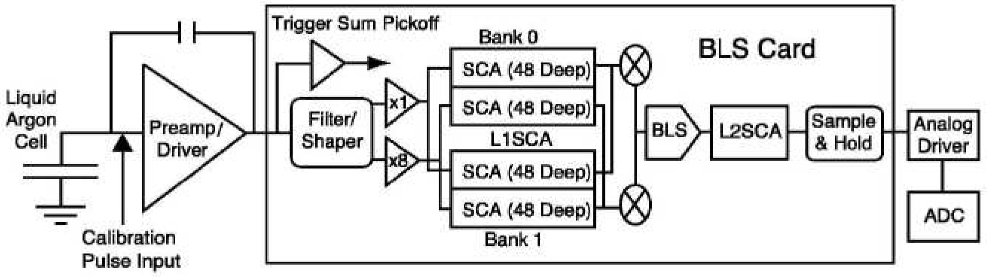

Figure 3.10: Readout chain of the calorimeter.

To equalize the energy response at the cell level, inter-calibration factors are derived using special runs with a calibration pulser system and with physics data [40]. The pulser calibration determines two parameters, a nonlinearity parameter and a gain factor. The observed nonlinearity in the calorimeter response originates from saturation effects in the SCA. The gain-factors account mostly for variations in the preamplifier response.

3.2.5 Intercryostat Detector

Separate cryostats for all three calorimeters result in an incomplete coverage in the $0.8 < |\eta| < 1.4$ region. Also, due to the presence of a significant amount of dead material, the energy resolution in this pseudorapidity range is poor. To account for that, additional sampling layers are installed there, forming the so-called *intercryostat detector* (ICD). The ICD is divided into eight $\Delta\eta \times \Delta\phi = 0.3 \times 0.4$ octants (tiles), each consisting of twelve 0.1×0.1 trapezoidal subtiles. However, this detector is not used in this analysis.

3.2.6 Muon Spectrometer

The muon system is the outermost section of the DØ detector, and is designed to detect muons. With energies between a few hundred MeV and a few hundred GeV, muons are minimum ionizing particles, losing energy at a rate of around 0.25 GeV per nuclear interaction length traversed. Since muons do not get absorbed in the calorimeter, by putting muon spectrometer outside, they can be identified. The muon spectrometer allows for local, tracker-independent momentum measurement of muons. In this analysis, the muon spectrometer is not used.

3.2.7 Luminosity Monitor

The luminosity monitor (LM) is used to determine the instantaneous luminosity being delivered to the DØ detector by measuring the rate of proton-antiproton collisions. The luminosity counters are made of two sets of 24 plastic scintillators, which are located in front of the end-cap calorimeters at $|z| = 140$ cm. and cover a range of $2.7 < |\eta| < 4.4$, as shown in Figure 3.11.

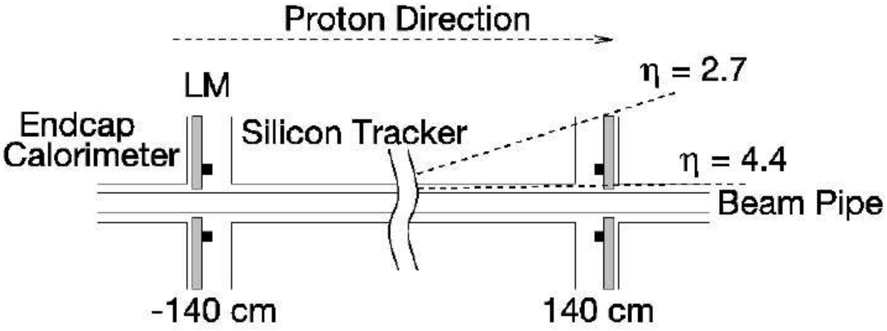

Figure 3.11: Side view of the luminosity monitor.

The average number of inelastic collisions per beam crossing N_{LM} is used to determine the luminosity

$$\mathcal{L} = f \cdot \frac{N_{LM}}{\sigma_{LM}}, \tag{3.6}$$

where f is the beam crossing frequency and σ_{LM} is the effective cross section for the luminosity monitor which takes into account the acceptance and efficiency of the LM. To suppress the beam halo backgrounds that result in an overestimated N_{LM}, the time-of-flight is measured for particles that hit the South and North LM scintillator arrays, t_- and t_+. The z position of the interaction point, z_v can then be estimated as

$$z_v = c \cdot \frac{t_- - t_+}{2} \tag{3.7}$$

Requiring $|z_v| < 100$ cm makes beam halo background negligible.

3.2.8 Trigger and Data Acquisition System

With 36 bunches of protons and antiprotons traveling around the Tevatron every 21 μs, the average rate of bunch crossings at the center of the DØ detector is 1.7 MHz. A three-level trigger system is implemented to reduce the rate to about 100 Hz of interesting physics events. The DØ trigger system starts with the Level 1 (L1), which is based on custom-made hardware and firmware and reduces the rate to about 2 kHz. The second stage, called Level 2 (L2), uses hardware engines and single board computers (SBC) running simple software algorithms to reduce the rate to 1 kHz. The Level 3 (L3) trigger uses more sophisticated algorithms that run in a farm of computers and reduces the rate to about 100 Hz.

Different trigger definitions are formed by applying certain requirements at the three distinct levels of the trigger architecture. Every event written to tape for later offline reconstruction has to satisfy at least one of these trigger definitions, which are basically a specific *AND* condition on L1, L2 and L3 requirements. A collection of trigger definitions forms a trigger list. These lists are defined for different ranges of instantaneous luminosities in order to optimize the acceptance rate of interesting physics processes at the different trigger levels. The trigger system is tightly integrated with the DØ data acquisition system, as shown in Figure 3.12.

The DØ data acquisition system (L3DAQ) transports data from the subdetectors

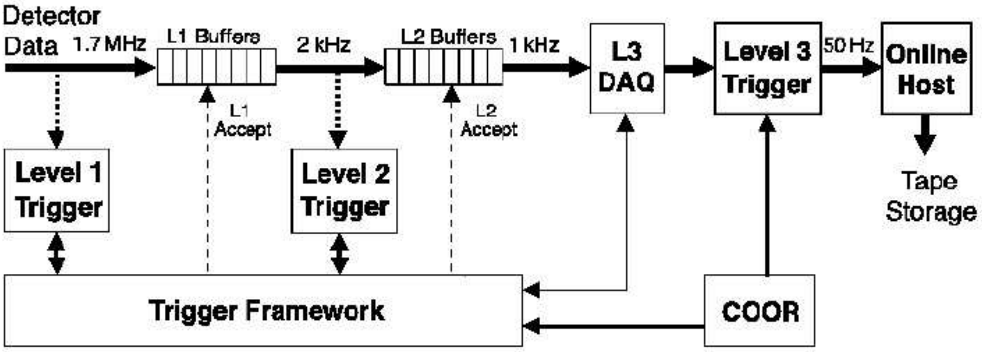

Figure 3.12: Overview of the DØ trigger and data acquisition systems.

to the L3 farm nodes, and controls the flow of information from the L3 trigger to the data logger and tape storage. A COOR program (running on the online host) handles the data acquisition, as well as triggering and overall coordination.

All nodes in the L3DAQ system (as well as the VME readout crates) are based on the SBC computers. The event builder (EVB) process, running on each farm code, builds a complete event from event fragments and organizes them into a readable format for the L3 trigger software. Both processes are controlled by the COOR program, which also informs the L1, L2 and L3 filters of the availability of the next event. The COOR sends events that pass the L3 trigger to the buffer. Events from the buffer are transmitted to the storage facility and are written to tape.

Chapter 4

Data Reconstruction

Detector data from triggered events are stored on tape and processed with the DØ Offline Reconstruction Software Package (DØRECO) [41] to build physical objects that are later used to perform DØ physics analyses. The reconstruction program is run on the offline production farms and it is based on the DØ Event Data Model [42]. A overview of the algorithms for different physical objects (tracks, vertices, electrons, photons, hadronic jets, etc.) is presented in the following subsections.

4.1 Track Reconstruction

Charged particles traversing the tracker interact with the SMT silicon strips or the CFT fibers in each layer, resulting in clusters of hits. Two algorithms, the Alternative Algorithm [43] and the Histogramming Track Finder [44], are used to reconstruct tracks. The track reconstruction efficiency measured in $Z \to e^+e^-$ data is $93.0\pm0.1\%$.

The Alternative Algorithm (AA) constructs a large pool of track hypotheses by extending seed clusters of tracking hits from the SMT to the rest of the tracking system. It filters down the number of track candidates based on well defined criteria and eliminates all overlapping hypotheses until no more tracks remain in the pool.

The Histogramming Track Finder (HTF) finds tracks by filling a histogram in the track parameter space (track curvature and azimuthal angle) with values consistent with each hit in the CFT and the SMT. Hits from the same particle will produce a peak in the histogram whereas random hits will uniformly populate the space.

The Alternative Algorithm In this method, an initial track hypothesis is reconstructed from three two-dimensional measurements (hits) in the SMT barrels or F-disks. The selection of hits starts at the inner-most layer and goes to the outermost layer of the tracking system. The next hit is selected in any successive layer if the axial angle between the first and the second hit $\Delta\phi$, as seen from the beamspot, is less than 0.08. The third hit is selected in successive layers of the SMT, provided that the radius of curvature of the constructed track hypothesis is greater than 30 cm (corresponding to track $p_T > 180$ MeV) and its axial impact parameter with respect to the beam spot is less than 2.5 cm. Additionally, the hits must fit the track with χ^2 fit value less than 16.

The initial track hypothesis is then extrapolated to the hits in the outer layers of the SMT and CFT. These hits are selected within an expectation window of the track hypothesis and are associated to the track if the resulting χ^2 increases by less than 16 for each new hit. If more than one hit is accepted, each of the hits is added separately, thus making multiple track hypotheses.

The algorithm skips the layer if there are no hits in this layer within the window. Missing hits (misses) are monitored, taking into account adjustments for the presence of dead or disabled channels. Misses can be characterized as inside misses, which are those in between any two hits of a track hypothesis, and forward and backward misses, which are basically missed hits in the corresponding track extrapolation path. The track hypotheses are then sorted using the following requirements:

* There must be at least four hits in the central tracker (SMT or CFT), in both axial and stereo layers. (*i.e.* the track hypothesis is discarded if a track is only two-dimensional.)

* No more than three inside misses, no more than six total forward and backward misses, and no more than two misses in the SMT are allowed. In addition, a maximum of four inside misses and a forward miss, or three inside misses and a backward miss is allowed.

* $N_{hits}/5 \geq N_{miss}$.

If the above requirements are fulfilled, the track is added to the pool. Within this pool, tracks are ordered by the total number of hits, the number of misses and the χ^2 of the fit. A hypothesis is declared an AA-track if $N_{shared} \leq 2N_{total}/3$ and $N_{shared} \leq N_{total}/5$ OR $N_{total} - N_{shared} \geq 3$, where N_{shared} (N_{total}) is the shared (total) number of axial hits.

In order to locate tracks with few or no hits in the SMT, AA is run a second time to search for hits in the CFT, using the preliminary vertex estimated in the first run. This allows for a smaller combinatorial background due to a larger number of hits in the CFT.

The Histogramming Track Finder The trajectory of a charged particle moving in a constant magnetic field can be characterized with three parameters in the plane perpendicular to the field lines: the radius of curvature, $\rho = qB/p_T$; the impact parameter, d_0; and the azimuthal angle, ϕ. Here q and p_T are the charge and transverse momentum of the particle, and B is the magnetic field. The HTF method relies on the so-called Hough transformation, which simply realizes that a family of possible trajectories crossing the (x, y) coordinates of a hit (in the SMT or CFT) of an unknown trajectory can be mapped into a single line in the parameter space (ρ, ϕ). The parameters of the unknown trajectory will be associated to the intersection of such lines after all possible hits are taken into consideration. By quantizing the parameter space one gets a histogram with a clearly pronounced peak. A Kalman filter is then employed to remove noisy or fake tracks.

4.2 Vertex Reconstruction

The position of the proton-antiproton collision, referred to as the primary vertex (PV), is an important quantity since it is used in the calculation of transverse energy and E_{Tmiss}. A three-step algorithm is used to reconstruct the PV: track selection, vertex fitting, and vertex selection.

In the first step, tracks with $p_T > 0.5$ GeV/c and having at least two hits in the SMT detector are selected. They are then clustered together to identify different interactions if they are less than 2 cm apart from each other along the z axis.

In the second step, for each of the track z-clusters, all the tracks within one cluster are fitted into a common vertex using an Adaptive Primary Vertex Algorithm [45], and a χ^2 for each track is calculated. The track errors are reweighted taking into account the χ^2 contribution of this track to the vertex. The weight is re-computed always with respect to the new fitted vertex at each iteration until convergence is achieved.

In the third step, the reconstructed primary vertices are ordered according to their increasing probability of coming from a Minimum Bias (MB) interaction [46]. Tracks from a MB interaction tend to have much lower p_T than tracks from a hard interaction. Using the track p_T, the probability for each track to have originated from a MB interaction is calculated. The MB probabilities for all tracks coming from a given vertex are multiplied to determine the MB probability for that collision vertex. The PV with the lowest MB probability is picked as the default hard scatter interaction vertex. More details of the PV selection in this analysis will be presented in Section 5.4.

4.3 Electromagnetic Object Reconstruction

Electromagnetic objects, electrons and photons, deposit most of their energy in the EM part of the calorimeter through the initiation of EM showers due to e^+e^- pair production of photons or bremsstrahlung of electrons. The EM shower develops in the transverse and longitudinal directions. The longitudinal development of the shower scales as the X_0, with the maximum of the shower around 6 X_0. Roughly 98% of the total energy of the shower is contained in 20-22 X_0. The transverse development scales as the Molière radius, R_M. The width of the shower is estimated as 3.5 R_M. Showers initiated by electrons and photons share the same basic properties. However, due to the fact that the mean distance traveled by a photon before producing e^+e^- pair is $9X_0/7$, showers initiated by photons typically start somewhat deeper in material compared to showers by electrons.

A Simple Cone Algorithm [47] is used to construct calorimeter clusters, which starts with EM towers. An EM tower is defined as the first five layers of a 0.1×0.1 ($\eta \times \phi$) tower of calorimeter cells (the four EM layers plus the first hadronic layer). EM towers with minimum transverse energy of 0.5 GeV are declared as seeds. A cone of $\Delta R < 0.4$ in $\eta \times \phi$ plane is drawn around each seed. The algorithm loops over all the towers within the cone. Each time another tower is found and added to the cluster, the energy-weighted position of the cluster is calculated, and a cone of radius of 0.4 is drawn around this new position. The algorithm repeats until a stable cluster is found. Any seed towers inside the cluster are removed from the list of seeds and the procedure is repeated with the updated list of seeds to find the next cluster. The cluster constructed is accepted if the total transverse energy E_T is greater than 1.5 GeV and at least 90% of its energy is deposited in the EM section of the calorimeter; otherwise, it is rejected.

At the next stage of this algorithm, the calorimeter isolation variable is calculated for each cluster. The tower with the highest energy in the cluster is selected. The algorithm makes a list of towers within a large window of radius four calorimeter towers centered at this tower. A circle of radius $\Delta R = 0.4$ is drawn around the initial cluster position. From the list of towers, the total energy E_{total} (EM + HAD) within this cone is calculated. Using the same list of towers, the EM energy around

$\Delta R < 0.2$ from the initial cluster position, E_{core} is calculated. If the calorimeter isolation variable, defined as $(E_{total} - E_{core})/E_{core}$, is smaller than 0.2, the cluster is considered as isolated and is stored, otherwise it is rejected. A graphical visualization of this isolation variable is shown in Figure 4.1.

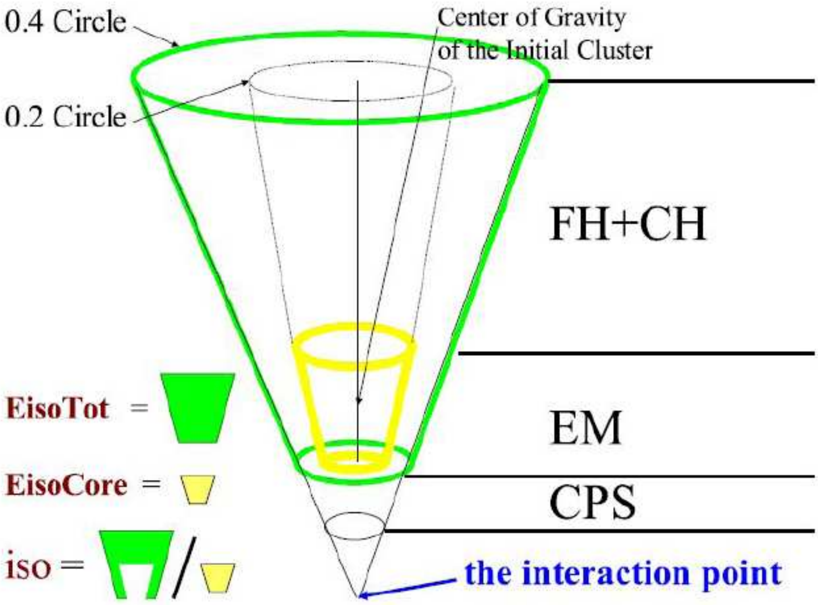

Figure 4.1: Schematic view of the calorimeter isolation.

To improve the identification of EM objects and suppress the backgrounds, a list of quality variables are constructed. The variables used in this dissertation are described below.

The basic quality variables are EM-fraction and isolation defined as

$$emfrac = \frac{E_{EM}(0.2)}{E_{total}(0.2)} \tag{4.1}$$

and

$$iso = \frac{E_{total}(0.4) - E_{EM}(0.2)}{E_{EM}(0.2)}, \tag{4.2}$$

respectively. Here $E_{total}(R)$ is the total energy (all EM and hadronic layers) inside a cone of radius R and $E_{EM}(R)$ is the energy in only the EM layers inside a cone of radius R. EM-fraction and isolation are remarkably good at rejecting clusters that are not EM showers. In the preselection, cuts of $emfrac > 0.9$ and $iso < 0.2$ are applied. Figure 4.2 shows plots of iso and $emfrac$ for CC electrons, photons and jet-faked EM objects.

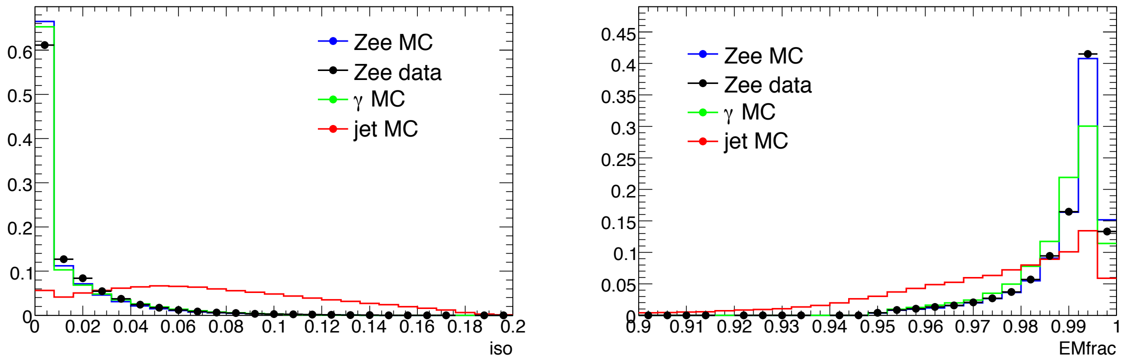

(a) iso (b) $emfrac$

Figure 4.2: Normalized distributions of iso and $emfrac$ variables for CC photons (green line), jet-faked EM objects (red line) from Monte Carlo (MC) simulation, electrons from MC (blue line) and data (black dots).

The track isolation variable, $IsoHC4$ allows one to significantly suppress the backgrounds from misidentified jets, as they are likely to have a rather high tracker activity. $IsoHC4$ is defined as the sum of p_T of all reconstructed tracks around an EM candidate in an annulus with openings $0.05 < \Delta R < 0.4$, if these tracks are within 2 cm from the primary vertex or the pointed vertex of the photon in the z direction. The typical requirement of the track isolation for electrons or photons is a value less than 2-2.5 GeV/c, as shown in Figure 4.3 a.

The width of the EM cluster in the third layer of the EM calorimeter in $r-\phi$, $sigphi$ is used in the analysis as a part of the photon identification criteria. In the central calorimeter $sigphi$ is used with an upper threshold of 14 cm^2, shown in Figure 4.3 b.

The HMatrix variable, $HMx7$ is constructed out of seven variables: the energy fractions in all four layers of the EM section of the calorimeter, the total energy of the shower, the position of the primary vertex, and the shower width in $r-\phi$ at the third EM layer. The covariance matrix is constructed as

$$M_{ij} = \frac{1}{N}\sum_{n=1}^{N}(x_i^n - < x_i >)(x_j^n - < x_j >), \tag{4.3}$$

where the summation is performed over MC electrons, and x_i ($< x_i >$) is the value (expectation value) of variable i. The H-matrix is defined simply as the inverse of the covariance matrix, $\mathrm{H} \equiv \mathrm{M}^{-1}$. Then, the $HMx7$ variable is defined as

$$HMx7 = \sum_{i,j=1}^{7}(x_i - < x_i >)H_{ij}(x_j - < x_j >); \tag{4.4}$$

where x_i is the value of variable i for the electron candidate being evaluated. Typically $HMx7$ for real EM showers are smaller than those for showers from jets, shown in Figure 4.3 c.

Electron neural net variable $NN7$ is constructed from seven variables and used for electron identification in the central region, shown in Figure 4.3 d. The $NN7$ variables are the fraction of EM cluster energy deposited in the first EM layer (EM1) ($EM1frac$), the number of EM1 cells in cone 0.2 ($EM1cells$), $IsoHC4$, the number of EM1 cells in an annulus cone $0.2 < \Delta R < 0.4$ ($EM1conecells$), the number of tracks in a cone 0.05 ($Ntrks005$), the number of CPS clusters in a cone 0.1 ($Ncps$) and the energy squared weighted RMS of CPS (E_{E2RMS}) which is

$$E_{E2RMS} = \frac{\sum_i E_i^2 \times (\phi_c - \phi_i)^2}{\sum_i E_i^2}, \tag{4.5}$$

where E_i is the energy of the i^{th} strip, ϕ_i is the ϕ of the i^{th} strip, ϕ_c is the ϕ of the electromagnetic cluster in the third layer of the EM calorimeter, and the summation is carried out over the strips in the window about the cluster.

For photons in the central region, a neural net variable $NN5$ is constructed based on five variables, shown in Figure 4.3 e. Compared to $NN7$, $NN5$ does not use $EM1frac$ and $Ntrks005$.

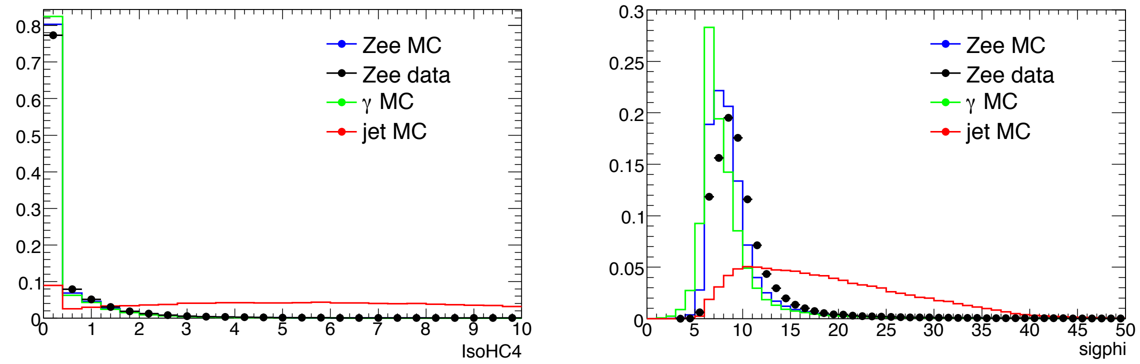

(a) $IsoHC4$

(b) $sigphi$

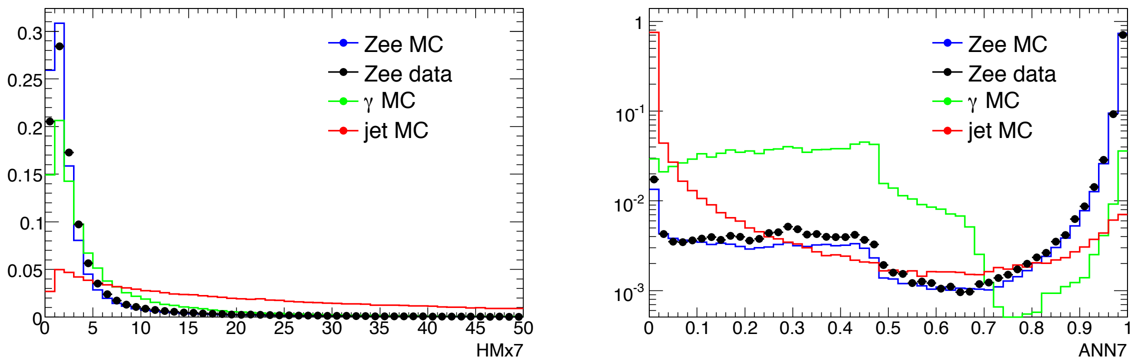

(c) $HMx7$

(d) $NN7$

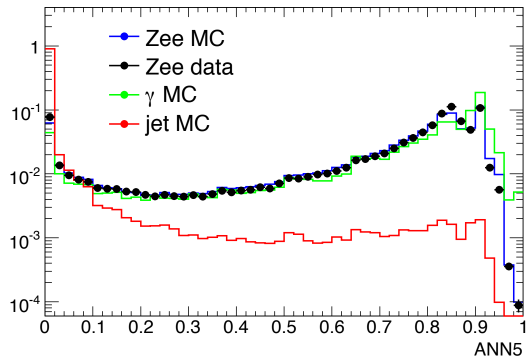

(e) $NN5$

Figure 4.3: Normalized distributions of $IsoHC4$, $sigphi$, $HMx7$, $NN7$, $NN5$ variables for CC photons (green line), jet-faked EM objects (red line) from Monte Carlo (MC) simulation, electrons from MC (blue line) and data (black dots).

To determine how well the cluster is matched to a track, a spatial track match χ^2 is calculated:

$$\chi^2_{spatial} = (\frac{\Delta\phi}{\sigma(\phi)})^2 + (\frac{\Delta\eta}{\sigma(\eta)})^2, \tag{4.6}$$

where $\Delta\phi$ and $\Delta\eta$ are the separations between the position of an EM cluster in the third layer of the EM calorimeter and the central track, and $\sigma(\phi)$ and $\sigma(\eta)$ are the resolutions of these quantities. The typical requirement of the spatial track match χ^2 probability for electrons is a value exceeding 0.001-0.1.

Since not all tracks are reconstructed, the Hits-on-the-road variable (HOR or $emhits\_e\_f\_discriminant$) was developed to improve the tracking efficiency. The HOR is defined as the probability of an EM object to have a track based on the density of hits in the central tracker, and is used as a powerful tool to discriminate between real electrons and fakes which tend to have HOR close to zero. Most of the time, this variable is "OR′ed" with the spatial track match χ^2 probability, e.g. ($\chi^2_{spatial} > 0.001 || HOR > 0.4$). This combination is inverted for photons.

Matching a calorimeter cluster with preshower clusters is used to help select the primary vertex position for photon events. The matching algorithm looks for a CPS cluster in the $\Delta\eta \times \Delta\phi = 0.1 \times 0.1$ window around the EM cluster in the calorimeter, and matches the calorimeter cluster to the most energetic CPS cluster.

4.4 Jet Reconstruction

Quarks and gluons (parton level) produced in hadron-hadron collisions fragment into mesons and baryons (hadronization). These energetic sprays of particles are known as jets. At DØ, jets are identified using a cone algorithm. Since jets are not used in this analysis, no more details are presented here.

4.5 Muon Reconstruction

Muon candidates are reconstructed using hits in the wire chambers and scintillation counters of the local muon system, as well as hits in the central tracking system. Since muons are not used in this analysis, no more details are presented here.

4.6 Missing Transverse Energy

At DØ, proton-antiproton collisions occur at a very small angle to the beam line, so the total transverse momentum at the interaction point is approximately zero, However, due to the finite resolution of the detector and non-interacting particles like neutrinos carrying away a significant amount of energy without being reconstructed, the vector sum of transverse momentum in an event can be large. The imbalance of the transversed energy is measured as missing transverse energy, $\not\!\!E_T$. Since $\not\!\!E_T$ is not used in this analysis, no more details are presented here.

Chapter 5

Data Samples and Event Selection

5.1 Dataset

The data used in this analysis were collected with the DØ detector between July 2002 and June 2009, with run numbers from 160582 to 252918. This data sample is separated into two periods: the first one is from July 2002 to February 2006 (Run IIa sample, p17, run numbers 160582-215670). The second period is from June 2006 to June 2009 (Run IIb sample, p20, run numbers 222028-252918).

The analysis begins with the 2EMhighpt (two EM clusters with $p_T > 12$ GeV) skims produced by the Common Sample Group [48]. Table 5.1 shows the dataset definitions of the samples used. Version v2009-06-13 of the Data Quality Definitions package dq_defs [49] is used, but modified such that events with problems only in the muon system are kept, since muons are not used in the analysis. Events with bad luminosity blocks or run number are removed. The total integrated luminosity of the sample is 5.4 ± 0.3 fb^{-1}, as listed in Table 5.2.

We use events collected with all the calorimeter-only triggers selecting two clusters of energy in the EM calorimeter (diEM) (see Tables 5.3, 5.4). The trigger efficiency of preselected events for v8-v14 has previously been estimated to be 100% with a precision of 0.1% [50]. For v15 and v16, the trigger efficiency is estimated to be

Table 5.1: Dataset definitions used in this analysis.

dataset	number of events
CSG_CAF_2EMhighpt_PASS3_p18.14.00	36.3M
CSG_CAF_2EMhighpt_PASS2_p21.10.00	29.2M
CSG_CAF_2EMhighpt_PASS4_p21.10.00_p20.12.00	9.4M
CSG_CAF_2EMhighpt_PASS4_p21.10.00_p20.12.01	0.9M
CSG_CAF_2EMhighpt_PASS4_p21.10.00_p20.12.02	19.6M
CSG_CAF_2EMhighpt_PASS4_p21.10.00_p20.12.04	0.3M
CSG_CAF_2EMhighpt_PASS4_p21.12.00_p20.12.05_allfix	33.7M

Table 5.2: Integrated luminosity for different trigger versions.

version	integrated luminosity (pb^{-1})
v8-v11	140.20
v12	240.08
v13	384.54
v14	341.28
v15	1644.51
v16	2646.84
total	5398.45

greater than 98% for a diEM invariant mass $M_{e^+e^-} = 60$ GeV, increasing to about 100% at $M_{e^+e^-} = 90$ GeV [51]. The mass dependence is shown in Figure 5.1, and can be parameterized as

$$\epsilon^{v15,16}_{trigger}(M_{e^+e^-}) = 0.5 \cdot p_2 \cdot (1.0 + \text{TMATH} :: \text{Erf}((M_{e^+e^-} - p_0)/(\sqrt{2} \cdot p_1))) \times (1.0 \pm 0.001) \tag{5.1}$$

where $p_0 = -16.39$, $p_1 = 34.55$, $p_2 = 0.9995$.

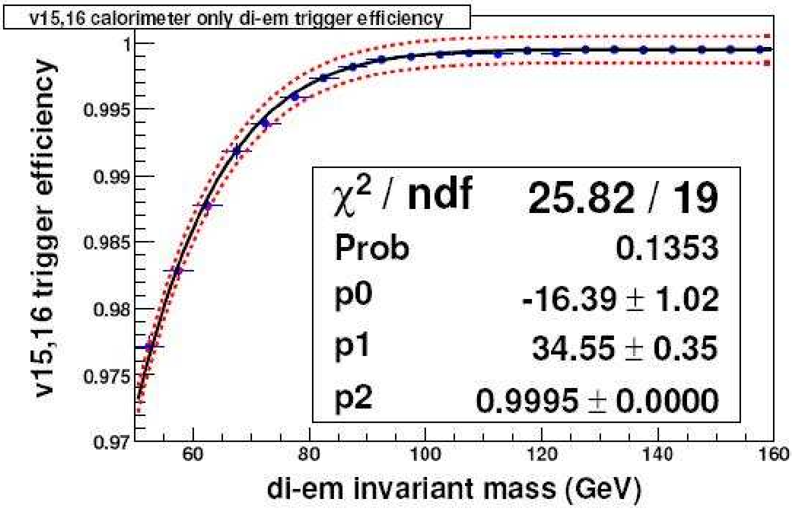

Figure 5.1: Trigger efficiency for v15 and v16 calorimeter-only diEM triggers as a function of diEM invariant mass. The two dotted lines illustrate the assigned 0.1% uncertainty.

5.2 Simulated Samples

The Monte Carlo (MC) samples used in this analysis are listed in Table 5.5 for the RS graviton signal and in Tables 5.7 and 5.8 for the various backgrounds.

Monte Carlo samples were generated for RS graviton decays to dielectron and diphoton final states. A total of 19 different graviton mass values, ranging from 220 GeV to 1050 GeV, were simulated. Values of the dimensionless coupling $k/\overline{M}_{\text{Pl}}$

Table 5.3: Calorimeter-only diEM triggers for RunIIa used in this analysis.

version	trigger name
v8-v11	2EM_HI, 2EM_HI_SH, 2EM_HI_EMFR8
v12	E1_2SH8, E1_2L15_SH15, E1_2L20, E2_2SH8, E2_2L15_SH15, E2_2L20, E3_2SH8, E3_2L15_SH15, E3_2L20.
v13	E1_2L20, E2_2L20, E3_2L20, E4_2L20, E20_2L20, E21_2L20, E22_2L20, E23_2L20, E25_2L20, E1_2L15_SH15, E2_2L15_SH15, , E3_2L15_SH15, E4_2L15_SH15, E20_2L15_SH15, E21_2L15_SH15, E22_2L15_SH15, E23_2L15_SH15, E25_2L15_SH15, E1_2SH8, E2_2SH8, E3_2SH8, E4_2SH8, E20_2SH8, E21_2SH8, E22_2SH8, E23_2SH8, E25_2SH8.
v13.20	E1_2L20, E2_2L20, E3_2L20, E4_2L20, E20_2L20, E21_2L20, E22_2L20, E23_2L20, E25_2L20, E1_2L15_SH15, E2_2L15_SH15, , E3_2L15_SH15, E4_2L15_SH15, E20_2L15_SH15, E21_2L15_SH15, E22_2L15_SH15, E23_2L15_SH15, E25_2L15_SH15, E1_2SH10, E2_2SH10, E3_2SH10, E4_2SH10, E20_2SH10, E21_2SH10, E22_2SH10, E23_2SH10, E25_2SH10.
v14	E1_2L20_L25, E2_2L20_L25, E3_2L20_L25, E4_2L20_L25, E5_2L20_L25, E6_2L20_L25, E1_2L15_SH15_L20, E2_2L15_SH15_L20, E3_2L15_SH15_L20, E4_2L15_SH15_L20, E5_2L15_SH15_L20, E6_2L15_SH15_L20, E1_2SH10_SH15, E2_2SH10_SH15, E3_2SH10_SH15, E4_2SH10_SH15, E5_2SH10_SH15, E6_2SH10_SH15.

Table 5.4: Calorimeter-only diEM triggers used for RunIIb in this analysis.

version	trigger name
v15	E1_2L15SH15_L20, E1_2L20_L25, E1_2SH10_SH15, E2_2L15SH15_L20, E2_2L20_L25, E2_2SH10_SH15, DE1_2L15SH15_L20, DE1_2L20_L25, DE1_2SH10_SH15, DE2_2L15SH15_L20, DE2_2L20_L25, DE2_2SH10_SH15, DE3_2L15SH15_L20, DE3_2L20_L25, DE3_2SH10_SH15.
v16	E1_2L15SH15_L20, E1_2L20_L25, E1_2SH10_SH15, E2_2L15SH15_L20, E2_2L20_L25, E2_2SH10_SH15, DE1_2L15SH15_L20, DE1_2L20_L25, DE1_2SH10_SH15, DE3_2L15SH15_L20, DE3_2L20_L25, DE3_2SH10_SH15.

Table 5.5: DØ official MC signal samples used in the analysis. All samples were generated using PYTHIA v6.409. The p17 signal samples are produced with d0release p17.09.08 and the p20 signal samples are produced in d0release p20.09.03.

signal sample	p17 ReqId	p20 ReqId
$G^* \rightarrow e^+e^-$	106772-106805	102052-102085,105961-105981
$G^* \rightarrow \gamma\gamma$	106806-106839	102096-102139,105982-106002

in the range spanning from 0.01 to 0.1 were used. The leading order (LO) cross section multiplied by the branching ratio to e^+e^- from PYTHIA is listed in Table 5.6 for the various MC signal samples. For each signal sample, around 20K events were generated.

The background samples used in this analysis include DY e^+e^-, direct $\gamma\gamma$ production, DY $\tau^+\tau^-$, $W\gamma$, WW, ZZ, WZ, $W+X$, $t\bar{t}$. The cross sections quoted in Table 5.7 are PYTHIA values.

The complexity of nature makes MC simulations of physics processes and detector response unable to reproduce perfectly what is seen in data. In order to model the data more accurately, additional studies are performed to determine the differences between simulation and data, and then MC simulations are corrected to match the performance observed in the data.

In order to simulate the effect of the trigger selection in the MC samples, a trigger weight is applied to each MC event. The trigger weight for a given MC event represents the probability that the same event in the data would have passed the trigger requirements. The weight is parameterized as a function of diEM invariant mass as described earlier in this chapter.

The MC samples are overlaid with zero bias events with the intent of making the simulated events more like the detector data. However, the zero bias events were not collected with the same luminosity spectrum as the data, which could result in small differences between the data and MC. Therefore, each of the MC samples has been reweighted based on the instantaneous luminosity of the overlaid zero bias events in order to have the same luminosity profile as the data.

Also, the z position of the primary vertex in MC events is Gaussian distributed, while in data the distribution is slightly non-Gaussian. Thus, the MC samples are reweighted to make the z position of the primary vertex match the actual vertex distribution measured in the data.

MC simulation produces EM objects with slightly better energy resolution than

Table 5.6: List of graviton MC samples simulated with the corresponding LO cross sections.

Graviton Mass (GeV)	Coupling $k/\overline{M}_{\mathrm{Pl}}$	Cross Section × BR ($G^* \to e^+e^-$) (fb)
220	0.01	58.8
250	0.01	31.9
270	0.01	22.2
300	0.01	13.7
350	0.01	6.75
400	0.01	3.55
450	0.01	1.99
500	0.02	4.52
550	0.02	2.66
600	0.02	1.59
650	0.02	0.95
700	0.02	0.57
750	0.03	0.78
800	0.03	0.46
850	0.05	0.74
900	0.05	0.43
950	0.07	0.47
1000	0.10	0.55
1050	0.10	0.30

Table 5.7: DØ official p17 MC background samples used in the analysis. All samples were generated using PYTHIA. For d0release p17.09.06, PYTHIA v6.323 is used. For d0release p17.09.08, PYTHIA v6.409 is used. For DY e^+e^-, direct $\gamma\gamma$ and DY $\tau^+\tau^-$ samples, the events were generated in several mass bins.

sample	ReqId	d0release	Events	cross section (pb)
$Z/\gamma^* \rightarrow e^+e^-$				
$15 - 60$ GeV	40668-40677	p17.09.06	1.99M	361.5
$60 - 130$ GeV	38770-38784,42033-42039	p17.09.06	3.93M	178.0
$130 - 250$ GeV	35707,35708,41249,41250	p17.09.06	0.49M	1.3
$250 - 500$ GeV	35713,41255	p17.09.06	0.15M	0.11
500 GeV$-$	35716,41260	p17.09.06	0.08M	0.0045
SM $\gamma\gamma$				
$50 - 130$ GeV	110272,110273	p17.09.08	0.39M	42.7
$130 - 250$ GeV	110274,110275	p17.09.08	0.39M	3.1
$250 - 500$ GeV	110276,110277	p17.09.08	0.40M	0.49
500 GeV$-$	110278,110279	p17.09.08	0.38M	0.03
$Z/\gamma^* \rightarrow \tau^+\tau^-$				
$60 - 130$ GeV	39216-39230	p17.09.06	3.06M	178.0
$130 - 250$ GeV	35711,35712,41253,41254	p17.09.06	0.50M	1.3
$250 - 500$ GeV	35715,41257	p17.09.06	0.15M	0.11
500 GeV$-$	35718,41258	p17.09.06	0.08M	0.0045
$W\gamma$	90538,90539	p17.09.08	0.38M	2.7
WW *inclusive*	97232-97236	p17.09.08	0.96M	8.0
ZZ *inclusive*	106212-106216	p17.09.08	0.97M	1.1
$WZ \rightarrow 3l + \nu$	43930	p17.09.06	0.10M	0.1145
$W + X$ *inclusive*	42214-42218,38851-38860 37636-37640,35923-35927 35692-35696,35015-35019	p17.09.06	6.76M	1928
$t\bar{t}$	79192-79194	p17.09.08	0.49M	6.3

Table 5.8: DØ official p20 MC background samples used in the analysis. All samples were generated using PYTHIA v6.409.

sample	ReqId	d0release	Events
$\mathrm{Z}/\gamma^* \to \mathrm{e}^+\mathrm{e}^-$			
$15 - 60$ GeV	86887-86891,86898-86902	p20.09.03	1.83M
$60 - 130$ GeV	86882-86886,86893-86897,94342-94351	p20.09.03	3.51M
$130 - 250$ GeV	86892,94192-94194	p20.09.03	0.74M
$250 - 500$ GeV	94195-94198	p20.09.03	0.73M
500 GeV$-$	94199,94200	p20.09.03	0.37M
SM $\gamma\gamma$			
$50 - 130$ GeV	90252,90253,99619-99621	p20.09.03	0.81M
$130 - 250$ GeV	90254,99622-99625	p20.09.03	0.90M
250 GeV$-$	86512-86516	p20.09.03	0.87M
$\mathrm{Z}/\gamma^* \to \tau^+\tau^-$			
$60 - 130$ GeV	66012,66032,66033,66052,66072,67812	p20.08.02	2.70M
	86909-86913,91212-91214	p20.09.03	
$130 - 250$ GeV	66373	p20.08.02	0.80M
	86908,102142,102153	p20.09.03	
$250 - 500$ GeV	66375	p20.08.02	0.46M
	102143,102146	p20.09.03	
500 GeV$-$	66377	p20.08.02	0.46M
	102144,102145	p20.09.03	
$W\gamma$	88458,88459	p20.09.03	0.36M
WW inclusive	79613,79614	p20.09.02	0.70M
	86772,86773	p20.09.03	
ZZ inclusive	106184-106195	p20.09.03	2.18M
$WZ \to 3l + \nu$	88822,90376,90377	p20.09.03	0.36M
$W + X$ *inclusive*	88612-88616,89212-89221,89472-88476 89612-89616,89627-89631,89878-89887	p20.09.03	7.19M
$t\bar{t}$	86783-86786,88764,88766	p20.09.03	0.92M

in the data. The DØ EM ID group use samples of $Z \rightarrow e^+e^-$ to determine how much to smear the lepton energies in MC to match the width of the Z mass peak in data. In the package EMresolution_cafe, separate corrections are applied for EM objects near the ϕ-boundaries of calorimeter modules (NonPhiFiducial) and those away from the boundaries (PhiFiducial). For the NonPhiFiducial EM objects, additional EM energy scale corrections are derived from both data and MC $Z \rightarrow e^+e^-$ sample to reproduce the Z mass expectation from previous precision measurements. Figure 5.2 shows the e^+e^- invariant mass distributions in data and MC after the EM energy resolution correction and NonPhiFiducial energy scale correction, good agreement between data and MC is achieved.

5.3 Event Selection

The analysis is performed within the DØ package vjets_cafe v03-04-00. The event selection begins with requirements that are common to both dielectron and diphoton channels. After the common requirements, additional tracking-based cuts are made to split the sample into the two non-overlapping categories.

The common event selection required the presence of at least 2 EM objects which each satisfy the following cuts:

- $|\text{detector } \eta| < 1.1$
- $p_T > 25$ GeV
- iso < 0.2
- emfrac > 0.9

In the case that there are more than 2 EM objects satisfying these cuts, the two with highest p_T are considered further in the analysis. Table 5.9 shows, for several MC signal and background samples, the fraction of events with both EM objects in

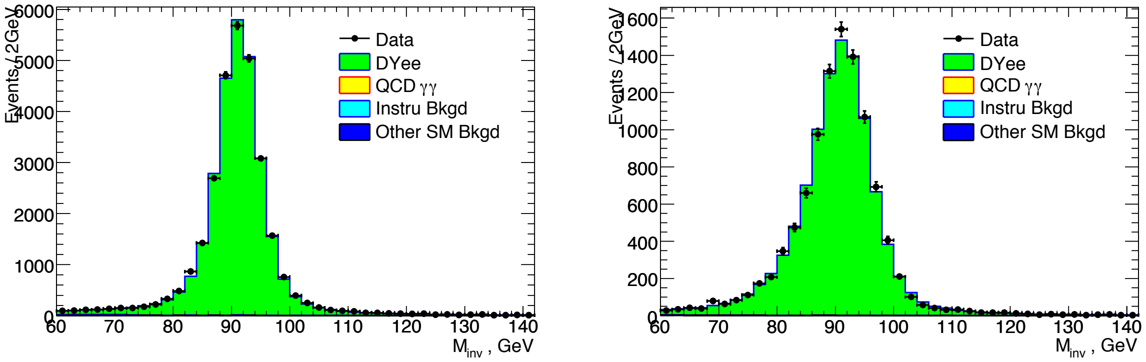

(a) p17 InIn (b) p17 Out

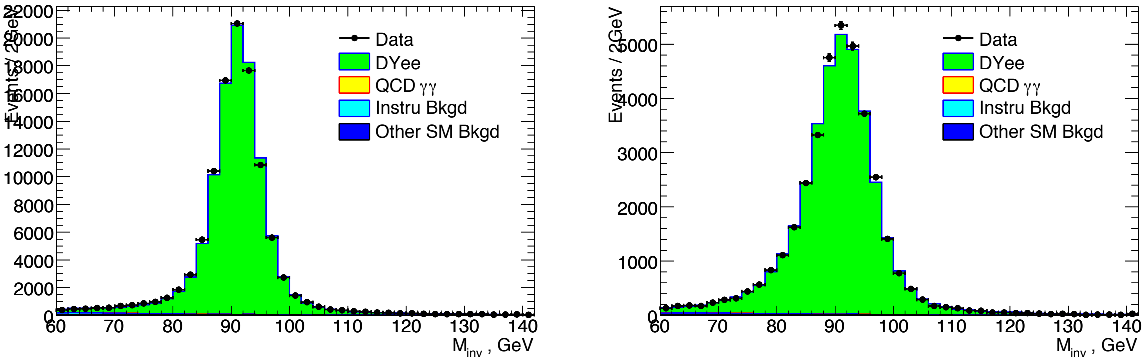

(c) p20 InIn (d) p20 Out

Figure 5.2: Invariant mass distribution for p17 and p20 Category I events for both in PhiFiducial (InIn) and at lease one in nonPhiFiducial (Out) events ($Z \rightarrow e^+e^-$ data and MC).

Table 5.9: Fraction of events with both EM objects in CC (CC-CC), one in CC and the other in EC (CC-EC), both in EC (EC-EC) with respect to all the generated events with both EM objects within $|\eta| < 5.0$.

Sample (10k events)	$CC - CC$	$CC - EC$	$EC - EC$
$\mathrm{G}^* \rightarrow \mathrm{e}^+\mathrm{e}^-$, 500 GeV	$58.4 \pm 0.5\%$	$9.8 \pm 0.3\%$	$5.4 \pm 0.2\%$
$\mathrm{G}^* \rightarrow \mathrm{e}^+\mathrm{e}^-$, 1 TeV	$63.1 \pm 0.5\%$	$2.4 \pm 0.3\%$	$10.1 \pm 0.3\%$
DY $\mathrm{e}^+\mathrm{e}^-[130\ \mathrm{GeV}, 250\ \mathrm{GeV}]$	$30.3 \pm 0.5\%$	$27.3 \pm 0.4\%$	$3.7 \pm 0.2\%$
$\mathrm{G}^* \rightarrow \gamma\gamma$, 500 GeV	$72.7 \pm 0.4\%$	$6.7 \pm 0.2\%$	$1.0 \pm 0.1\%$
$\mathrm{G}^* \rightarrow \gamma\gamma$, 1 TeV	$85.2 \pm 0.4\%$	$1.2 \pm 0.1\%$	$1.3 \pm 0.1\%$
SM $\gamma\gamma[130\ \mathrm{GeV}, 250\ \mathrm{GeV}]$	$6.8 \pm 0.3\%$	$12.2 \pm 0.3\%$	$4.8 \pm 0.2\%$

CC, as well as other possibilities. As can be seen, there is little gain in acceptance for decay products of massive gravitons by including showers in the endcap calorimeters (EC). In addition, the main SM backgrounds increase quite substantially if the EC is included. Therefore, the analysis is restricted to the central region.

We do not exclude EM objects in CC NonPhiFiducial regions. Including EM objects in the "ϕ-cracks" of the CC leads to a substantial ($\sim 20\%$) increase in signal acceptance.

After the first set of common event selection cuts, additional cuts are made to split the sample into two non-overlapping categories, as described below. Category I events are "dielectron-like", while Category II events are more "diphoton-like".

Category I Selection Cuts For the Category I definition, **BOTH** EM objects are required to pass the standard electron identification "MLoose1" requirements. The standard MLoose1 ID requirements include cuts that are common to both p17 and p20 samples, namely the following:

Calo cut : iso < 0.07, emfrac > 0.97, HMx7 < 25

TrkIso cut : IsoHC4 < 2.5 GeV

NN cut : NN7 > 0.2

In addition, there are standard tracking requirements that are slightly different for p17 and p20.

In p17 samples:

In p17 : "HasTrk"$=\chi^2_{\text{spatial}} > 0.0$ || HOR > 0.4, EOP < 4.0

In p20 samples:

In p20 : "HasTrk"$=\chi_{\text{spatial}} > 0.001$ || HOR > 0.4

In Category I, the "MLoose1" selection has an efficiency ∼90% in selecting electrons with p_T above 25 GeV. The selection efficiency was measured via the tag-and-probe method. The principle of the tag-and-probe method is that under the Z mass peak in data if one of the two EM objects in an event passes tight electron selection, the other EM object has a very high probability of coming from a real electron. The Data/MC scale factor of "MLoose1" efficiency is shown in Figure 5.3.

For photons in Category-I, we selected $Z \to \mu^+\mu^-\gamma$ events from the data to measure the photon Data/MC scale factors of EM ID efficiency. A loose muon selection criteria was used in selecting events with two muon objects. In addition, the photon was required to have $E_T > 15$ GeV and to be away from either muon object by dR > 0.2. The invariant mass distributions of selected events are shown in Figure 5.4 (p17 data) and Figure 5.5 (p20 data). Only events with three-body invariant mass between 82 GeV and 102 GeV were considered for the efficiency measurement. The "MLoose1" efficiency scale factors for a single photon are summarized in Table 5.10

Category II Selection Cuts As described above, events in Category I require that both EM objects pass some track quality cuts. To avoid any overlap, the Category II definition requires that AT LEAST ONE of the two EM objects fails the electron "HasTrk" requirement. Instead, at lease one of the two EM objects must satisfy

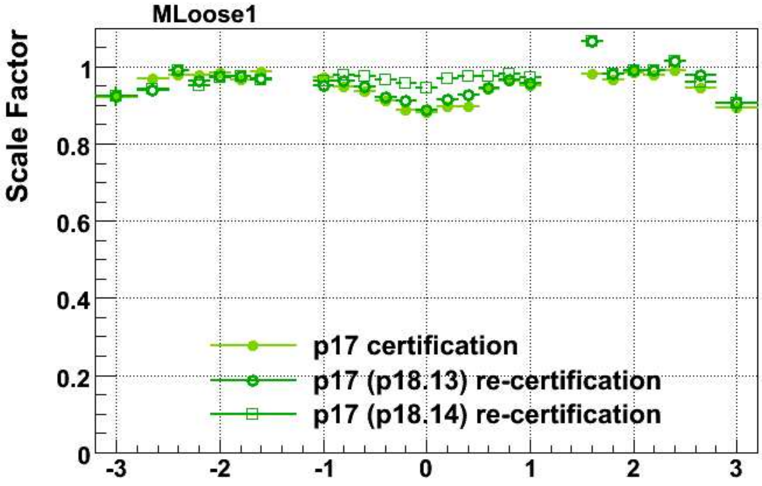

(a) RunIIa

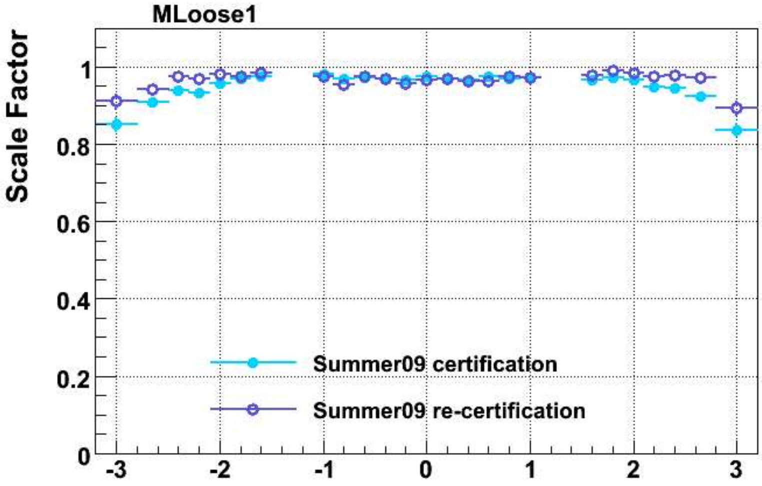

(b) RunIIb

Figure 5.3: Scale factor of "MLoose1" selection for electrons.

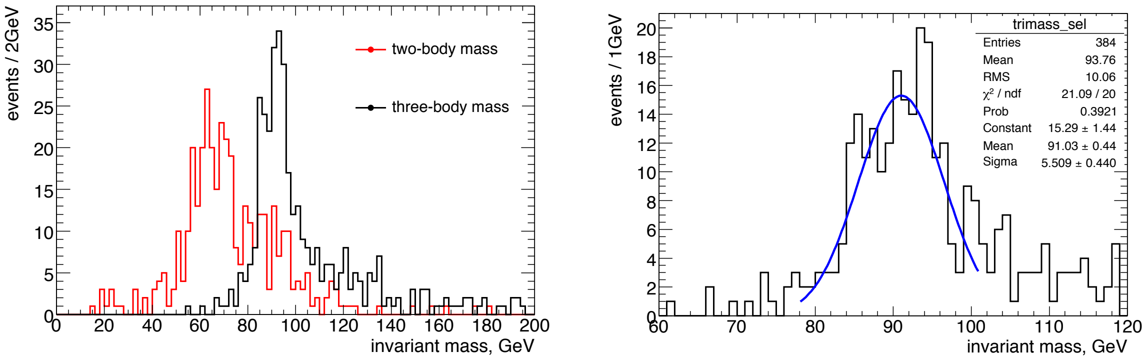

Figure 5.4: Two-body and three-body invariant mass distributions for p17 $\mu^+\mu^-\gamma$ events (left) and a Gaussian fit to the three-body invariant mass Z peak(right)

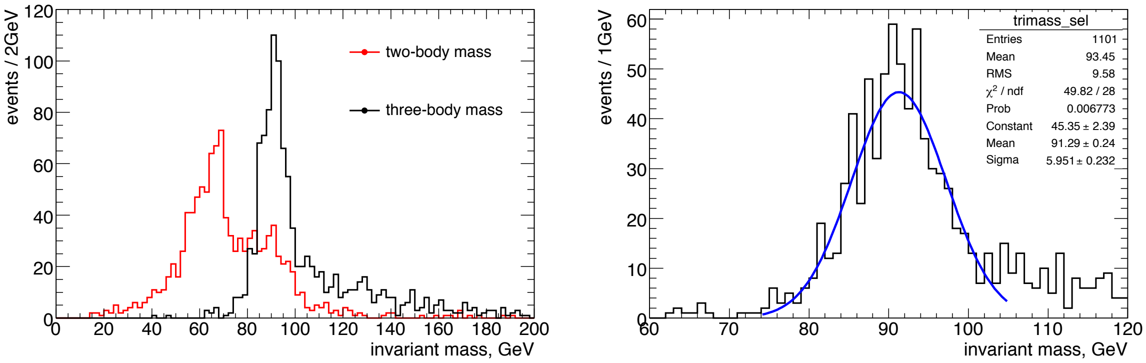

Figure 5.5: Two-body and three-body invariant mass distributions for p20 $\mu^+\mu^-\gamma$ events (left) and a Gaussian fit to the three-body invariant mass Z peak(right)

Table 5.10: Efficiency and scale factor for photon in Category I selection.

Samples	p17	p20
$\gamma\gamma$ MC	0.072 ± 0.002	0.162 ± 0.002
$Z \rightarrow \mu^+\mu^-\gamma$ Data	0.079 ± 0.016	0.168 ± 0.013
scale factor	1.10 ± 0.23	1.09 ± 0.23

Table 5.11: Efficiencies and scale factors of electron and photon Calo and IsoTrk cuts for p17 and p20. In p17, the p_T dependence of the scale factor is modeled as $0.5 \cdot \mathrm{p_0} \cdot (1.0 + \mathrm{TMATH :: Erf((E_T - p_1)/(\sqrt{2} \cdot p_2))}) \pm 0.010$, where $p_0 = 0.977$, $p_1 = -1.13$, $p_2 = 19.3$.

Samples	p17		p20	
	Calo	IsoTrk	Calo	IsoTrk
MC	0.930 ± 0.001	0.972 ± 0.001	0.918 ± 0.001	0.971 ± 0.001
Data	0.896 ± 0.002	0.971 ± 0.001	0.890 ± 0.002	0.964 ± 0.001
scale factor	function	0.999 ± 0.001	0.97 ± 0.01	0.993 ± 0.004

a “NoTrk” requirement (i.e. the inverse of the HasTrk definition above) as defined below:

In p17 : “NoTrk”=$\chi^2_{\text{spatial}} \leq 0$ && HOR < 0.4

In p20 : “NoTrk”=$\chi^2_{\text{spatial}} < 0.001$ && HOR < 0.4

Each of the EM objects must also satisfy the following additional requirements:

Calo cuts : emfrac > 0.97, iso < 0.07, sigphi $< 14\text{cm}^2$, HMx7 < 30 (for p17 only to remove warm events)

TrkIso cut : IsoHC4 < 2.0 GeV

NN cut : NN5 > 0.1

For the Category II selection criteria, the scale factors for Calo and TrkIso efficiencies are shown in Table 5.11.

In this analysis, we measured the photon and electron track and NN efficiencies and the corresponding scale factors. The photon sample comes from $Z \to \mu^+\mu^-\gamma$ events as described above. Table 5.12 gives the efficiencies and scale factors of the “NoTrk” selection in p17 and p20 for a single photon.

Table 5.12: Efficiency and scale factor for photon “NoTrk” after Calo and TrkIso Cuts.

Samples	p17	p20
$\gamma\gamma$ MC	0.899 ± 0.002	0.760 ± 0.002
Z $\rightarrow \mu^+\mu^-\gamma$ Data	0.900 ± 0.020	0.718 ± 0.020
scale factor	1.000 ± 0.020	0.945 ± 0.020

Table 5.13: Efficiencies and scale factors of photon NN cut for p17 and p20.

Samples	p17		p20	
	NoTrk	HasTrk	NoTrk	HasTrk
$\gamma\gamma$ MC	0.978 ± 0.001	0.832 ± 0.009	0.980 ± 0.001	0.905 ± 0.003
$\mu^+\mu^-\gamma$ Data	0.974 ± 0.011	0.818 ± 0.082	0.982 ± 0.006	0.927 ± 0.019
scale factor	1.00 ± 0.01	0.98 ± 0.08	1.00 ± 0.01	1.02 ± 0.02

The neural net variable $NN5$ is sensitive to the track requirement and its efficiency and scale factor were measured for “HasTrk” and “NoTrk” cases, as summarized in Table 5.13 (for photons).

The electron sample comes from $Z \rightarrow e^+e^-$ events selected via the tag-and-probe method as described above. Table 5.14 and Table 5.15 give the efficiencies and scale factors of “NoTrk” and “NN”selection in p17 and p20 for a single electron.

In the p20 MC sample, the electron “notrk” efficiency has an sudden increase for physics η close to 0, as shown in Figure 5.8. This behavior is corrected by reweighting the MC to reproduce the results observed with data.

We noticed that there is some $\eta_{detector}$ dependence of Data/MC scale factors for the NN cut as shown in Figure 5.9. The $\eta_{detector}$ dependence is parameterized and applied to correct the MC samples.

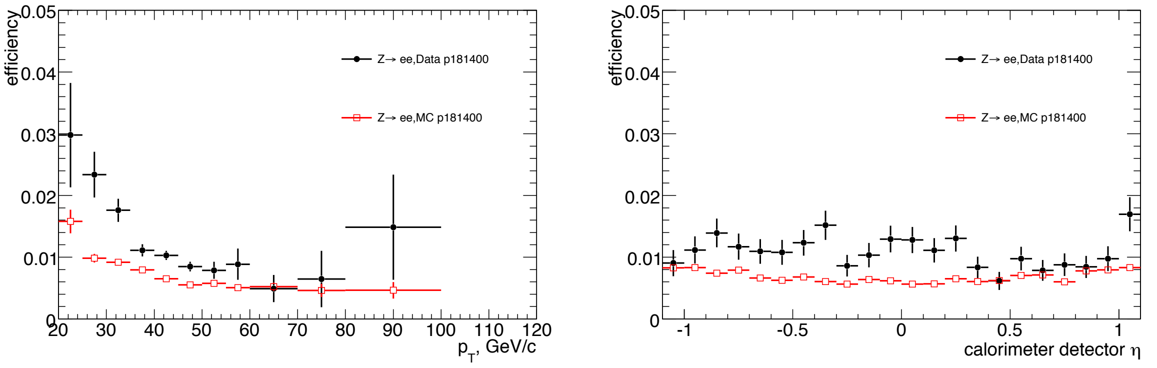

(a) p_T, GeV (b) $Eta_{detector}$

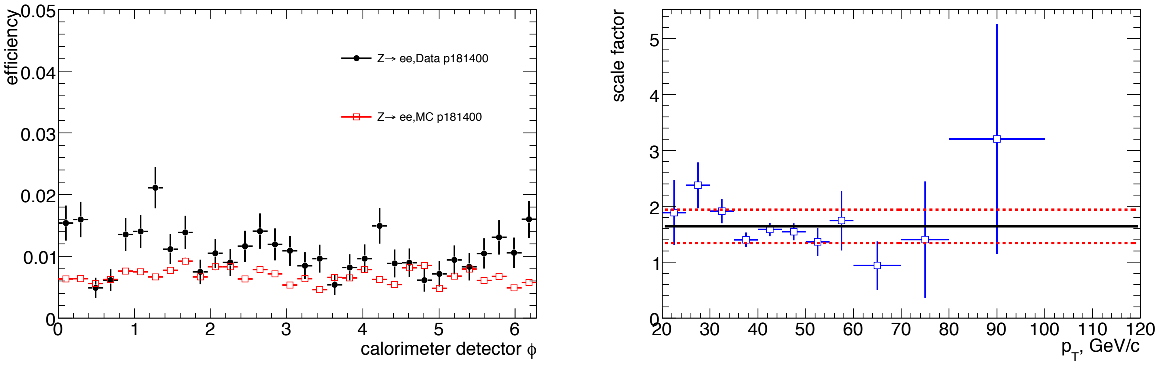

(c) $Phi_{detector}$ (d) $scalefactor$

Figure 5.6: Electron “notrk” efficiency and scale factor in p17.

Table 5.14: Efficiency and scale factor for electron “NoTrk” after Calo and TrkIso Cuts.

Samples	p17	p20
Zee MC	0.0067 ± 0.0001	0.0119 ± 0.0001
Zee Data	0.0110 ± 0.0004	0.0110 ± 0.0002
scale factor	1.64 ± 0.3	0.92 ± 0.1

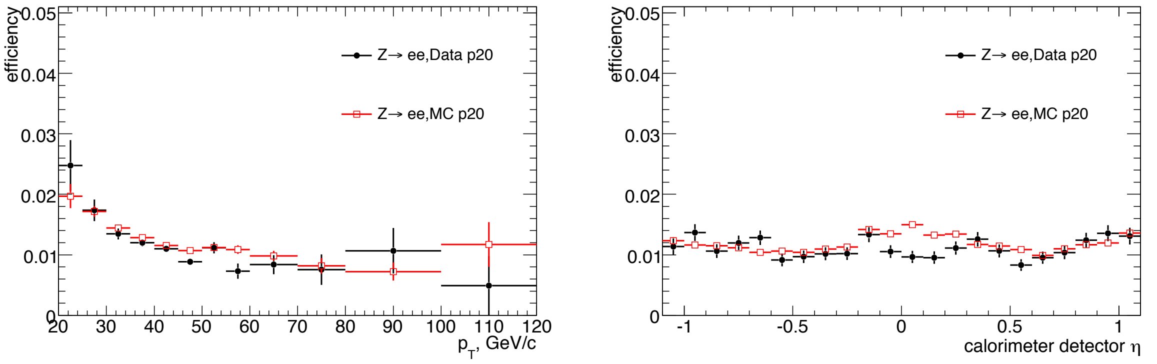

(a) p_T, GeV

(b) $Eta_{detector}$

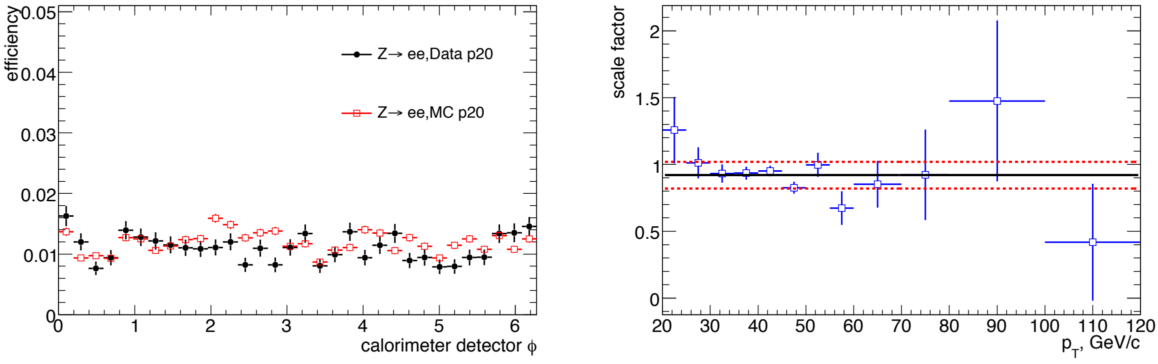

(c) $Phi_{detector}$

(d) $scalefactor$

Figure 5.7: Electron "notrk" efficiency and scale factor in p20.

Table 5.15: Efficiencies and scale factors of electron NN cut for p17 and p20.

Samples	p17		p20	
	NoTrk	HasTrk	NoTrk	HasTrk
Zee MC	0.776 ± 0.006	0.952 ± 0.001	0.845 ± 0.003	0.952 ± 0.001
Zee Data	0.811 ± 0.016	0.908 ± 0.001	0.825 ± 0.008	0.947 ± 0.001
scale factor	1.05 ± 0.02	0.95 ± 0.01	0.98 ± 0.01	0.99 ± 0.01

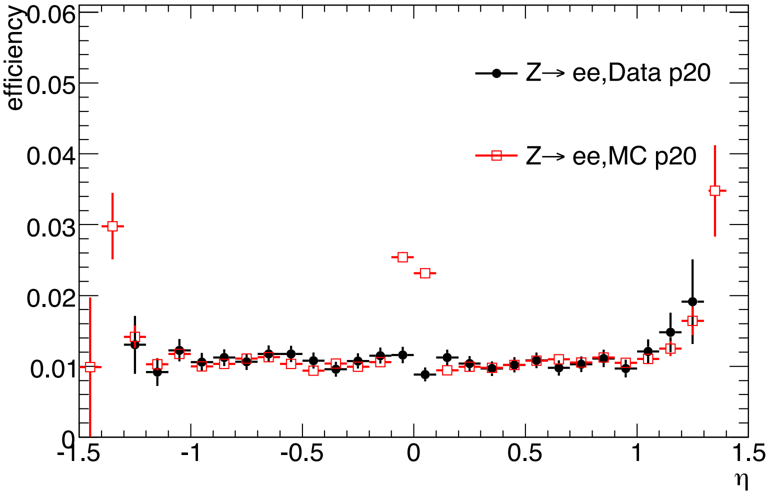

Figure 5.8: Electron "notrk" efficiency as a function of physics η in p20.

5.4 Primary Vertex Selection

In Category I, the primary vertex is picked as the one with the least probability of being a vertex in minimum-bias events. The z-coordinate of the vertex is required to be within 60 cm of the geometrical center of the detector.

For Category II, the diphoton final state dominates, and it is necessary to assign the photons to the correct vertex in order to ensure the diphoton invariant mass is properly calculated. In this case, three different primary vertex selection algorithms were investigated. The first is the default, namely choosing the vertex with the smallest probability of being a minimum bias vertex [52]. The second method, dubbed "maxtrk", selects the vertex to which the maximum number of tracks was associated. The final method uses CPS pointing information [53]. If both photons in the final state have matched CPS clusters, the extrapolated z-positions from CPS pointing are required to lie within 10 cm of each other, and the vertex closest and within 7 cm from their average is chosen as the primary vertex. If only one photon has a matching CPS cluster, the vertex closest to it and within 10 cm is chosen as the primary vertex. In case that neither of the two photons have CPS matches, the primary vertex is chosen

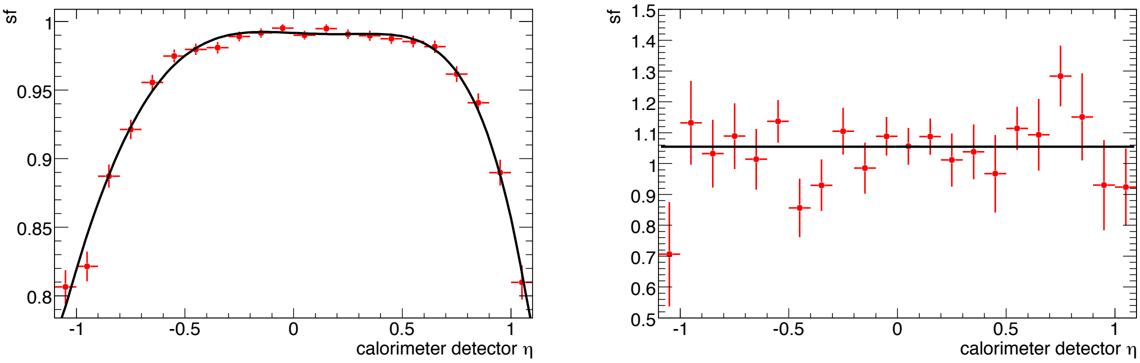

(a) p17 "HasTrk"

(b) p17 "NoTrk"

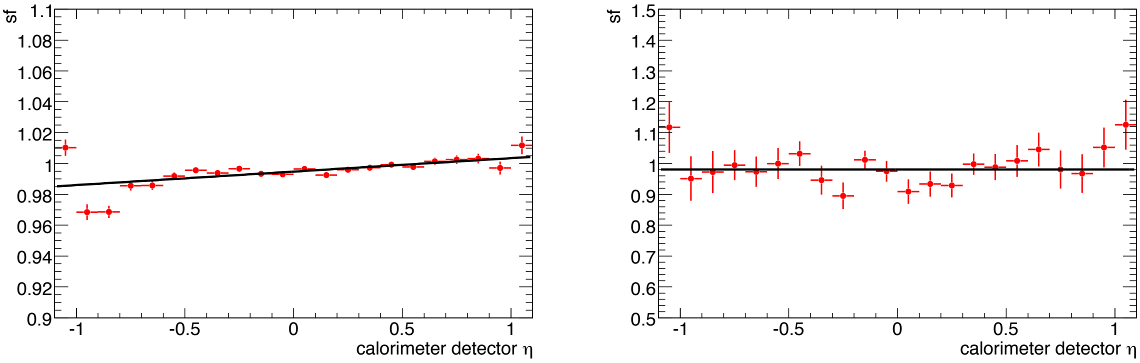

(c) p20 "HasTrk"

(d) p20 "NoTrk"

Figure 5.9: Data/MC scale factors for $NN5 > 0.1$ cut. The fitting function of p17 "HasTrk" is $p_0 + p_1 x + p_2 x^2 + p_3 x^3 + p_4 x^4 + p_5 x^5$ where $p_0 = 9.91588e - 1$, $p_1 = -7.321436e - 3$, $p_2 = 6.1077e - 4$, $p_3 = 1.056588e - 1$, $p_4 = -1.544973e - 1$ and $p_5 = -7.969381e - 2$. The fitting function of p20 "HasTrk" is $p_0 + p_1 x$ where $p_0 = 9.947522e - 1$ and $p_1 = 8.714454e - 3$.

as the one from the "maxtrk" method. In this analysis, we use this "cpsmatch" algorithm to identify the primary vertex for Category II events.

Figure 5.10 illustrates the performance of the various primary vertex selection algorithms, as applied to 500 GeV $G^* \rightarrow \gamma\gamma$ MC events. The plots, made separately for p17 and p20, show the difference in the z-position of the identified primary vertex and the generated (ie. true) primary vertex, and the resultant diphoton invariant mass distribution. The probability of the identified primary vertex lying within 2 cm of the generated one increases from $85.7 \pm 0.3\%$ ($71.5 \pm 0.4\%$) for the "default" algorithm to $94.7 \pm 0.2\%$ ($91.9 \pm 0.2\%$) for the "cpsmatch" algorithm in p17 (p20). In events where the default vertex was not chosen, the four-vectors of the two photons were recalculated using the selected primary vertex. The corresponding invariant mass distribution is narrower for the "cpsmatch" algorithm than for the default one, confirming the improvement achieved in the diphoton mass reconstruction. For p17, the value of sigma returned from a Gaussian fit to the invariant mass distribution is improved from 11.9 ± 0.1 GeV for the "default" vertex to 11.5 ± 0.1 GeV for "cpsmatch" vertex algorithm. For p20, the corresponding improvement is from 12.3 ± 0.1 GeV ("default") to 11.4 ± 0.1 GeV ("cpsmatch").

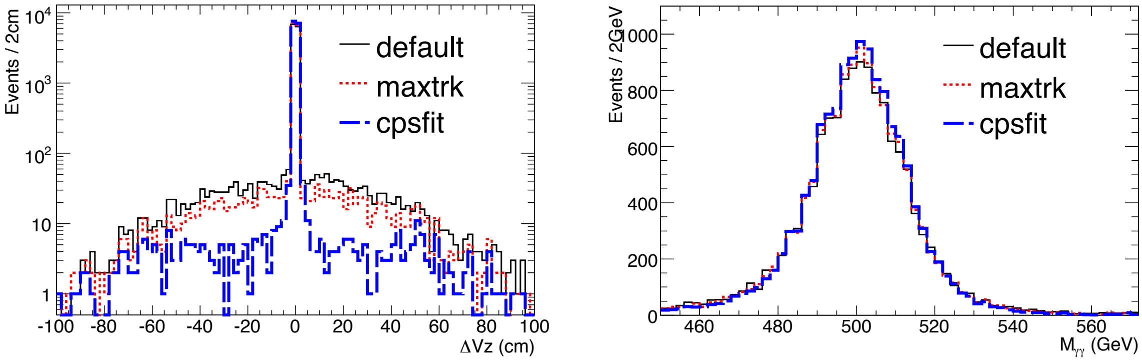

(a) p17 (b) p17

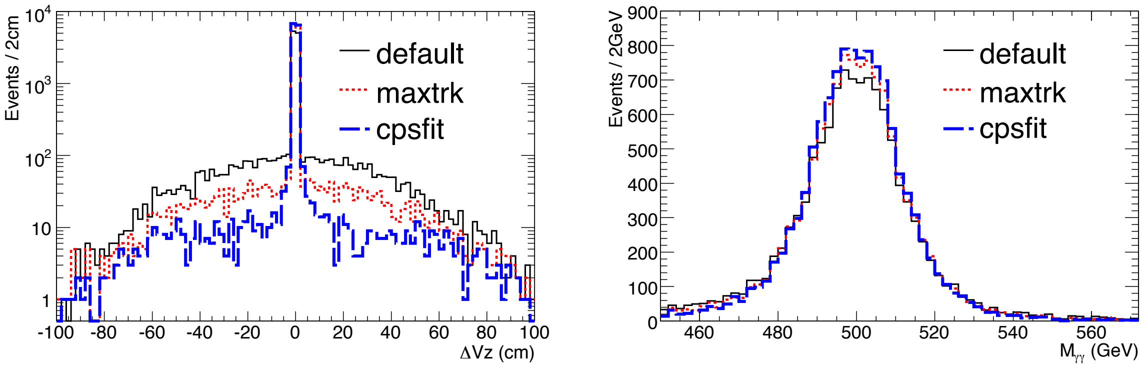

(c) p20 (d) p20

Figure 5.10: For the 500 GeV $G^* \rightarrow \gamma\gamma$ MC sample, the left plots show the difference between the z-position of the true primary vertex and that selected by the three vertex selection algorithms. The right plots show the diphoton invariant mass distribution, as recalculated using the vertex selected by the three algorithms. The top row of plots are for p17 and the bottom row are for p20.

Chapter 6

Graviton Signal Studies

Monte Carlo samples were generated for RS graviton decays to dielectron and diphoton final states. A total of 19 different graviton mass values, ranging from 220 GeV to 1050 GeV, were simulated. The LO cross section multiplied by the branching ratio to e^+e^- from PYTHIA is listed in Table 6.1 for the various MC signal samples. For the analysis, a NLO k-factor of 1.54 [54] on the graviton production is used.

Some plots of the kinematics of the decay daughters for 500 GeV graviton to e^+e^- and $\gamma\gamma$ events are shown in Figure 6.1, 6.2 and 6.3. As can be seen, the decay daughters are produced centrally, with a transverse momentum which is roughly half the graviton mass. The transverse momentum of the graviton is typically small, so the difference in ϕ between the two daughters is peaked at a value of π.

Table 6.2 shows the selection efficiency for a 500 GeV graviton with coupling 0.02 for p17. Table 6.3 shows the same for p20.

As can be seen from the tables, the Category I cuts select mostly the dielectron final state, while Category II selects mostly the diphoton final state. Plots of the selection efficiency as a function of graviton mass are shown in Figure 6.4.

For very heavy gravitons, the decay of which would typically lead to very highly energetic electrons and photons, one has to take into account possible saturation effects in the readout of the calorimeter. We have investigated the impact using a

Table 6.1: Natural width of the graviton (from Breit-Wigner fitting) and its mass resolution (in e^+e^- channel from Gaussian fitting) for the PYTHIA MC signal samples.

Graviton Mass GeV	Coupling $k/\overline{M}_{\rm Pl}$	Natural Width GeV	Mass Resolution (e^+e^-) GeV
220	0.01	0.030±0.002	5.70±0.07
250	0.01	0.034±0.002	6.33±0.07
270	0.01	0.040±0.002	6.72±0.08
300	0.01	0.042±0.002	7.3±0.1
350	0.01	0.050±0.002	8.3±0.1
400	0.01	0.056±0.002	8.8±0.1
450	0.01	0.064±0.002	10.0±0.1
500	0.02	0.28±0.01	11.2±0.1
550	0.02	0.31±0.01	11.8±0.2
600	0.02	0.34±0.01	12.7±0.2
650	0.02	0.36±0.01	14.2±0.2
700	0.02	0.39±0.01	15.0±0.2
750	0.03	0.96±0.02	15.9±0.2
800	0.03	1.06±0.02	16.6±0.2
850	0.05	2.9±0.1	18.4±0.2
900	0.05	3.1±0.1	19.5±0.2
950	0.07	6.6±0.2	22.1±0.2
1000	0.10	14.8±0.2	24.6±0.3
1050	0.10	16.6±0.2	27.6±0.3

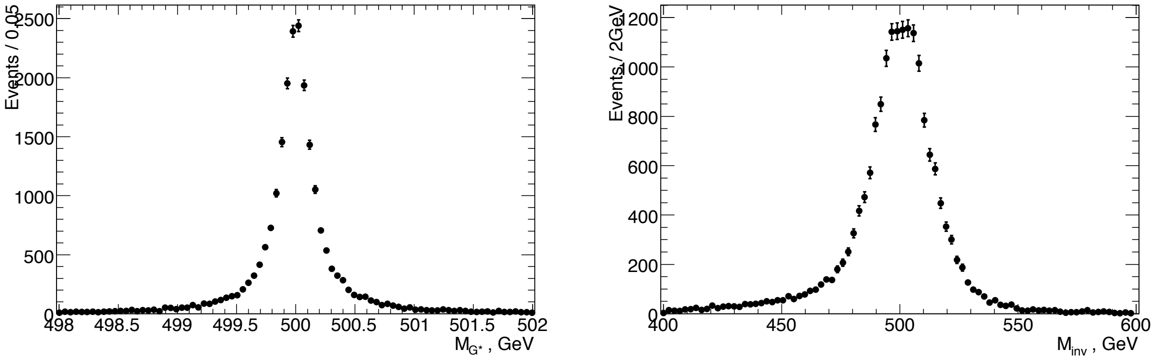

Figure 6.1: The generated (left) and reconstructed (right) invariant mass spectra for an RS graviton of mass 500 GeV and coupling $k/\overline{M}_{\rm Pl} = 0.02$. Note that the horizontal scales for the two figures are different.

Table 6.2: Selection efficiency for a 500 GeV graviton for p17.

Selection Efficiency %	Graviton 500 GeV 0.02			
Channel	e^+e^-		$\gamma\gamma$	
Data Quality	97.0 ± 0.1		96.6 ± 0.1	
Preselection	52.0 ± 0.3		63.6 ± 0.3	
	Category I	Category II	Category I	Category II
Category Splitting	97.3± 0.1	2.7± 0.1	1.6± 0.1	98.4± 0.1
Vertex Selection	98.8 ± 0.1	97.7 ± 0.8	97.6 ± 1.0	98.7 ± 0.1
EM ID	78.5± 0.4	42.8± 2.7	15.2± 2.3	76.2± 0.3
Total	38.1± 0.3	0.57± 0.05	0.15± 0.02	45.4±0.3

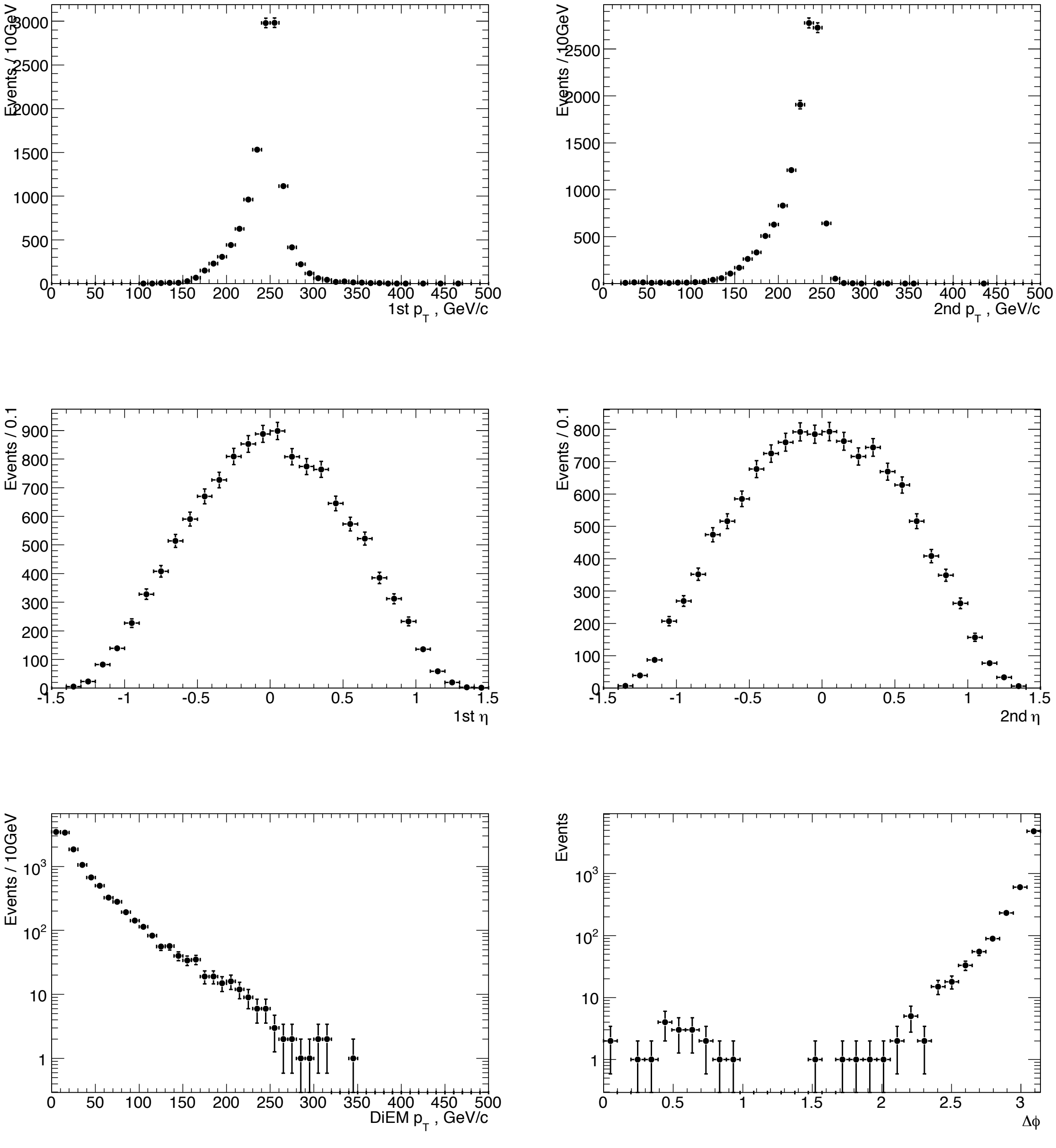

Figure 6.2: Various distributions for 500 GeV $G^* \rightarrow e^+e^-$ events, including the transverse momentum and η of the leading and second leading electrons, the transverse momentum of the dielectron system, and the difference in ϕ between the two electrons.

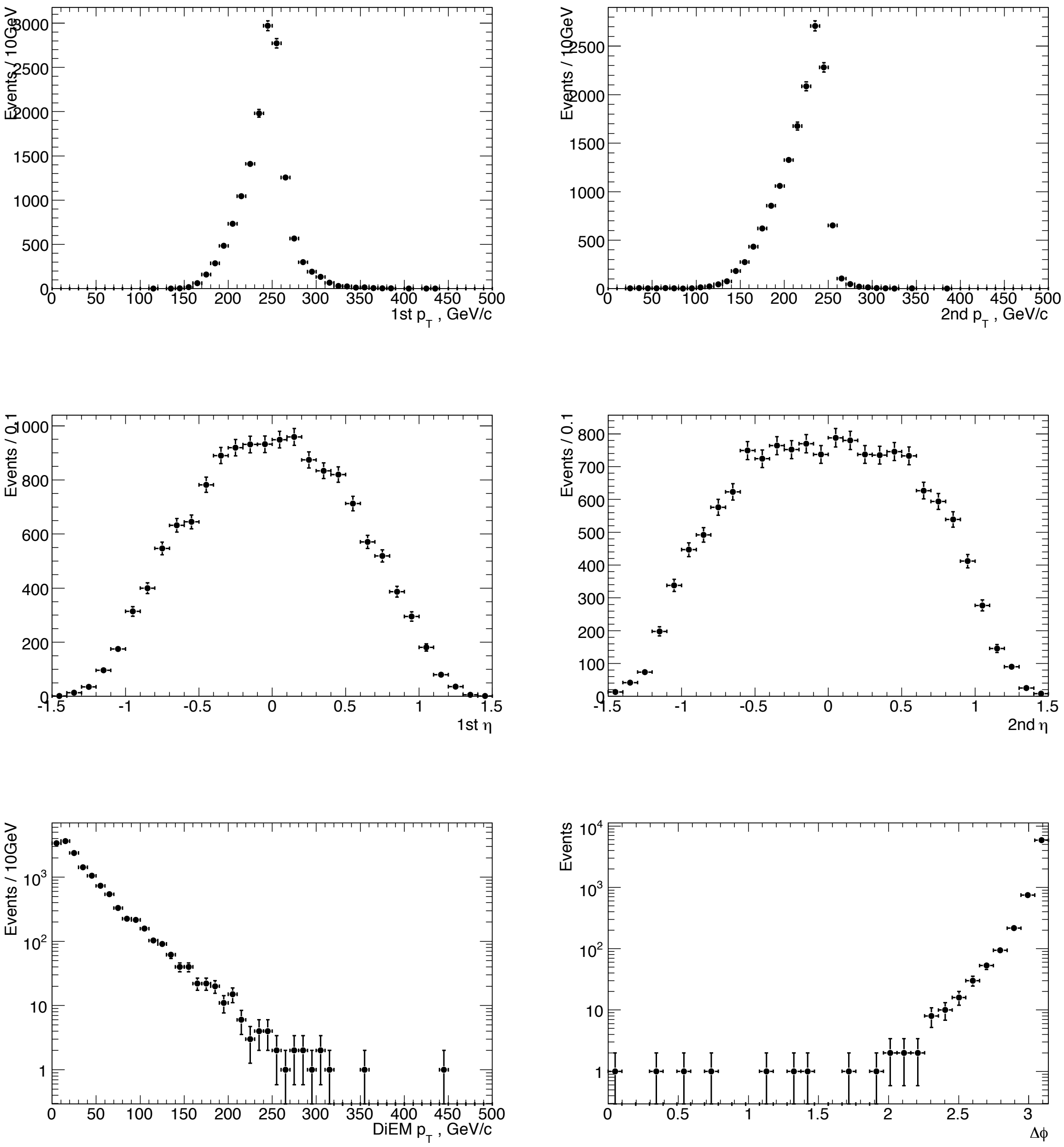

Figure 6.3: Various distributions for 500 GeV $G^* \rightarrow \gamma\gamma$ events, including the transverse momentum and η of the leading and second leading photons, the transverse momentum of the diphoton system, and the difference in ϕ between the two photons.

Table 6.3: Selection efficiency for a 500 GeV graviton for p20.

Selection Efficiency %	Graviton 500 GeV 0.02			
Channel	e^+e^-		$\gamma\gamma$	
Data Quality	96.5 ± 0.1		96.9 ± 0.1	
Preselection	52.6 ± 0.3		63.7 ± 0.3	
	Category-I	Category-II	Category-I	Category-II
Category Splitting	96.6± 0.2	3.4± 0.2	10.4± 0.3	89.6± 0.3
Vertex Selection	98.5 ± 0.1	98.1 ± 0.7	98.1 ± 0.3	98.8 ± 0.1
EM ID	82.6± 0.3	55.6± 2.5	16.0± 1.0	81.8± 0.3
Total	39.9± 0.3	0.94± 0.06	1.01± 0.07	44.8±0.3

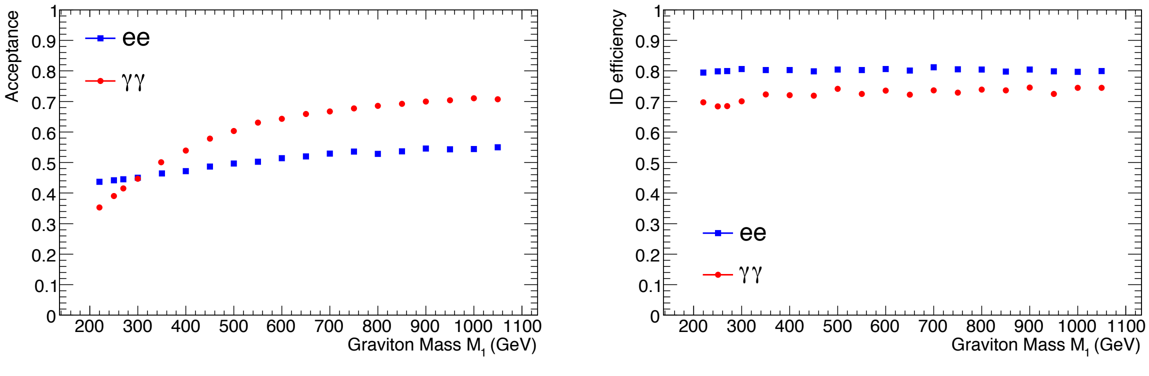

(a) acceptance

(b) EM ID efficiency

Figure 6.4: Signal acceptance and EM ID efficiency, as a function of graviton mass.

parametrization [55] [56] of the saturation level (i.e. highest possible signal) for each cell of the calorimeter. For the signal MC samples, we compare the energy of each cell of an EM cluster with its saturation energy level. If the deposited energy in a given cell according to the MC is higher than the saturation value of that cell, then the energy in that cell is set by hand to the saturation value.

After applying these "saturation corrections", a saturation scale is derived for each cluster from the ratio of the saturation-corrected cluster energy to the original cluster energy:

$$Scale_{saturation} = \frac{E1_{corr} + E2_{corr} + E3_{corr} + E4_{corr}}{E1 + E2 + E3 + E4} \tag{6.1}$$

Here $E1$, $E2$, $E3$ and $E4$ are the summations of energies of cells of EM calorimeter layers 1, 2, 3 and 4 respectively. $E1_{corr}$ is similar but refers to the saturation-corrected cell energies, and likewise for $E2_{corr}$, $E3_{corr}$ and $E4_{corr}$. The diEM invariant mass is then corrected by this scale via the following equation:

$$M_{inv}(corrected) = M_{inv} \times \sqrt{Scale_{saturation}(obj_1) \cdot Scale_{saturation}(obj_2)} \tag{6.2}$$

Figure 6.5 shows, for 1 TeV gravitons, the distributions of deposited energies in each of the calorimeter layers, both without and with these saturation corrections. Clear differences are visible.

Figure 6.6 shows the impact of saturation effects on the reconstruction of the mass of the graviton, where the impact becomes visible for gravitons with mass above ∼700 GeV. The effect is quite pronounced for the highest mass graviton shown (1050 GeV), resulting in a reconstructed mass distribution that has both a lower peak position and a wider resolution than would otherwise be expected. We also tested the saturaction effects on the EM identification algorithms, but they have negligible impact.

The size of the effect is visualized in Figure 6.7 by plotting the mean and sigma from applying a Gaussian fit to the reconstructed graviton mass, and comparing the results with and without saturation. Note that this is for illustration purposes only,

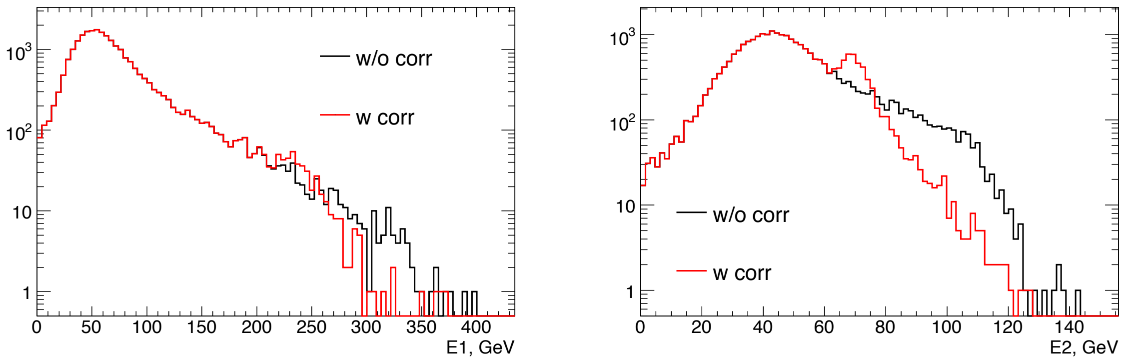

(a) E1

(b) E2

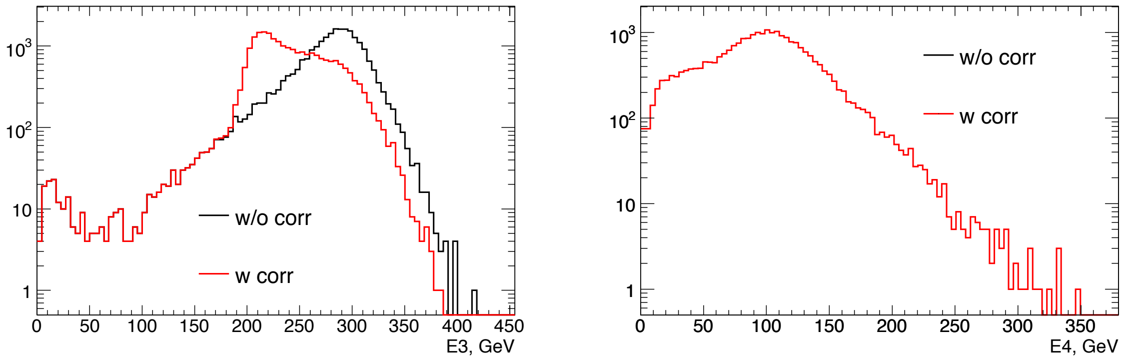

(c) E3

(d) E4

Figure 6.5: Energy in different calorimeter layers of electrons from 1TeV graviton decay with and without saturation effect corrections.

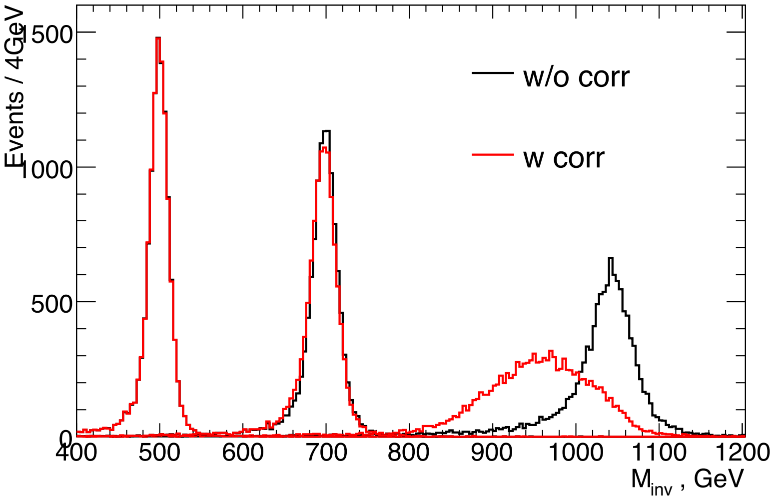

Figure 6.6: Dielectron invariant mass distributions expected for (from left to right) 500 GeV, 700 GeV and 1050 GeV gravitons, with and without corrections to model calorimeter saturation effects.

since the limit calculation (see later) uses the full shape of the signal and not the result of a Gaussian signal description.

For the remainder of the analysis, the invariant mass as reconstructed including the effects of saturation is used for both signal MC and background MC samples in the search.

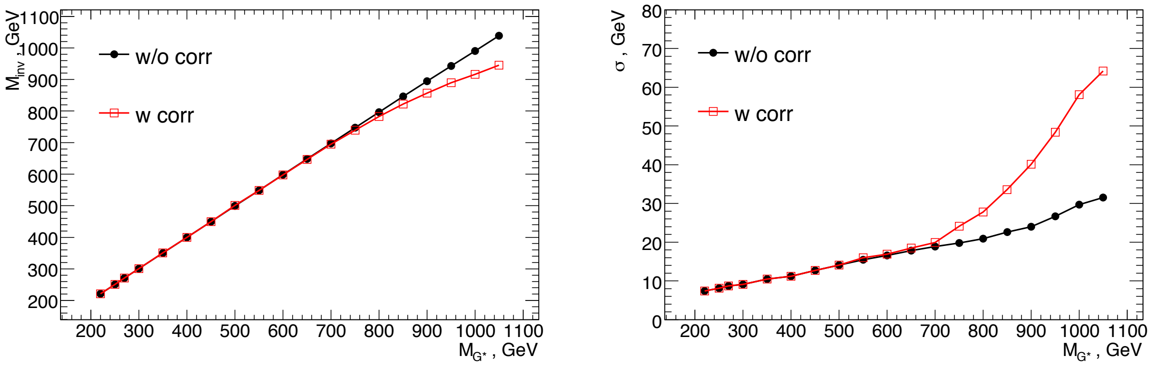

Figure 6.7: A Gaussian fitted mean (left) and sigma (right) of the reconstructed diEM invariant mass distribution with and without corrections to model calorimeter saturation effects.

Chapter 7

Background Estimation and Systematic Uncertainties

The total background is comprised of physics backgrounds, mostly DY e^+e^- and direct $\gamma\gamma$ production (see Figure 7.1), and instrumental backgrounds in which one or both of the EM objects are misidentified.

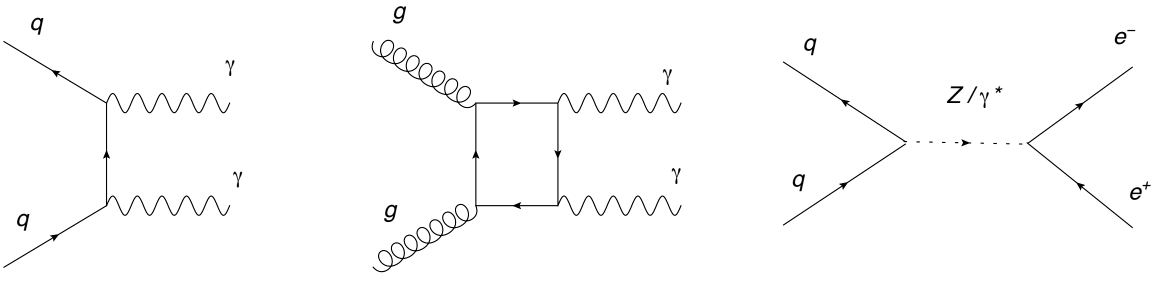

Figure 7.1: The SM $\gamma\gamma$ and e^+e^- production Feynman diagrams simulated in PYTHIA.

7.1 Shapes of the Physics Background Distributions

SM DY e^+e^- The spectra of the DY process are estimated from PYTHIA MC samples. The shape of the invariant mass spectrum expected from the next-to-next-to-leading order (NNLO) cross section is obtained by multiplying the LO cross section by a mass-dependent k-factor [57], as seen in Figure 7.2.

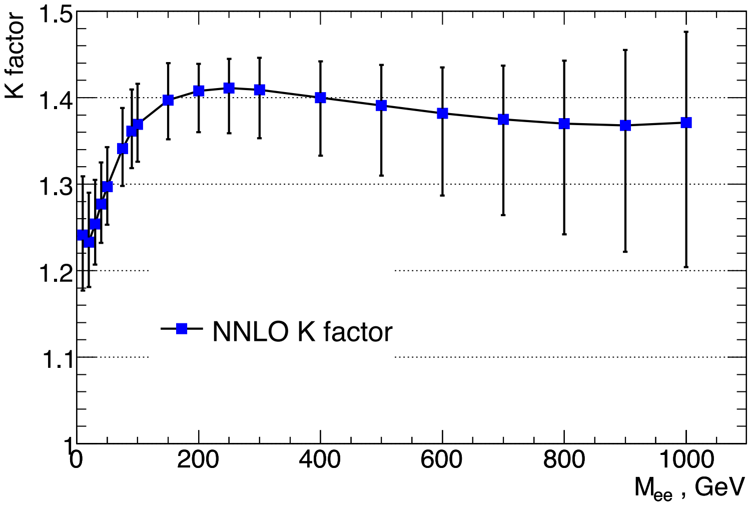

Figure 7.2: The NNLO k-factor used for the DY e^+e^- process.

In addition, Z p_T reweighting [58] is applied on the DY e^+e^- and $\tau^+\tau^-$ MC samples, since the generated p_T spectrum of the Z boson in PYTHIA does not agree perfectly with the observed spectrum in data.

SM $\gamma\gamma$ The shapes of the direct $\gamma\gamma$ background distributions are also estimated from PYTHIA. The LO distributions are then corrected by a mass dependent factor derived from the DIPHOX NLO package [59]. DIPHOX computes a full NLO diphoton cross section as a function of diphoton invariant mass. The cross sections from DIPHOX and PYTHIA, as well as the ratio between them, are shown in Figure 7.3. The ratio is fitted with a functional form parametrized as

$$\begin{cases} \mathrm{p0} + \mathrm{p1}\cdot(\mathrm{M}_{\gamma\gamma}-90) + \mathrm{p2}\cdot(\mathrm{M}_{\gamma\gamma}-90)^2 + \mathrm{p3}\cdot(\mathrm{M}_{\gamma\gamma}-90)^3, & \mathrm{M}_{\gamma\gamma} < 90 \\ \mathrm{p0} + \exp[\ \mathrm{p4}\cdot(\mathrm{M}_{\gamma\gamma}-90) + \mathrm{p5}\cdot(\mathrm{M}_{\gamma\gamma}-90)^2] - 1, & \mathrm{M}_{\gamma\gamma} > 90. \end{cases} \tag{7.1}$$

where p0 = 1.71726, p1 = -1.44793e-02, p2 = -1.05832e-03, p3 = -1.11511e-05, p4 = -4.10934e-03, and p5 = 2.45821e-06. The ratio decreases with increasing diphoton invariant mass, and the correction is typically less than 20% in the signal search region.

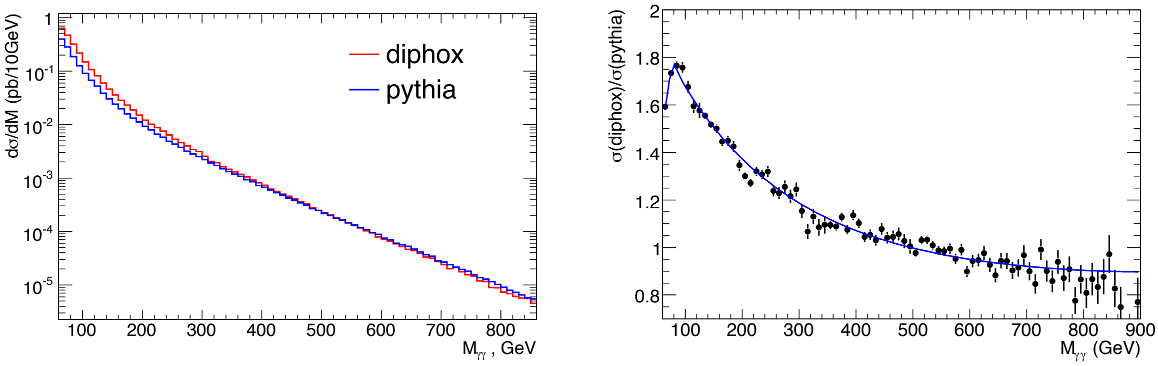

Figure 7.3: Cross sections for SM $\gamma\gamma$ production as a function of diphoton invariant mass from PYTHIA and DIPHOX (left) and their ratio (right). At the generator level, the photons are restricted to the calorimeter central region ($|\eta| < 1.1$) with $E_T > 25$ GeV.

In the DIPHOX calculation, we estimate the uncertainty due to the choices of the renormalization scale μ, of the initial state factorization scale M (which enters in the parton distribution functions), and of the fragmentation scale M_f. The default choice is $\mu = M = M_f = m_{\gamma\gamma}$, where $m_{\gamma\gamma}$ is the diphoton invariant mass. We compare four other choices of scales: two choices along the first diagonal $\mu = M = M_f = m_{\gamma\gamma}/2$ and $\mu = M = M_f = 2m_{\gamma\gamma}$; and two anti diagonal choices, $\mu = m_{\gamma\gamma}/2$ $M = M_f = 2m_{\gamma\gamma}$ and $\mu = 2m_{\gamma\gamma}$ $M = M_f = m_{\gamma\gamma}/2$. In this analysis, the SM $\gamma\gamma$ is normalized by fitting to the data in the control region. The systematic uncertainty is therefore the allowed variation after normalization. As shown in Figure 7.4, the anti diagonal choices give larger shape differences after normalization than the diagonal choices.

With the different choices of DIPHOX scales, we evaluate the effect on the background. Figure 7.5 shows the corresponding scale factors of DIPHOX/PYTHIA and the variation of the total expected background. These variations are accounted for in the systematic errors. As described in Appendix A, we have also performed a cross-check where a two-dimensional reweighting of the PYTHIA events to the diphoton invariant mass and diphoton p_T distributions was used. However, the resultant variations were small and fall within the variations above.

We also compared DIPHOX with another NLO $\gamma\gamma$ calculation from RESBOS [60]. The comparison shows that the difference between RESBOS and DIPHOX in the $\gamma\gamma$ invariant mass distribution is within the DIPHOX uncertainties, as shown in Figure 7.6.

7.2 Shapes of the Instrumental Background Distributions

The shapes of the instrumental backgrounds are estimated from a subsample of the preselected data in which at least one EM object is inconsistent with an electromagnetic shower.

For Category I events, the instrumental background sample is selected by reversing the HMx7 cut, requiring that both EM objects satisfy iso<0.07, emfrac>0.97 and HMx7 > 25.

Reversing the H-matrix cut was shown to introduce negligible kinematic bias. Jet-faked EM objects were selected from the data via the tag-and-probe method by selecting events with two same-sign EM objects, one of them failing the showershape cut (tag) and the invariant mass of the two EM objects away from the Z mass peak.

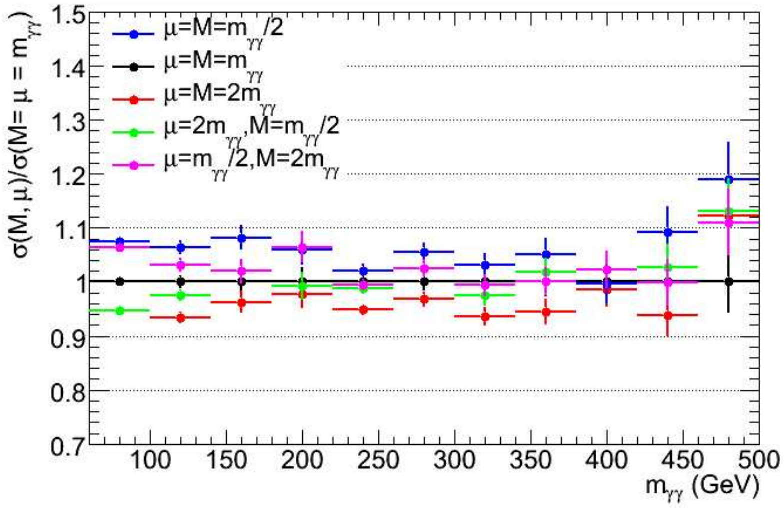

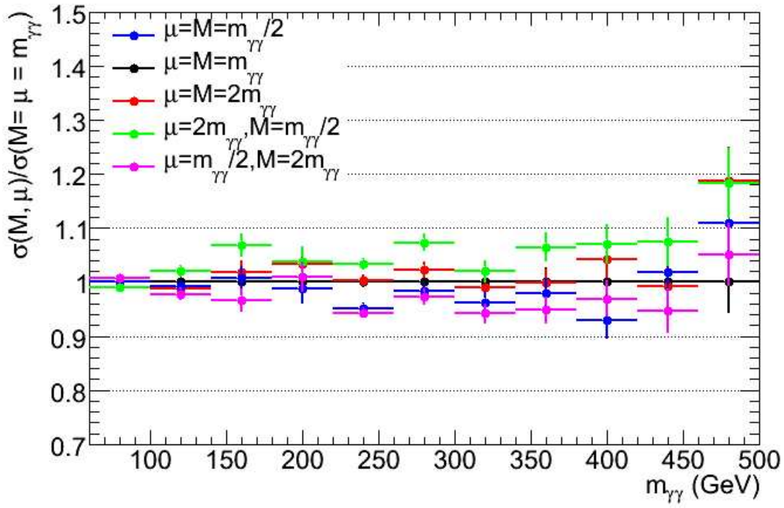

Figure 7.4: Left: ratio of $\gamma\gamma$ invariant mass from difference scale choices to the default one. Right: the same after normalizing the mass spectrum in the control region [60 GeV, 200 GeV].

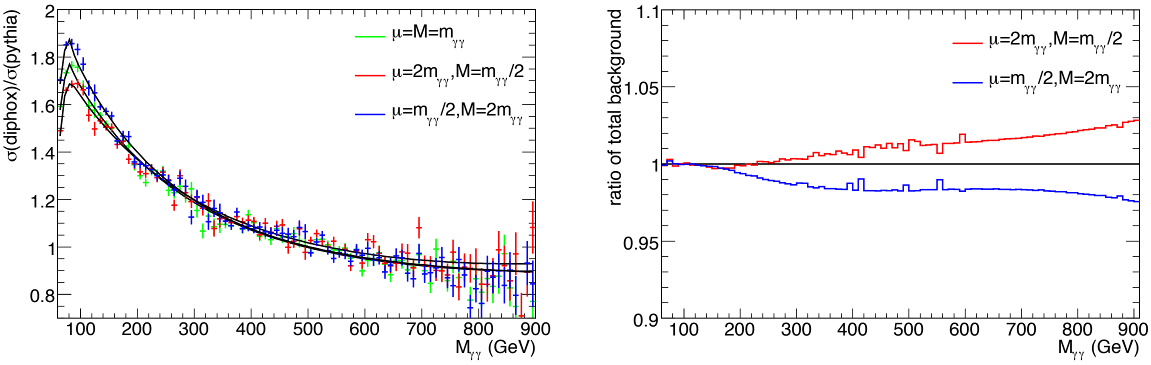

Figure 7.5: Left: DIPHOX/PYTHIA scale factors. Right: Ratio of total expected background from anti diagonal DIPHOX scale choices to that from the default scale choice

.

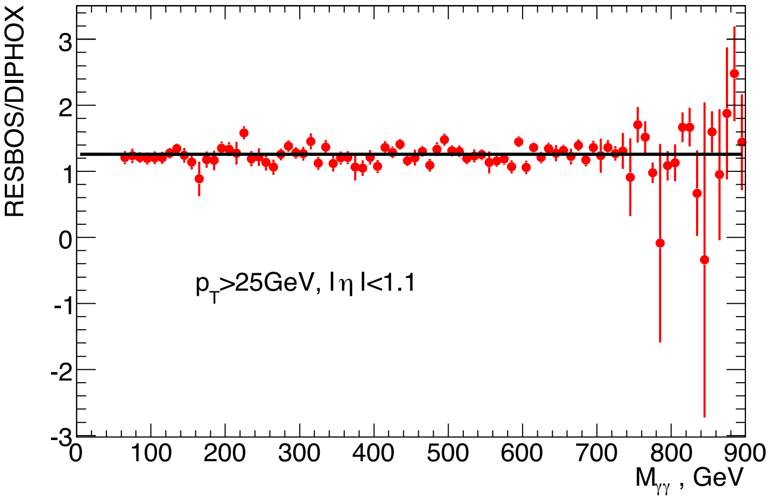

Figure 7.6: Comparison between RESBOS and DIPHOX predictions for the SM $\gamma\gamma$ invariant mass spectrum.

The fraction of probe objects passing the electron ID cuts is measured and compared with the fraction of probe failing the H-matrix cut. Their ratio is shown in Figure 7.7 and 7.8 as functions of p_T, $\eta_{detector}$.

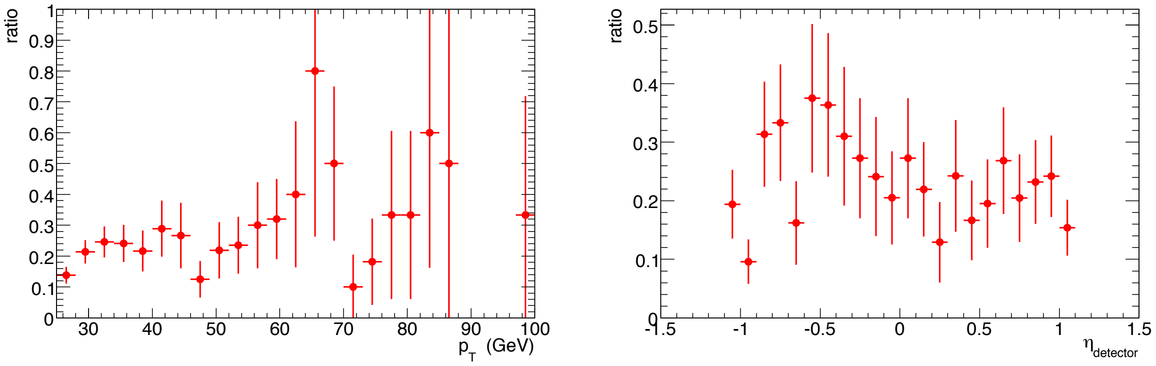

(a) p_T (b) $\eta_{detector}$

Figure 7.7: Ratio between fraction of jet-faked clusters passing electron ID cuts and that of failing H-matrix cut from p17 data.

For Category II, the instrumental backgrounds include multijet and γ+jet processes. We select background samples by reversing the NN5 cut, requiring that both EM objects satisfy iso< 0.07, emfrac> 0.97, isotrk< 2 GeV, and that at least one of them has NN5< 0.1.

Reversing the neural net cut introduces some $\eta_{detector}$ dependence. We estimated the ratio between fraction of jet-faked cluster passing photon ID cuts and that of failing $NN5$ cut, as shown in Figures 7.9 and 7.10.

7.3 Normalization of the Backgrounds

In order to determine the normalization of the various background contributions, we fit the measured diEM invariant mass spectrum in the control region [60 GeV, 200 GeV], where no new physics is expected, with a superposition of the physics background

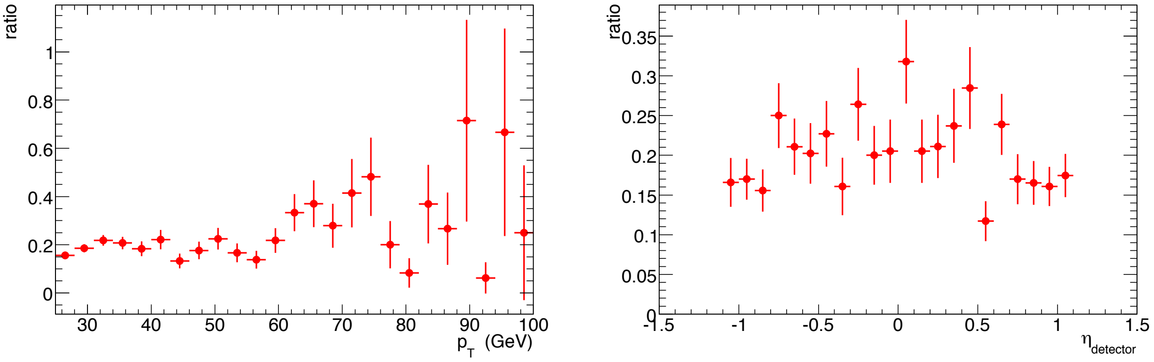

(a) p_T

(b) $\eta_{detector}$

Figure 7.8: Ratio between fraction of jet-faked clusters passing electron ID cuts and that of failing H-matrix cut from p20 data.

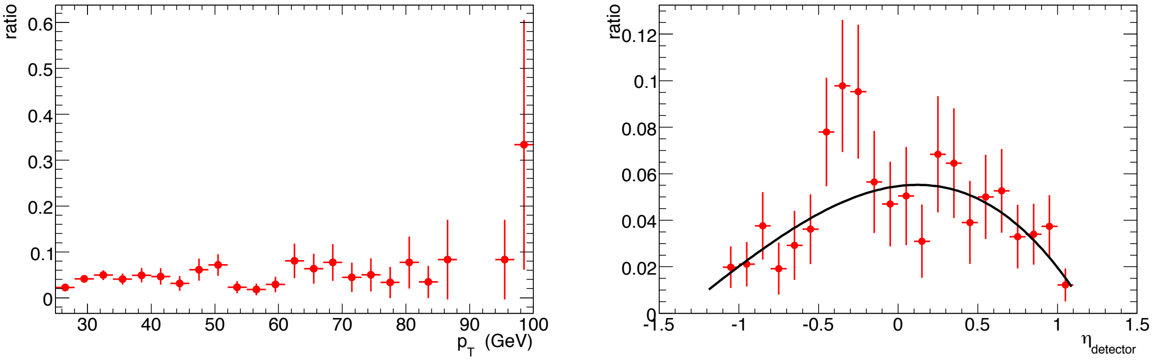

(a) p_T

(b) $\eta_{detector}$

Figure 7.9: Ratio between fraction of jet-faked cluster passing electron ID cuts and that of failing $NN5$ cut from p17 data. The $\eta_{detector}$ dependence is parametrized as $p_0 + p_1x + p_2x^2 + p_3x^3$ where $p_0 = 0.054684$, $p_1 = 0.008785$, $p_2 = -0.034761$ and $p_3 = -0.008998$.

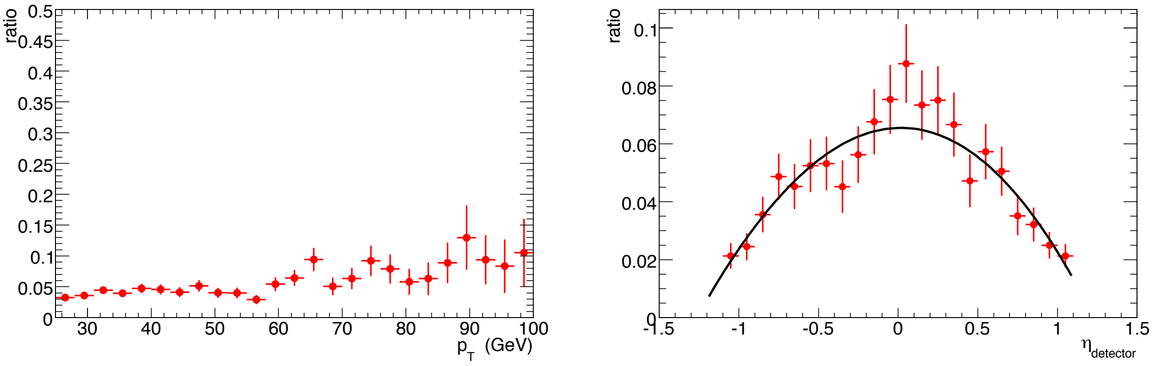

(a) p_T (b) $\eta_{detector}$

Figure 7.10: Ratio between fraction of jet-faked cluster passing photon ID cuts and that of failing $NN5$ cut from p20 data. The $\eta_{detector}$ dependence is parameterized as $p_0 + p_1 x + p_2 x^2 + p_3 x^3$ where $p_0 = 0.065495$, $p_1 = 0.001582$, $p_2 = -0.042321$ and $p_3 = -0.002050$.

shapes and the instrumental background shape. In the control region, the total data should be well described by a weighted sum of the total backgrounds. In addition to DY and $\gamma\gamma$ physics backgrounds, there should be small contributions from some other SM processes including $Z \to \tau\tau$, $W\gamma$, WW, WZ, $t\bar{t}$ and $W + jets$. Given their small size, these backgrounds are fixed to the shape determined by PYTHIA MC, with their normalization fixed according to their NLO production cross sections or the measured value shown in Table 5.8.

The invariant mass spectrum of the data in the control region is fit with a functional form

$$h_{bkg} = f_1 \times h_{DYee} + f_2 \times h_{\gamma\gamma} + (1 - f_1 - f_2) \times h_{inst} + \text{other SM bkgnd}, \qquad (7.2)$$

where h_{DYee}, $h_{\gamma\gamma}$ and h_{inst} are the shapes of the invariant mass spectra normalized to the data from the irreducible DY and $\gamma\gamma$ backgrounds and the instrumental background, respectively. The parameters f_1 and f_2 are varied to minimize the Pearson's

χ^2 test between h_{bkg} and the invariant mass spectrum from the data, h_{data}. The minimization is performed with Root using TMinuit. The fitting process is done on p17 and p20 datasets separately. The results shown below are the combined results of p17 and p20, where the combination is achieved by bin-by-bin additions of the separate results. The p17 and p20 plots and fits can be seen separately in Appendix B.

For Category I, the SM $\gamma\gamma$ contribution is small and difficult to distinguish from the instrumental background. Instead, its normalization is determined from the normalization as determined from the corresponding fit to Category II, described below. After fixing in this way the small SM $\gamma\gamma$ contribution to Category I, the fit to the Category I data in the control region is used to determine the DY and instrumental background normalizations. The results of the fit are shown in Table 7.1 and Figure 7.11. In p17 the fitting $Chi2/ndof$ is 99/70 and in p20 it is 126/70. As can be seen from the table, the DY background contributes over 98% of the total events in the control region for Category I, with most the remainder coming from the instrumental background, and only very small contributions from SM $\gamma\gamma$ and the other SM backgrounds.

For Category II events, the fit procedure is used to determine the normalizations of the contributions of the DY e^+e^- , SM $\gamma\gamma$ and instrumental backgrounds. The results of the fit are shown in Table 7.1 and Figure 7.12. In p17 the fitting $Chi2/ndof$ is 62/70 and in p20 it is 72/70. As can be seen from the table, the control region for Category II includes significant contributions from instrumental background (39.6%), SM $\gamma\gamma$ (36.0%), and DY (22.8%), with the remaining 1.6% arising from the other, small SM backgrounds. Table 7.1 also demonstrates that Category II has far fewer events that Category I, since Category I is dominated by the large background from the DY process. Given the much smaller background, plus the fact that the graviton branching to diphotons is twice that to dielectrons, the Category II sample has a much better search sensitivity than that of Category I. This fact is the primary motivation for splitting the sample into the two categories. As shown in Figure 7.13, this strategy

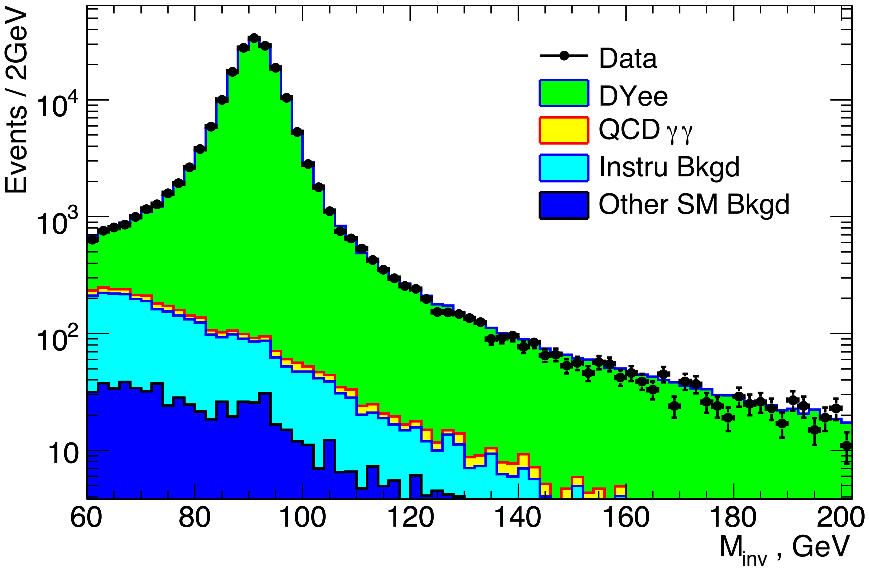

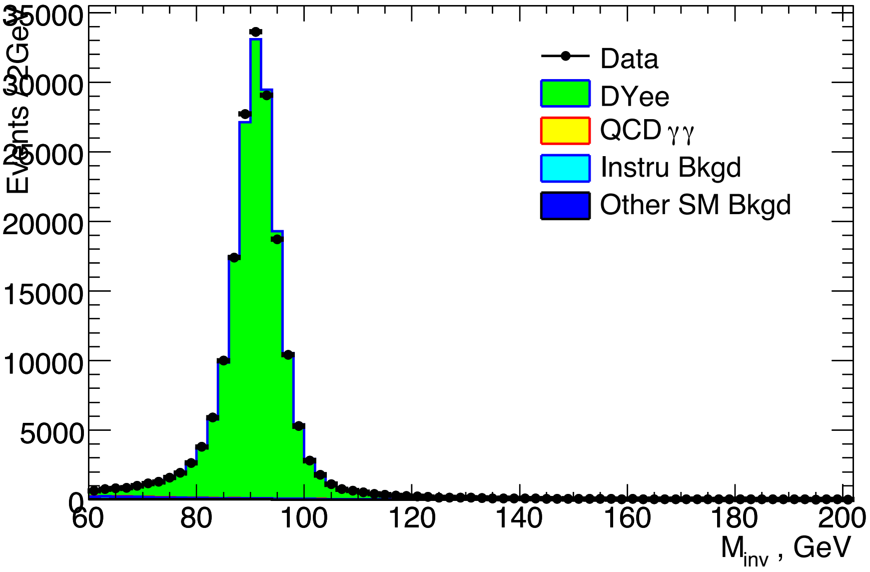

Figure 7.11: Results of the fit of the backgrounds to the data in the control region for Category I, on a log scale (upper plot) and a linear scale (lower plot).

Table 7.1: Number of events in the data in the low-mass control region and the fitted normalization of the various backgrounds for both Category I and Category II.

Control Region	Data	DY e^+e^-	SM $\gamma\gamma$	Instru Bkgd	Other SM Bkgd
Category I	186080	182590.6	356.6	2457.6	675.2
Category II	16703	3809.0	6003.9	6620.2	269.9

improves the expected limit compared to the previous search by a factor of 1.5-2.

7.4 Systematic Uncertainties

The different sources of systematic uncertainties are summarized in Table 7.2. The uncertainties in the integrated luminosity (6.1%) and for EM ID (3% per EM object) are taken as the standard DØ values.

The parton distribution function (pdf) uncertainty is calculated using the pdf reweight procedures as described in [61], where a central pdf set CTEQ6.1M [62] and 2 × 20 sets of error pdfs are provided. The CAF processor caf_pdfreweight is used to study the pdf systematic uncertainties for Gravitons decaying to diEM objects, which calculates an event weight for each pdf set relative to the leading order pdf set CTEQ6L [63]. If B is the central value for CTEQ6.1M and B_i is the value for the error pdf, then if $(B_i - B) > 0$, the difference is called "positive". The quadratic sum of all the "positive" differences yields the "positive" uncertainty. The "negative" uncertainty is calculated similarly. The larger of the two uncertainties is quoted as the symmetric systematic uncertainty. Table 7.3 lists the pdf uncertainties of the acceptance and cross section for p17 and p20 samples.

As described in Section 7.1, the predictions from DIPHOX, with different assumptions for the various relevant scales, are used to set systematic uncertainties on the shape of the SM diphoton invariant mass spectrum.

To investigate the stability of the background estimation, we vary the background

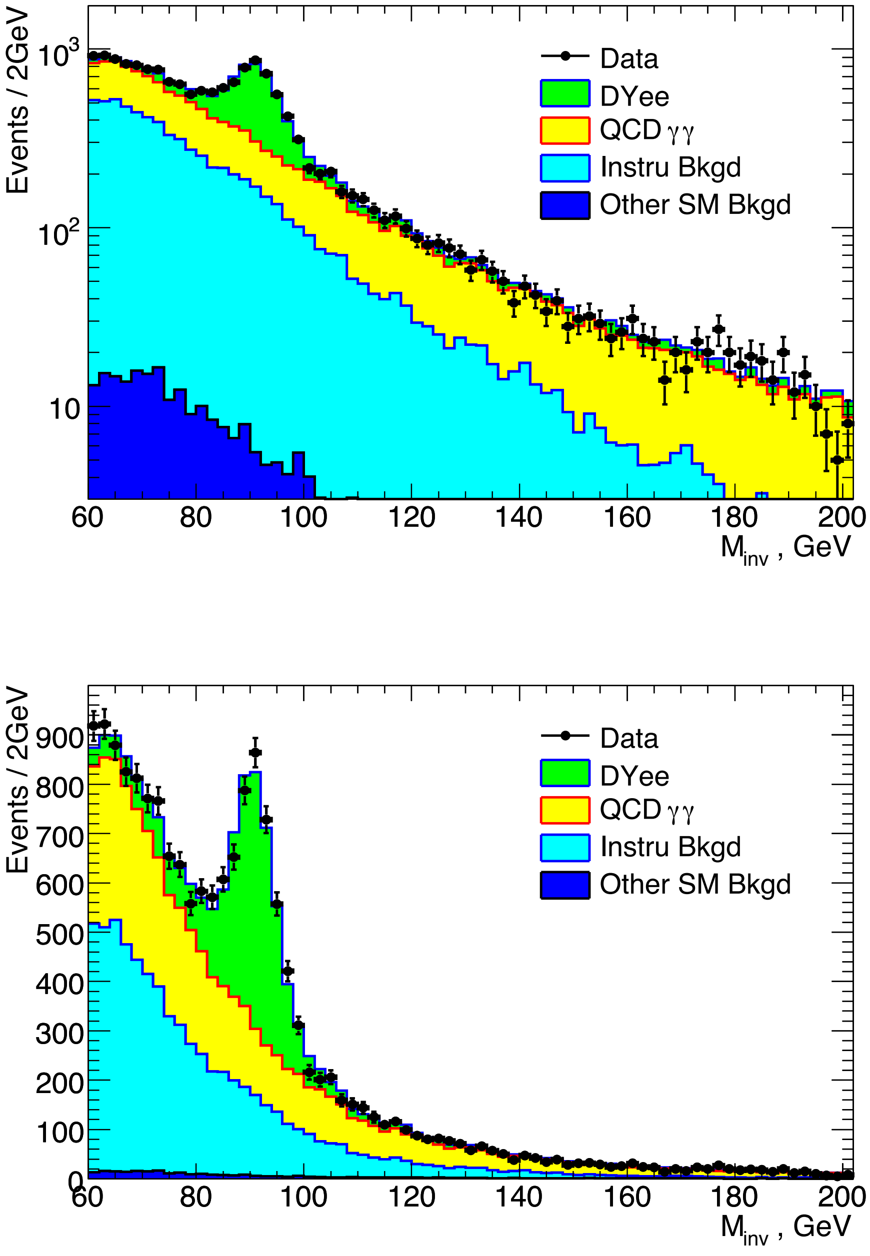

Figure 7.12: Results of the fit of the backgrounds to the data in the control region for Category II, on a log scale (upper plot) and a linear scale (lower plot).

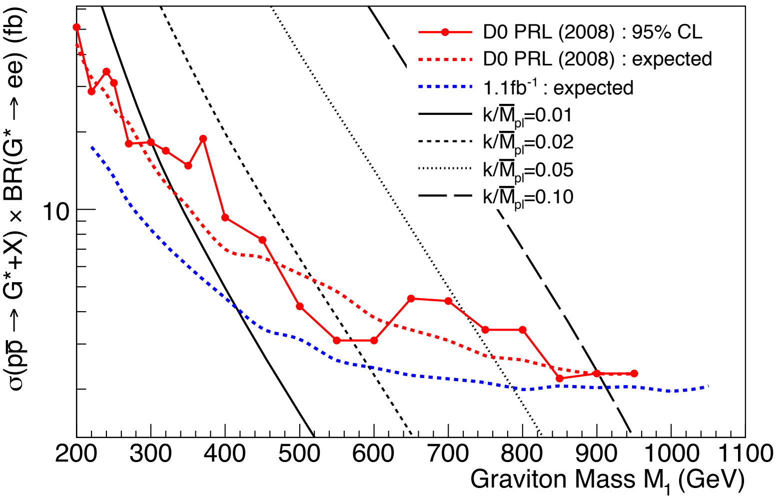

Figure 7.13: 95% CL upper limit on $\sigma \cdot BR(p\bar{p} \rightarrow G \rightarrow e^+e^-)$ and $k/\overline{M}_{Pl}$ versus graviton mass from 1.1 fb^{-1} of data. The limits are shown separately for the previous published results and that from the strategy used in this analysis.

Table 7.2: Sources of systematic uncertainties for signal and expected background

Uncertainties of signal	
Luminosity	6.1%
Acceptance uncertainty from pdf	0.7% – 6.6%
Cross section uncertainty from pdf	9.2% – 16.9%
EM ID uncertainty	3.0%
Energy resolution	6.0%
Trigger	0.1%
Uncertainties of expected background	
EM ID uncertainty	3.0%
DY e^+e^- k-factor	5.0%
SM $\gamma\gamma$ mass spectrum shape	shapes
Background normalization	2% (Category I) and 10% (Category II)

Table 7.3: Uncertainty of signal acceptance and cross section due to pdf's for the various graviton mass points

Graviton		Acceptance Uncertainty (%)				Cross Section Uncertainty (%)			
Mass (GeV)	Coupling	e^+e^- channel		$\gamma\gamma$ channel		e^+e^- channel		$\gamma\gamma$ channel	
		p17	p20	p17	p20	p17	p20	p17	p20
220	0.01	3.7	4.0	5.8	6.1	11.9	12.5	11.7	11.7
250	0.01	3.0	2.8	6.6	6.6	12.5	12.3	12.8	12.7
270	0.01	2.2	2.6	6.9	6.6	12.3	12.8	13.0	12.9
300	0.01	2.3	1.7	6.4	6.0	13.0	12.4	12.8	12.3
350	0.01	1.3	1.1	6.3	6.1	12.7	12.3	12.9	12.4
400	0.01	1.2	1.1	5.5	6.2	12.5	11.4	11.4	12.5
450	0.01	1.3	1.3	5.3	5.5	11.5	11.3	11.4	11.4
500	0.02	1.1	1.2	5.7	5.1	10.9	10.5	12.0	10.9
550	0.02	1.2	1.1	4.8	3.8	10.5	10.6	10.7	9.9
600	0.02	1.6	1.6	3.9	3.8	9.8	10.1	9.8	9.7
650	0.02	1.4	1.7	3.8	3.2	10.8	9.5	9.9	9.2
700	0.02	1.6	2.0	3.9	3.0	10.8	10.5	10.0	9.9
750	0.03	1.4	1.5	2.6	3.2	11.1	10.8	10.8	10.7
800	0.03	0.7	2.4	2.8	3.4	11.6	11.6	11.5	11.6
850	0.05	1.9	1.9	2.2	2.7	12.4	12.6	12.6	12.5
900	0.05	1.7	1.5	2.4	2.2	13.5	13.5	13.6	13.6
950	0.07	2.2	2.4	4.0	2.7	14.6	14.5	14.5	14.6
1000	0.10	1.7	1.4	2.4	2.9	15.6	15.6	15.7	15.5
1050	0.10	2.2	1.5	2.4	1.5	16.9	16.9	16.9	16.9

templates in different ways, redo the background fitting as described previously, and take the resultant variations in the extrapolated background as systematic uncertainties.

For Category I, we varied the background templates and fitting process in the following ways:

- use HMx7 > 30 (instead of > 25) to estimate the instrumental background
- loosen iso and $emfrac$ cut to $iso < 0.15$ and $emfrac > 0.95$
- add in events with only one EM object failing HMx7 cut
- change the upper fitting range from 200 GeV down to 180 GeV
- change the W+jet contribution by a factor of 2 and 1/2
- change the $\gamma\gamma$ contribution by a factor of 2 and 1/2

The fitting $\chi^2/ndof$ fluctuates between 99.5/70 and 107.2/70 in p17 or between 124.0/70 and 152.0/70 in p20, and the total background fluctuation relative to the one used is shown in Figure 7.14. The fit parameters have a statistical uncertainty of 0.2%. We assign a 2% of systematic error to cover all these variations.

For Category II, we try the following variations:

- use NN5 < 0.05 to estimate the instrumental background
- loosen iso, $emfrac$ and $isotrk$ cuts as $iso < 0.15$, $emfrac > 0.95$ and $isotrk <$ 5 GeV
- use events with both EM objects failing $NN5$ cut
- change the upper fitting range from 200 GeV down to 180 GeV

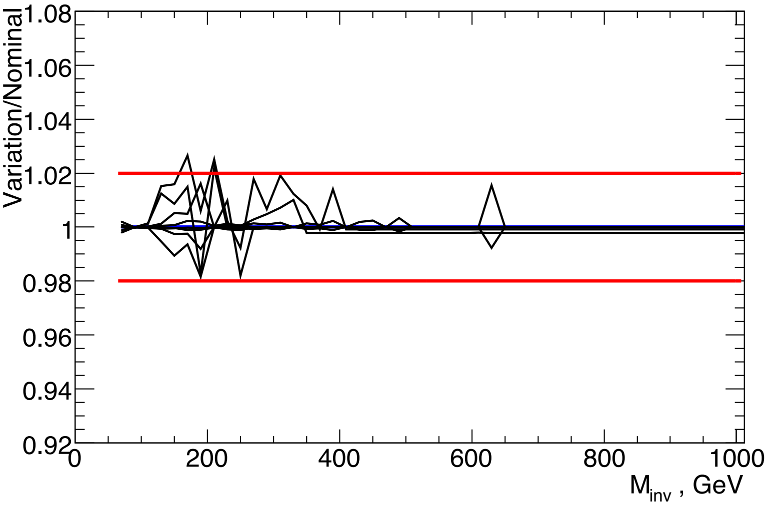

(a) p17

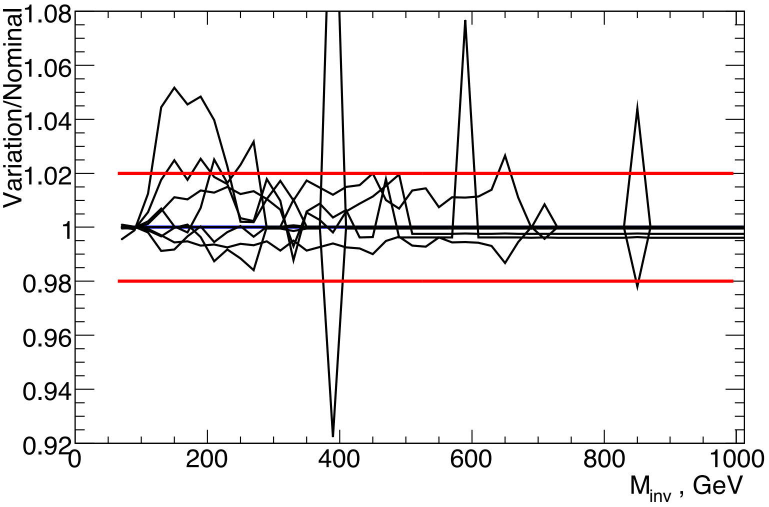

(b) p20

Figure 7.14: Variation of background estimate in Category I p17 and p20. For more details, see the text.

The fitting $\chi^2/ndof$ fluctuates between 58.6/70 and 70.5/70 in p17 or between 71.0/70 and 81.6/70 in p20, and the total background fluctuation relative to the one used is shown in Figure 7.15. The uncertainties on the fit parameters are also shown on this plot, and are able to cover these variations.

For the EM calorimeter, the electron or photon energy resolution can be modeled with three parameters:

$$\frac{\sigma_{EM}(E)}{E} = C_{EM} \oplus \frac{S_{EM}}{\sqrt{E}} \oplus \frac{N_{EM}}{E} \tag{7.3}$$

where C_{EM} is the constant term, N_{EM} is the noise term, and S_{EM} is the sampling term. For high energy EM particles, the influence of the constant term is dominant. The value of the constant term has been measured with two different methods [64], giving the results $2.06 \pm 0.12\%$ and $2.04 \pm 0.13\%$, implying a relative uncertainty on the constant term of about 6%. To take this into account, two Gaussian weighting functions are used with larger (oversmearing) and smaller (undersmearing) widths, which are applied to each event to simulate the impact of these oversmearing and undersmearing effects on the signal reconstruction.

Among the systematic uncertainties, those due to the energy resolution, SM $\gamma\gamma$ mass shape variation, and the fit error in Category I and Category II are implemented in the limit calculation with $\pm 1\sigma$ shapes. The lower edge of the signal theoretical cross section band is taken as a conservative approach. Other uncertainties are treated as a constant throughout the whole mass spectrum.

As will be shown later, for large graviton masses the search is strongly limited by statistics, and the systematic errors have little impact on the expected sensitivity.

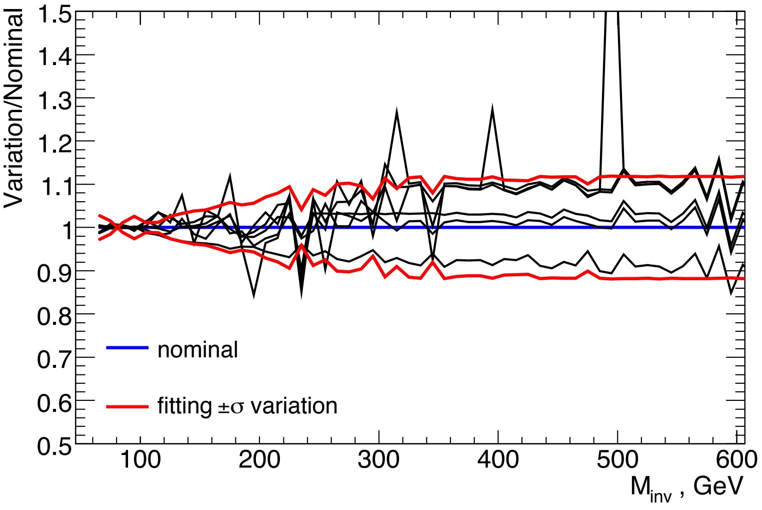

(a) p17

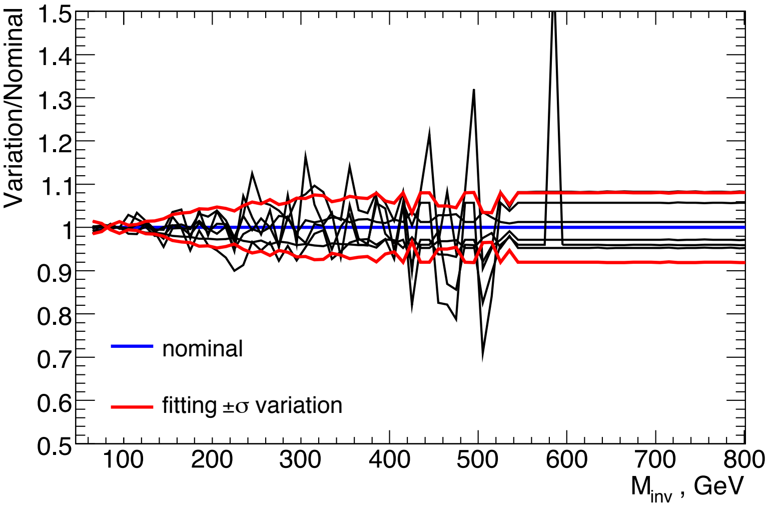

(b) p20

Figure 7.15: Variation of background estimate in Category II p17 and p20. For more details, see the text.

Chapter 8

Results

Having normalized the various background contributions to data in the low-mass control region, we extrapolate those normalized background shapes to the high-mass signal search region. Figure 8.1 shows the invariant mass spectra of Category I and Category II events for the entire mass range, including the data as well as the extrapolated background predictions.

No significant excess in seen in the data of Figure 8.1 above the expected background levels. This visual impression is confirmed by examining the number of data and expected background events in various mass windows (see Table 8.1) or integrated above various mass values (see Table 8.2).

In the absence of a signal of a heavy narrow resonance, an upper limit can be

Table 8.1: Number of data and background events for various mass windows for Category I and Category II in signal search region.

Mass Window (GeV)		(200,300)	(300,400)	(400,500)	(500,600)	(600, -)
Cat. I	Data	391	90	23	9	3
	Bkgnd	419.5±33.9	89.7±7.2	24.6±2.0	7.8±0.6	3.6±0.3
Cat. II	Data	212	55	16	2	2
	Bkgnd	238.0±29.8	48.3±6.0	14.1±1.8	4.4±0.6	1.9±0.2

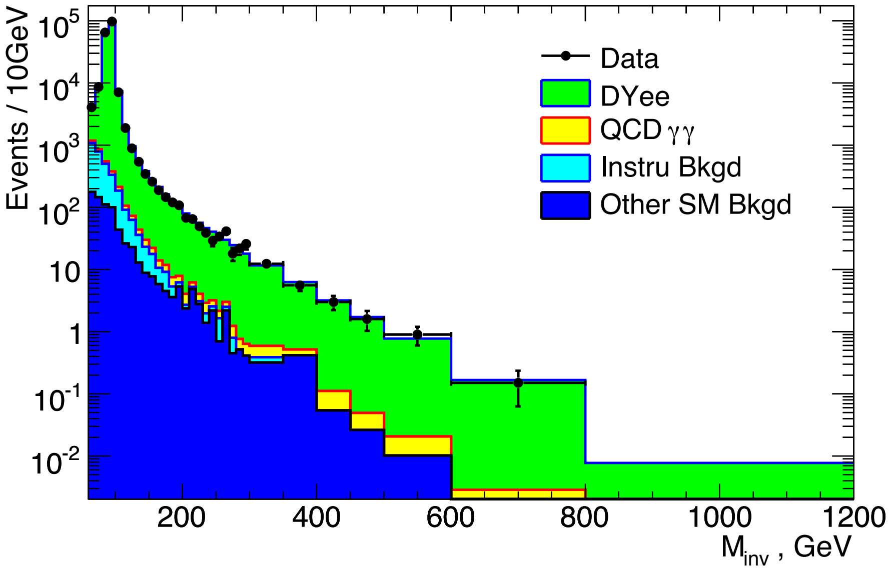

(a) Category I

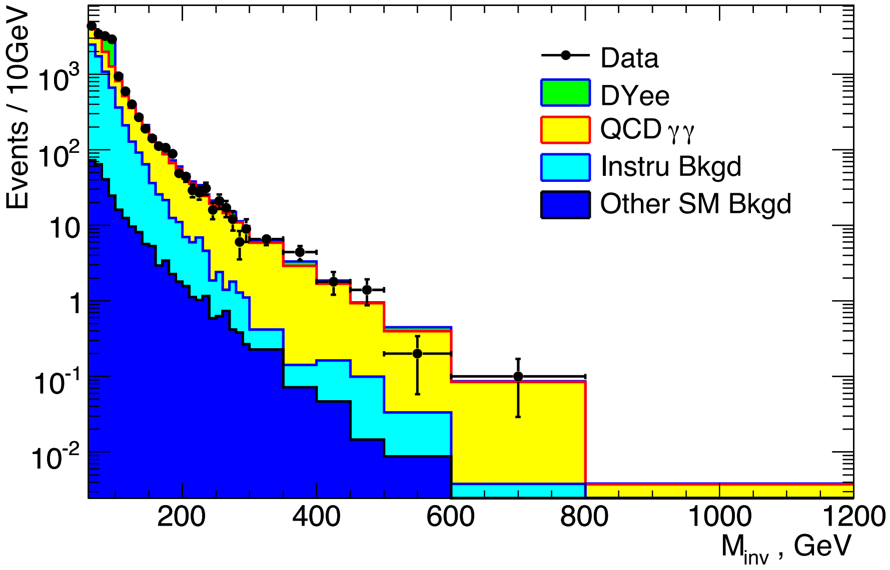

(b) Category II

Figure 8.1: Invariant mass spectrum for data (points) and expected total background (open line histogram) in Category I and Category II.

Table 8.2: Number of data and background events, integrated above various mass values, for Category I and Category II.

Mass Window(GeV)		(200,-)	(300,-)	(400,-)	(500,-)	(600,-)
Cat. I	Data	516	125	35	12	3
	Bkgnd	545.2±44.0	125.7±10.1	36.0±2.9	11.4±0.9	3.6±0.3
Cat. II	Data	287	75	20	4	2
	Bkgnd	306.7±38.4	68.7±8.6	20.4±2.6	6.3±0.8	1.9±0.2

set on the value of $\sigma \cdot BR(p\bar{p} \rightarrow G^{*} \rightarrow e^{+}e^{-})$. The Collie Limit calculator [65] is used to calculate exclusion limits at the 95% CL. Two distinct hypotheses that will be compared to data are described: background-only (NULL) hypothesis and signal-plus-background hypothesis (TEST). Collie adopts a semi-Frequentist construction for the estimation of the likelihood distributions associated with a comparison of the TEST and NULL hypotheses, which is

$$\Gamma = -2\ln(Q) = 2\sum_{i=1}^{Nchannels}\sum_{j=1}^{Nbins}(s_{ij} - d_{ij}\ln(1 + s_{ij}/b_{ij})) \tag{8.1}$$

where s and b are the expected signal and background, and d is the data. Category I and Category II as treated as two independent channels. Systematic uncertainties are incorporated via convolution of the Poisson probability distributions for signal and background with Gaussian distributions corresponding to the different sources of systematic uncertainty. The inputs to Collie are:

- the measured invariant mass spectrum of the data,
- the invariant mass spectrum of the expected background, with proper normalizations,
- the expected invariant mass spectrum for a given graviton signal, and
- the uncertainties on the expected background and graviton signal,

where the histograms are input with a fixed bin width of 2 GeV.

Table 8.3 and Figure 8.2 show the exclusion limits on production of an RS graviton with subsequent decay to dielectrons. These results are the combination of the separate Category I and Category II results, which can be seen separately in Appendix C. For the Randall-Sundrum model with a warped extra dimension, we set 95% CL upper limits on the production cross section times branching ratio into electron-positron pairs of the lightest Kaluza-Klein mode of the graviton between 6.9 fb and 0.43 fb for masses of 220 GeV and 1050 GeV, respectively. These translate into lower limits on the mass M_1 of the lightest Kaluza-Klein mode of the graviton of 440 GeV to 1040 GeV for couplings of the graviton to SM fields $k/\overline{M}_{\mathrm{Pl}} = 0.01$ to 0.1. In addition, for coupling $k/\overline{M}_{\mathrm{Pl}} = 0.01$, 460 GeV $< M_1 <$ 560 GeV is also excluded at 95% CL.

Given the smaller background and larger branching ratio to diphotons, the Category II sample has more sensitivity than that of Category I. Therefore, as mentioned earlier, separating into two categories would be expected to improve the sensitivity. This can be seen in Figure C.1 in Appendix C, where the p17 version of this analysis is compared with the published result with the same dataset. The expected limit improves by a factor of typically 1.5-2 compared with the previous result. Figure C.2, also in Appendix C, shows the separate limits of the current analysis for the two categories, demonstrating the increased sensitivity of Category II as compared to Category I.

Figure C.3 shows the limit for statistical errors only in addition to the full errors including both statistical and systematic errors; the sensitivity is strongly statistics-limited for all but the lowest graviton masses considered. Finally, Figure C.4 shows the limit obtained, and the limit which would have been obtained if calorimeter saturation effects were not considered; given the statistically limited nature of the search for high graviton masses, the impact on the limit of the saturation effects is rather small.

As discussed in Appendix D, we have investigated whether including a decay angu-

Table 8.3: 95% CL expected and observed upper limits on cross section × branching ratio and coupling.

Graviton Mass	Cross Section × BR ($G^* \to e^+e^-$) in fb		Coupling $k/\overline{M}_{\mathrm{Pl}}$	
GeV	expected	observed	expected	observed
220	10.6	6.7	0.0037	0.0029
250	7.2	5.4	0.0041	0.0036
270	5.6	5.7	0.0044	0.0044
300	3.9	5.5	0.0046	0.0054
350	2.6	3.1	0.0054	0.0059
400	2.0	1.4	0.0065	0.0054
450	1.4	3.0	0.0072	0.0105
500	1.1	1.3	0.0085	0.0091
550	0.86	0.87	0.0097	0.0097
600	0.73	0.81	0.011	0.012
650	0.62	0.68	0.014	0.014
700	0.55	0.48	0.017	0.016
750	0.52	0.52	0.021	0.021
800	0.47	0.47	0.026	0.026
850	0.45	0.45	0.034	0.033
900	0.43	0.41	0.043	0.043
950	0.43	0.43	0.058	0.058
1000	0.42	0.43	0.076	0.077
1050	0.42	0.42	0.105	0.104

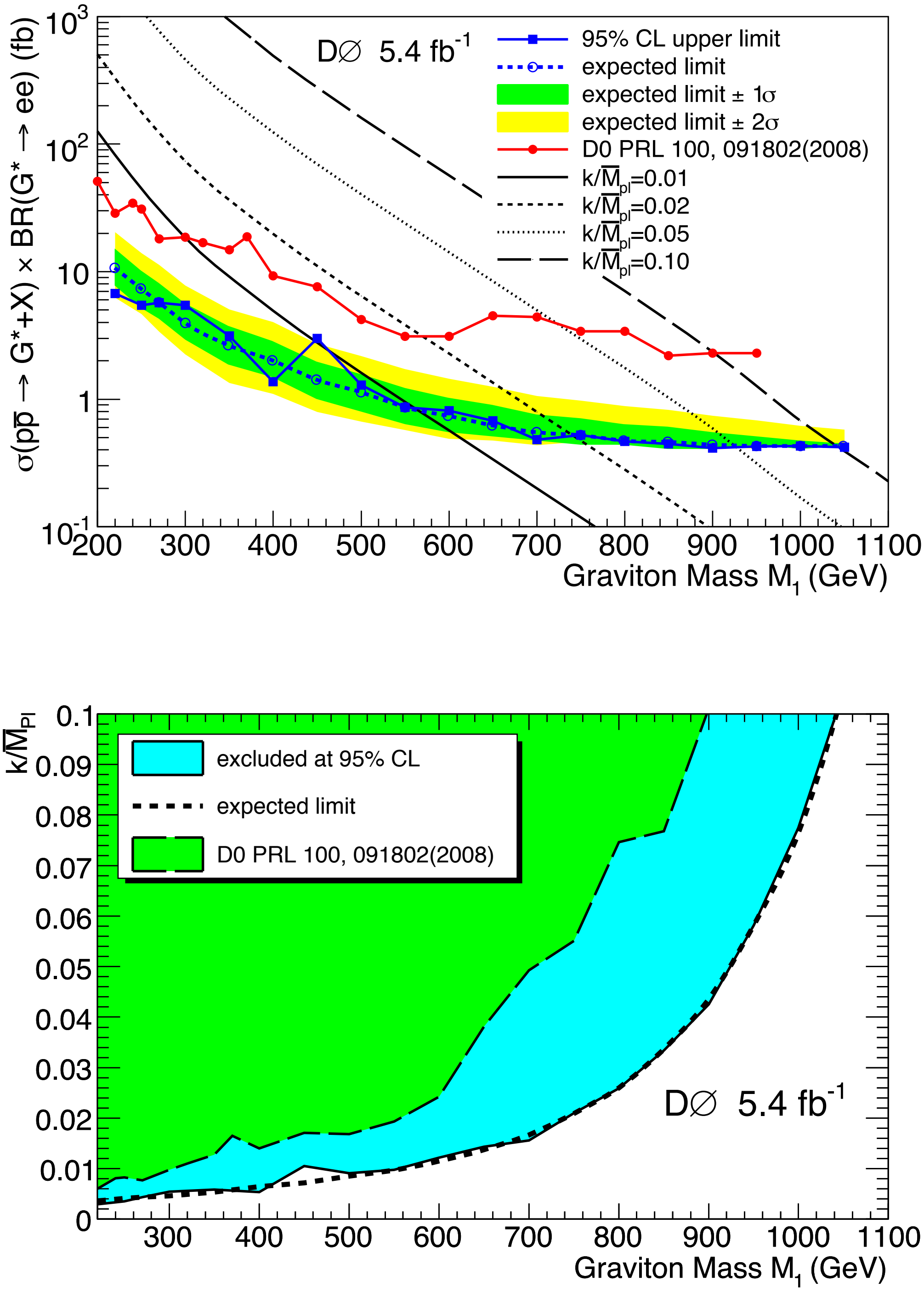

Figure 8.2: 95% CL upper limit on $\sigma \cdot BR(p\bar{p} \rightarrow G^* \rightarrow e^+e^-)$ and $k/\overline{M}_{\rm Pl}$ versus graviton mass from 5.4 fb^{-1} of DØ data compared with the previously published DØ results.

lar analysis can significantly improve the sensitivity of the analysis, given the unique spin-2 nature of the graviton. However, the result is only a very small improvement in sensitivity, so we have not included the complication of the angular analysis in the main result.

Chapter 9

Summary and Conclusions

Using 5.4 fb^{-1} of data from $p\bar{p}$-collisions at $\sqrt{s} = 1.96$ TeV, collected with the DØ detector at the Fermilab Tevatron between July 2002 and June 2009, we have searched for a narrow resonance in the invariant mass spectrum of two electromagnetic showers from electron-positron or photon pairs. The observed spectrum agrees with predictions based on SM background processes. For the Randall-Sundrum model with a warped extra dimension, we set 95% CL upper limits on the production cross section times branching ratio into electron-positron pairs of the lightest Kaluza-Klein mode of the graviton between 6.9 fb and 0.43 fb for masses of 220 GeV and 1050 GeV, respectively. These translate into lower limits on the mass M_1 of the lightest Kaluza-Klein mode of the graviton of 440 GeV to 1040 GeV for couplings of the graviton to SM fields $k/\overline{M}_{\mathrm{Pl}} = 0.01$ to 0.1. In addition, for coupling $k/\overline{M}_{\mathrm{Pl}} = 0.01$, 460 GeV $< M_1 <$ 560 GeV is also excluded at 95% CL. These results represent the most sensitive limits to date.

Looking ahead to the future prospects for possible discovery of Randall-Sundrum gravitons, the DØ experiment continues collecting data. In total by the end of 2011, around 12 fb^{-1} of data is expected. By then, due to the increase of integrated luminosity, the sensitivity would be enhanced. For example, with coupling $k/\overline{M}_{\mathrm{Pl}} =$ 0.01, $M_1 <$600 GeV could be excluded at 95% CL.

Currently, the Large Hadron Collider (LHC) at CERN is being commissioned. First collisions at 900 GeV were recently observed, with operations at 7 TeV anticipated during 2010, and a final energy of 14 TeV to be achieved later. The potential to discover RS graviton was evaluated based on 1 fb^{-1} of data expected at the ATLAS experiment with center of mass energy of 14 TeV. The results are summarized in Figure 9.1. For example, a 900 GeV RS graviton with a coupling of 0.01 could be discovered with 5σ significance if it exists.

With the turn on of the LHC, we expect to continue to make significant inroads in the search for evidence of RS gravitons.

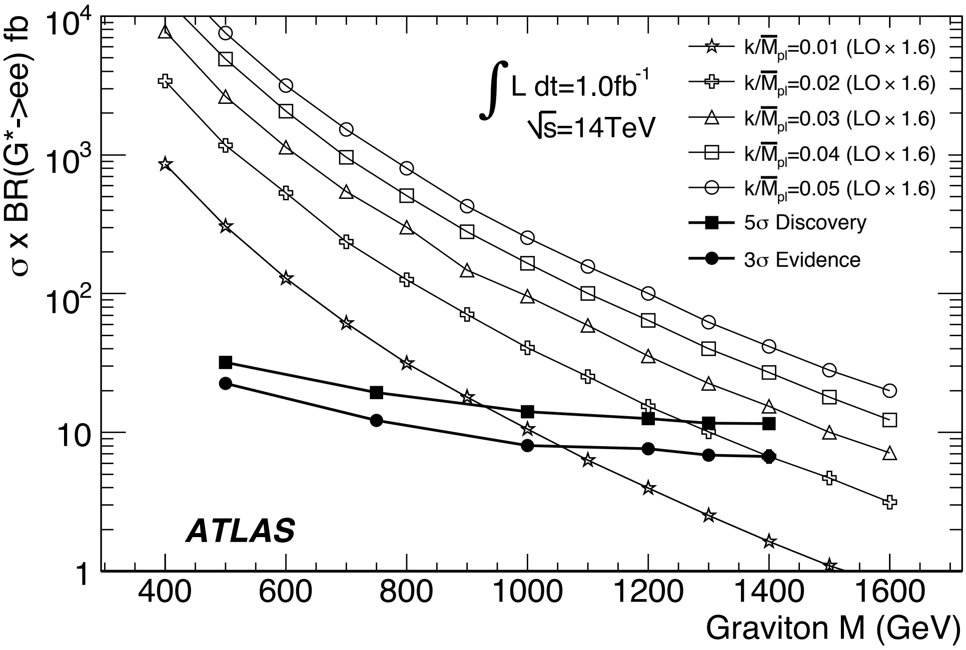

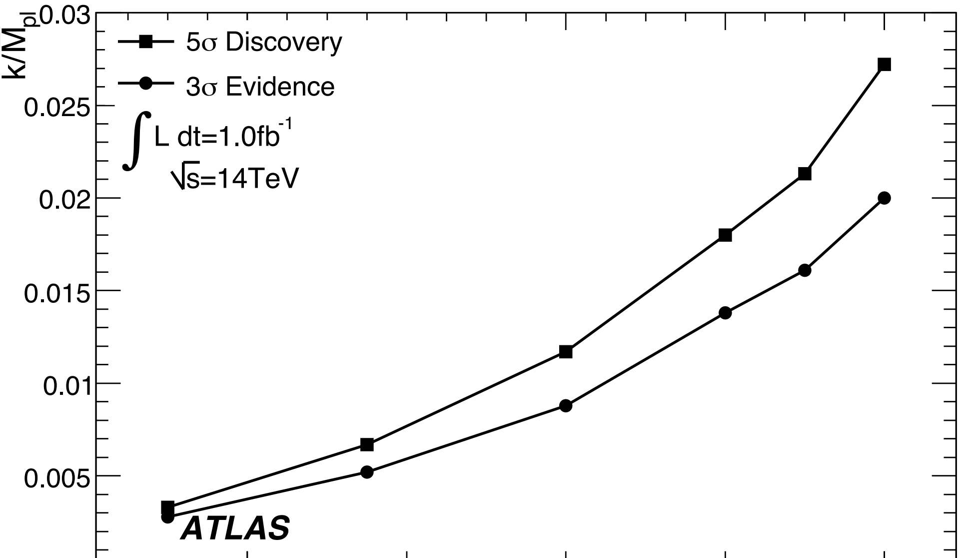

Figure 9.1: 5σ discovery and 3σ evidence potential for $\sigma \cdot BR(p\bar{p} \to G^* \to e^+e^-)$ and $k/\overline{M}_{\rm Pl}$ versus graviton mass expected at the ATLAS experiment with 1 fb^{-1} of data at $\sqrt{s}$=14 TeV.

Bibliography

[1] N. J. Buchanan *et al.* ATLAS liquid argon calorimeter font end electronics. *JINST*, 3:P09003, 2008.

[2] N. J. Buchanan *et al.* Design and implementation of the front end board for the readout of the ATLAS liquid argon calorimeters. *JINST*, 3:P03004, 2008.

[3] G. Aad *et al.* The ATLAS experiment at the CERN Large Hadron Collider. *JINST*, 3:S08003, 2008.

[4] F. M. L. Almeida Jr. *et al.* Dilepton resonances at high mass. ATL-PHYS-PUB-2009-070, ATL-COM-PHYS-2009-093.

[5] M. Aharrouche *et al.* Physics performance studies and strategy of the electron and photon trigger selection. ATL-PHYS-PUB-2009-029, ATL-COM-PHYS-2009-122.

[6] M. Aharrouche *et al.* The trigger for early running. ATL-PHYS-PUB-2009-025, ATL-COM-PHYS-2009-124.

[7] G. Aad *et al.* Expected performance of the ATLAS experiment - detector, trigger and physics. CERN-OPEN-2008-020.

[8] J. Parsons and N. Zhou. Search for Randall-Sundrum gravitons in dielectron and diphoton final states with 5.4 fb^{-1} of data. DØ Note 6012.

[9] D. Bandurin *et al.* Photon identification for Run II data. DØ Note 6004.

[10] S. Weinberg. A model of leptons. *Phys. Rev. Lett.*, 19:1264, 1967.

[11] A. Salam. *Elementary Particle Theory.* Almquist and Wiksells, Stockholm, 1968.

[12] S. L. Glashow, J. Iliopoulos, and L. Maiani. Weak interactions with lepton-hadron symmetry. *Phys. Rev. D.*, 2:1285, 1970.

[13] R. K. Ellis et al. *QCD and Collider Physics.* Cambridge, 1996.

[14] Y. Fukuda et al. Evidence for oscillation of atmospheric neutrinos. *Phys. Rev. Lett.*, 81:1562, 1998.

[15] Q. R. Ahmad et al. Direct evidence for neutrino flavor transformation from neutral-current interactions in the Sudbury Neutrino Observatory. *Phys. Rev. Lett.*, 89:011301, 2002.

[16] C. Amsler et al. Review of particle physics 2008. *Phys. Lett. B.*, 667:1, 2008.

[17] L. Randall and R. Sundrum. Large mass hierarchy from a small extra dimension. *Phys. Rev. Lett.*, 83:3370, 1999.

[18] W. D. Goldberger and M. B. Wise. Modulus stabilization with bulk fields. *Phys. Rev. Lett.*, 83:4922, 1999.

[19] H. Davoudiasl, J. L. Hewett, and T. G. Rizzo. Phenomenology of the Randall-Sundrum gauge hierarchy model. *Phys. Rev. Lett.*, 84:2080, 2000.

[20] Th. Kaluza. *Sitzungsber. Preuss. Akad. Wiss. Math. Phys*, page 966, 1921.

[21] O. Klein. *Z. Phys*, 37:895, 1926.

[22] T. Sjöstrand et al. High-energy-physics event generation with PYTHIA 6.1. *Compu. Phys. Commun.*, 135:238, 2001.

[23] H. Davoudiasl, J. L. Hewett, and T. G. Rizzo. Experimental probes of localized gravity: on and off the wall. *Phys. Rev. D.*, 63:075004, 2001.

[24] B. C. Allanach et al. Exploring small extra dimensions at the Large Hadron Collider. *JHEP*, 12:039, 2002.

[25] V. M. Abazov et al. Search for Randall-Sundrum gravitons with 1 fb^{-1} of data from $p\bar{p}$ collisions at $\sqrt{s} = 1.96$tev. *Phys. Rev. Lett.*, 100:091802, 2008.

[26] T. Aaltonen et al. Search for high-mass e^+e^- resonances in $p\bar{p}$ collisions at $\sqrt{s} = 1.96$ tev. *Phys. Rev. Lett.*, 102:031801, 2009.

[27] T. Aaltonen et al. Search for high-mass diphoton states and limits on Randall-Sundrum gravitons at CDF. *Phys. Rev. Lett.*, 99:171801, 2007.

[28] Frank T. Cole, (Ed.), Edwin L. Goldwasser, (Ed.), and Robert Rathbun Wilson, (Ed.). National Accelerator Laboratory design report january 1968. FERMILAB-DESIGN-1968-01.

[29] TeVI Group. Design report Tevatron 1 project. FERMILAB-DESIGN-1984-01.

[30] Pushpalatha C. Bhat and William J. Spalding. Fermilab collider Run II: accelerator status and upgrades. *AIP Conf. Proc.*, 753:30, 2005.

[31] S. Abachi et al. The DØ detector. *Nucl. Inst. Methods A*, 338:185, 1994.

[32] S. Abachi et al. The DØ upgrade: the detector and its physics. *Fermilab Technical Report*, 1996. FERMILAB-PUB-96/357-E.

[33] V. M. Abazov et al. The upgraded DØ detector. *Nucl. Inst. Methods A*, 565:463, 2006.

[34] DØ Upgrade Collaboration. DØ silicon tracker technical design report. Available online at: http://d0server1.fnal.gov/ projects/ silicon/ www/ silicon_old.html.

[35] Michael S. Weber. The DØ silicon micro-strip tracker. *Nucl. Inst. Methods A*, 560:14, 2006.

[36] DØ Upgrade Collaboration. The DØ upgraded central fiber tracker technical design report. Available online at: http://d0server1.fnal.gov/ projects/ scifi/ cft_home.html.

[37] M. Adams et al. Design report of the central preshower detector for the DØ upgrade. 1996. DØ Note 3014.

[38] M. Bhattachargee et al. Technical design report of the forward preshower detector for the DØ upgrade. 1998. DØ Note 3445.

[39] G. Bernardi et al. Improvements from the T42 algorithm on calorimeter objects reconstruction. 2004. DØ Note 4335.

[40] U. Bassler. Online calorimeter calibration procedures and database design. 2007. DØ Note 5316.

[41] DØ Algorithms Group. How to run RECO. Available online at: http://www-d0.fnal.gov/ computing/ algorithms/ howto/ howtoreco.html.

[42] DØ Algorithms Group. DØ Run II event data model. Available online at: http://www-d0.fnal.gov/ software/ data_model/ data_model.html.

[43] G. Borissov. Ordering a chaos or ... technical detail of AA tracking. Available online at: http://www-d0.fnal.gov/ global_tracking/ talks/ 20030228/ talk-adm-030228.ps.

[44] A. Khanov. HTF: histogramming method for finding tracks. the algorithm description. 2000. DØ Note 3778.

[45] A. Schwartzman et al. Primary vertex reconstruction by means of adaptive vertex fitting. 2005. DØ Note 4918.

[46] M. Narain et al. Probabilistic primary vertex selection. 2002. DØ Note 4042.

[47] F. Fleuret. The DØ electron/photon analysis package emanalyze. 2001. DØ Note 3888.

[48] Common Samples Group. http://www-d0.fnal.gov/ Run2Physics/ cs/.

[49] DØ Data Quality Group. http://www-d0.fnal.gov/ computing/ data_quality/ d0_private/ forusers.html.

[50] L. Han et al. Measurement of the forward-backward charge asymmetry in $z/\gamma^* + z \rightarrow e^+e^- + x$ events produced at $\sqrt{s} = 1.96$ tev. 2008. DØ Note 5603.

[51] X. Bu et al. Search for the standard model higgs boson in $\gamma\gamma$ final states at DØ with 4.2 fb^{-1} data. 2009. DØ Note 5846.

[52] A. Schwartzman et al. Probabilistic primary vertex selection. 2002. DØ Note 4042.

[53] D. Bandurin et al. Photon identification for RunII data. 2009. DØ Note 6004.

[54] P. Mathews et al. NLO-QCD corrections to dilepton production in the Randall-Sundrum model. *JHEP*, 0510:031, 2005.

[55] R. Zitoun. Study of the non linearity of the DØ calorimeter readout chain. 2002. DØ Note 3997.

[56] U. Bassler. Calorimeter calibration: online calibration procedures and online/offline database design. 2007. DØ Note 5316.

[57] T. Nunnemann. NNLO cross-sections for Drell-Yan, Z and W production using modern parton distribution functions. 2004. DØ Note 4476.

[58] M. Shamim et al. Generator level reweighting of Z boson p_t. 2008. DØ Note 5565.

[59] T. Binoth et al. A full next-to-leading order study of direct photon pair production in hadronic collisions. *Eur. Phys. J. C.*, 16:311, 2000.

[60] C. Balázs, E. L. Berger, P. M. Nadolsky, and C. P. Yuan. Calculation of prompt diphoton production cross sections at Tevatron and LHC energies. *Phys. Rev. D.*, 76:013009, 2007.

[61] V. Buescher et al. Conclusions of mini-workshop on PDF uncertainties and related topics. 2004. DØ Note 4618.

[62] D. Stump et al. Inclusive jet production, parton distributions, and the search for new physics. *JHEP*, 0310:046, 2003.

[63] J. Pumplin et al. New generation of parton distributions with uncertainties from global QCD analysis. *JHEP*, 07:012, 2002.

[64] A. Melnitchouk. Determination of the constant term of the electron resolution. 2009. DØ Note 5879.

[65] W. Fisher. Collie: a confidence level limit evaluator. 2009. DØ Note 5595.

Appendix A

Test of Two-Dimensional Reweighting to DIPHOX Events

In the analysis, the PYTHIA SM $\gamma\gamma$ events are reweighted to reproduce the diphoton invariant mass spectrum as predicted by DIPHOX. However, after this reweighting, there still exist differences in other variables between PYTHIA and DIPHOX, and in particular in the distributions of diphoton p_T and $\Delta\phi$ between the two photons.

We investigated the effects of applying instead a two-dimensional reweighting of PYTHIA to the DIPHOX prediction for diphoton invariant mass and diphoton p_T. The weights are shown in the upper left plot of Figure A.1. Note that there are insufficient PYTHIA events for large diphoton p_T, so above a certain (mass-dependent) threshold, the weights are held constant as a function of p_T.

The upper right plot of Figure A.1 shows that the diphoton invariant mass spectrum is essentially identical for either the 1-D or 2-D reweightings. The lower plots show that the 2-D reweighting improves the agreement between DIPHOX and reweighted PYTHIA for diphoton p_T and $\Delta\phi$. The agreement for large p_T is limited by using a constant weight there, but the agreement for $p_T < 100$ GeV, which accounts for 99% of the events, is good.

The diphoton p_T and $\Delta\phi$ distributions are shown in Figure A.2 and A.3 for p17

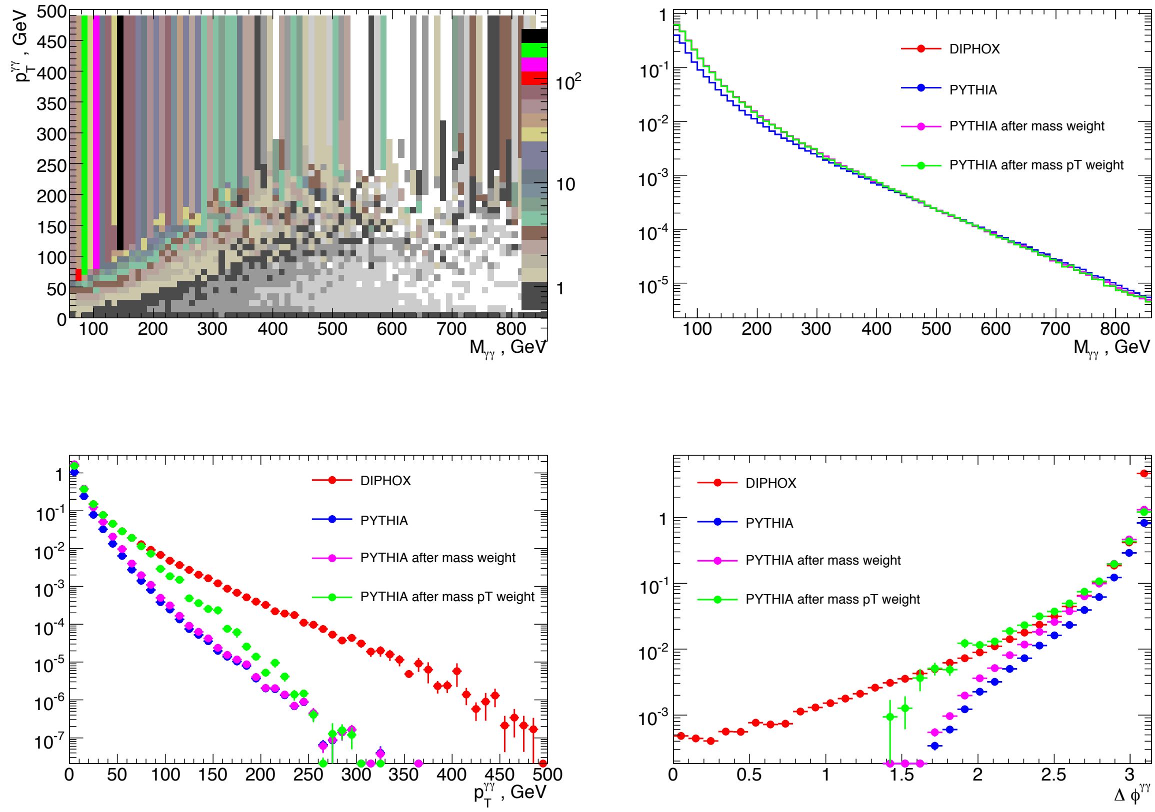

Figure A.1: 2D weighting ($M_{\gamma\gamma}$) vs $p_T^{\gamma\gamma}$, and DIPHOX/PYTHIA comparison after mass only weighting or mass-p_T 2D weighting.

and p20 Category II events, using the 2-D reweighting. The impact on the invariant mass spectrum is negligible, and the variation of the background as determined in the fit to the control region is within the fit errors.

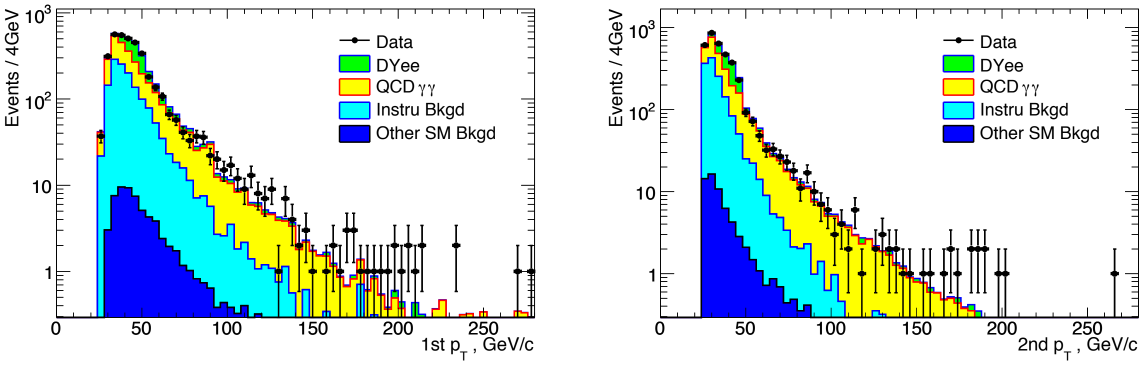

(a) leading p_T

(b) subleading p_T

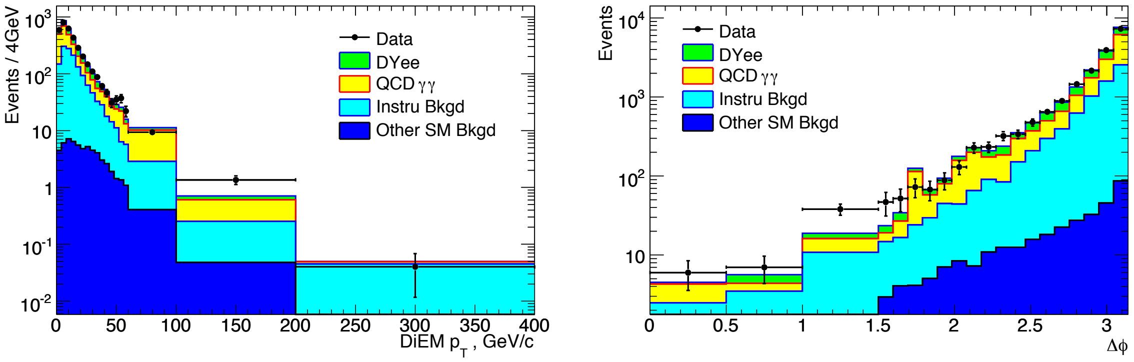

(c) q_T

(d) $\Delta\phi$

Figure A.2: Leading and subleading p_T, $q_T^{\gamma\gamma}$ and $\Delta\phi^{\gamma\gamma}$ distributions for p17 Category II events after the 2-D weighing.

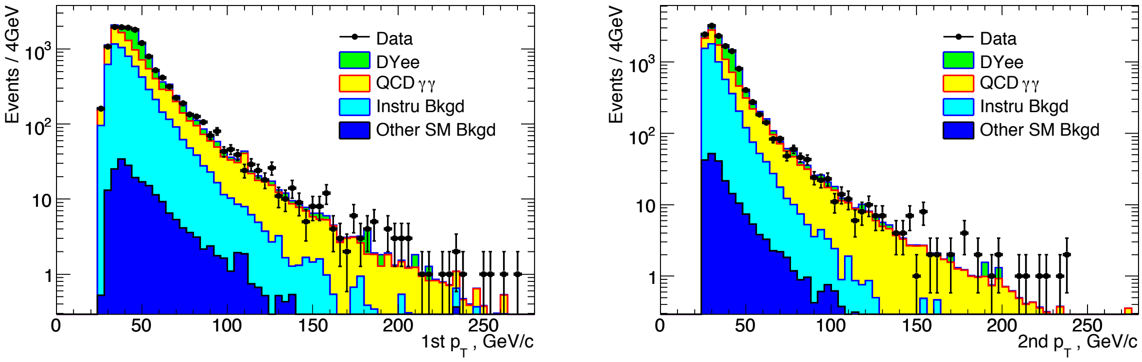

(a) leading p_T

(b) subleading p_T

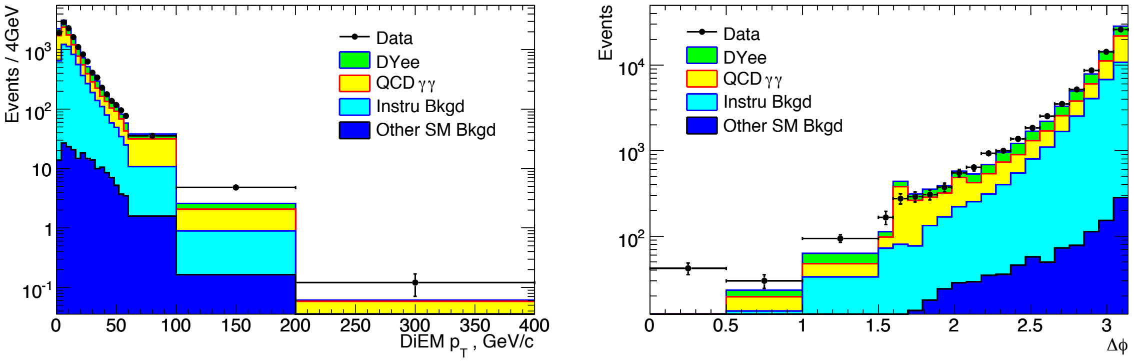

(c) q_T

(d) $\Delta\phi$

Figure A.3: Leading and subleading p_T, $q_T^{\gamma\gamma}$ and $\Delta\phi^{\gamma\gamma}$ distributions for p20 Category II events after the 2-D weighing.

Appendix B

Backup Plots

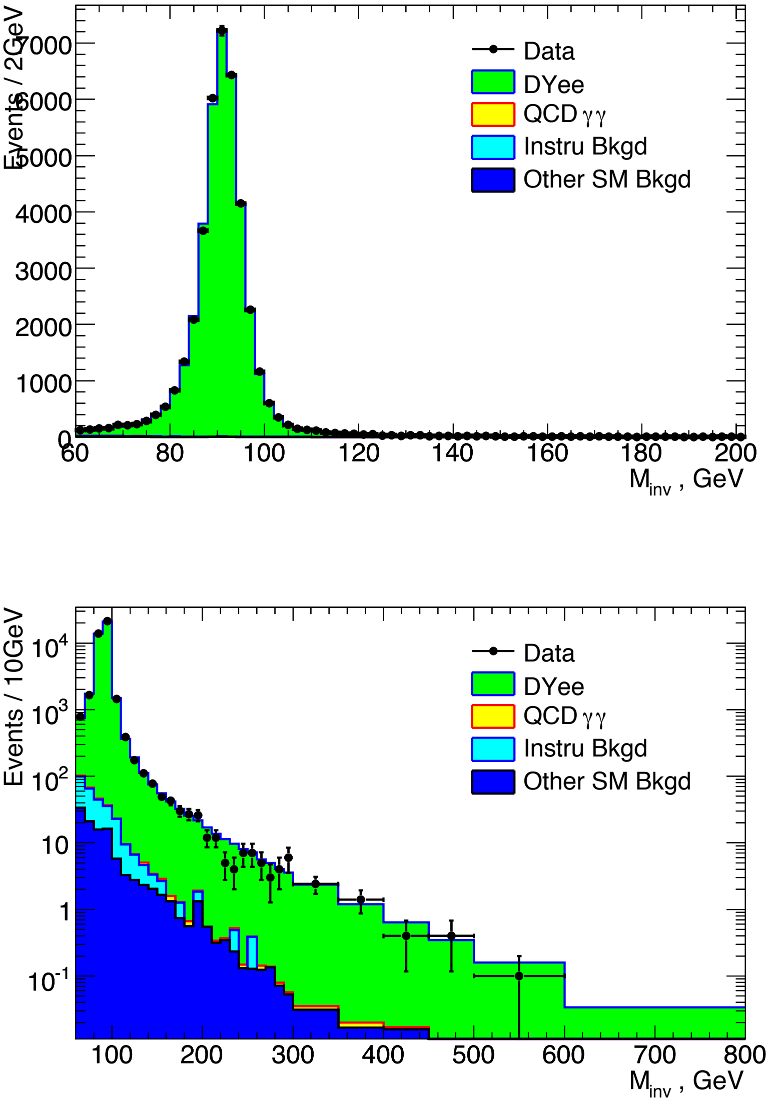

Figure B.1: p17 Category I invariant mass spectrum.

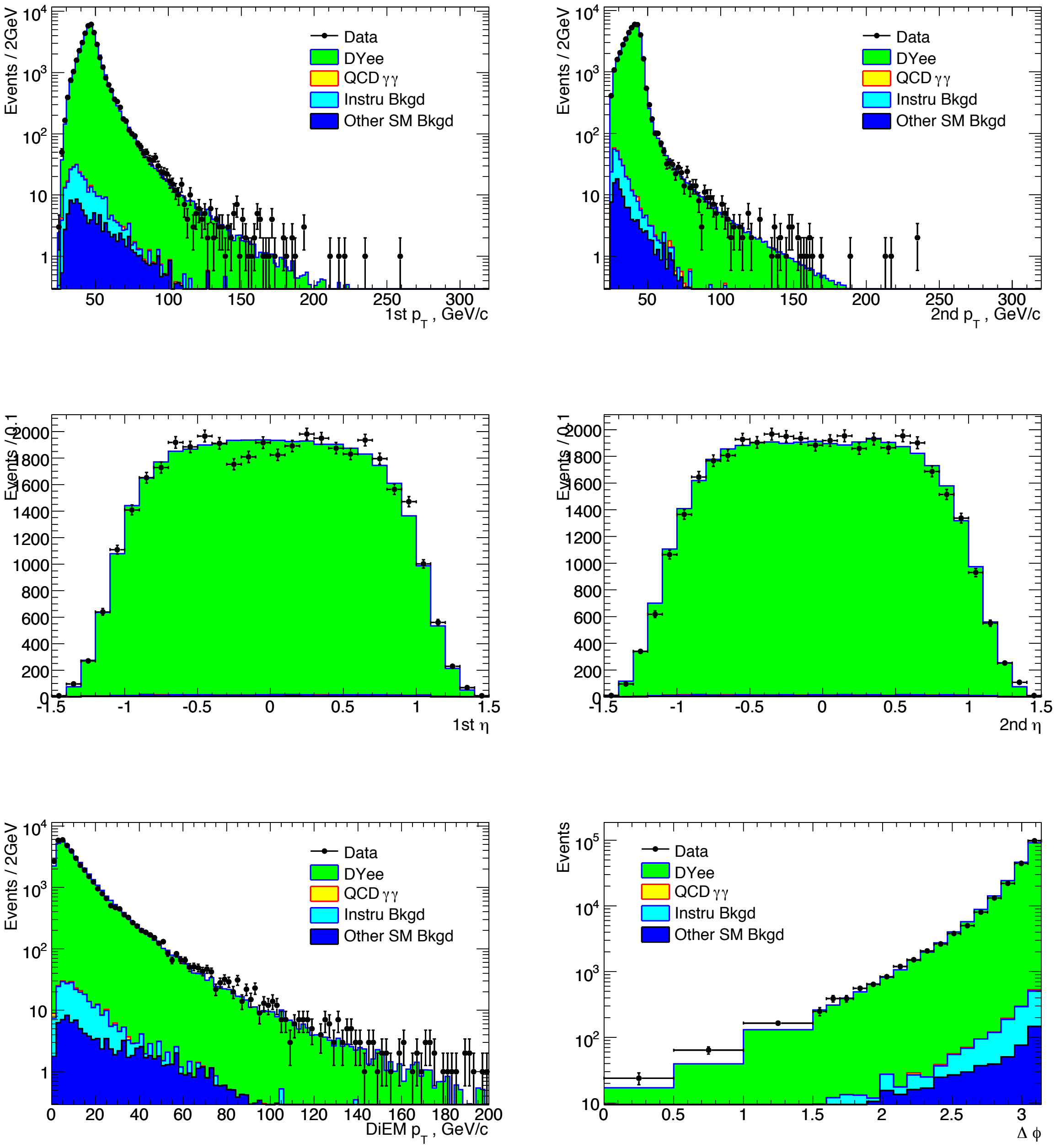

Figure B.2: Various distributions for p17 Category I events.

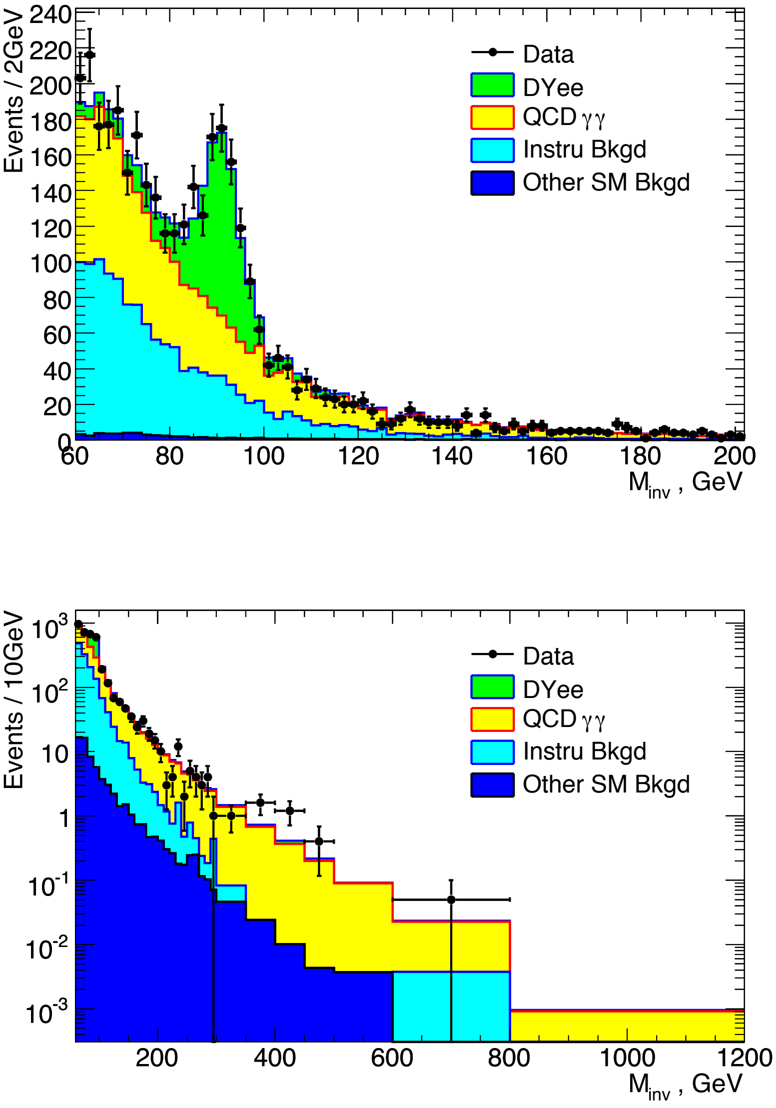

Figure B.3: p17 Category II invariant mass spectrum.

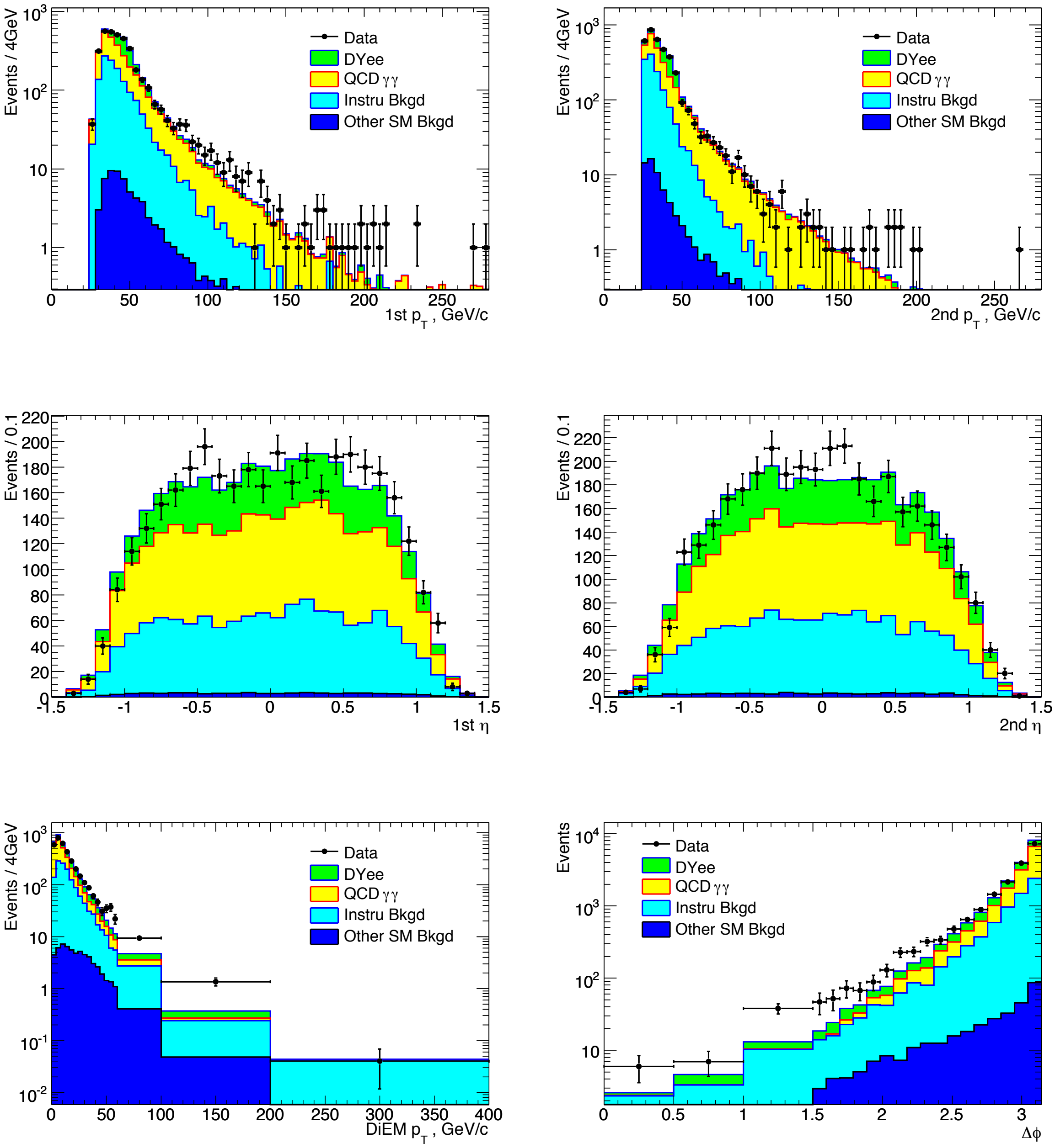

Figure B.4: Various distributions for p17 Category II events.

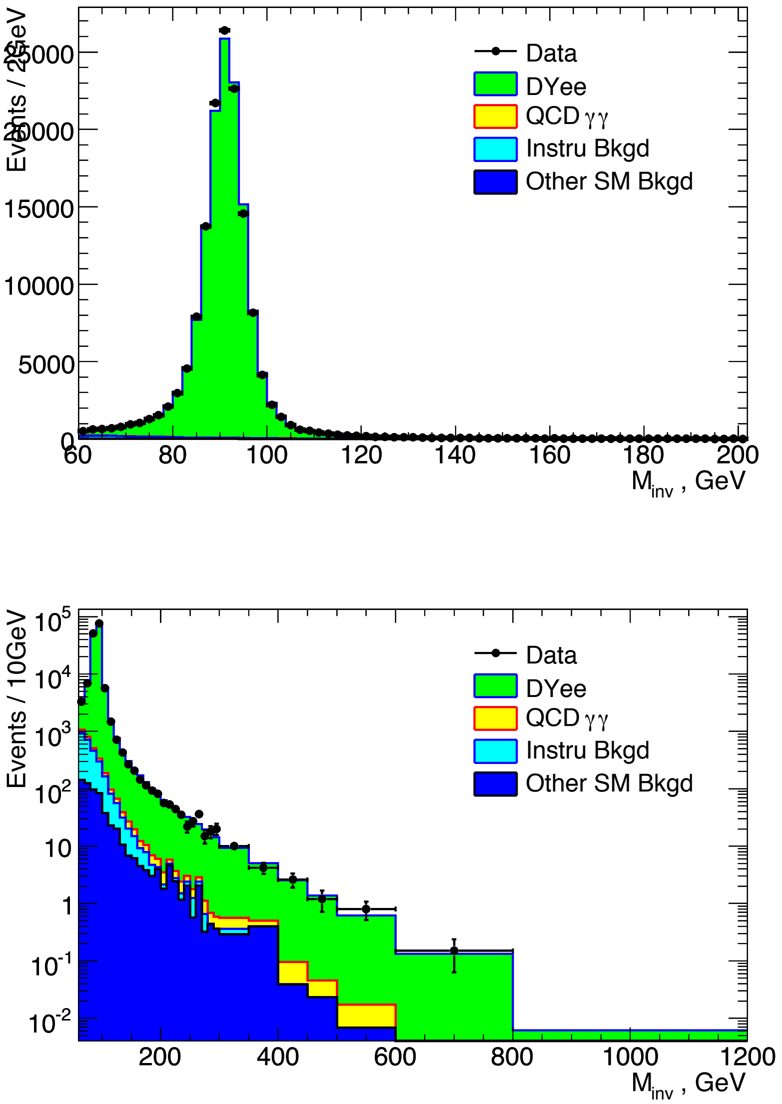

Figure B.5: p20 Category I invariant mass spectrum.

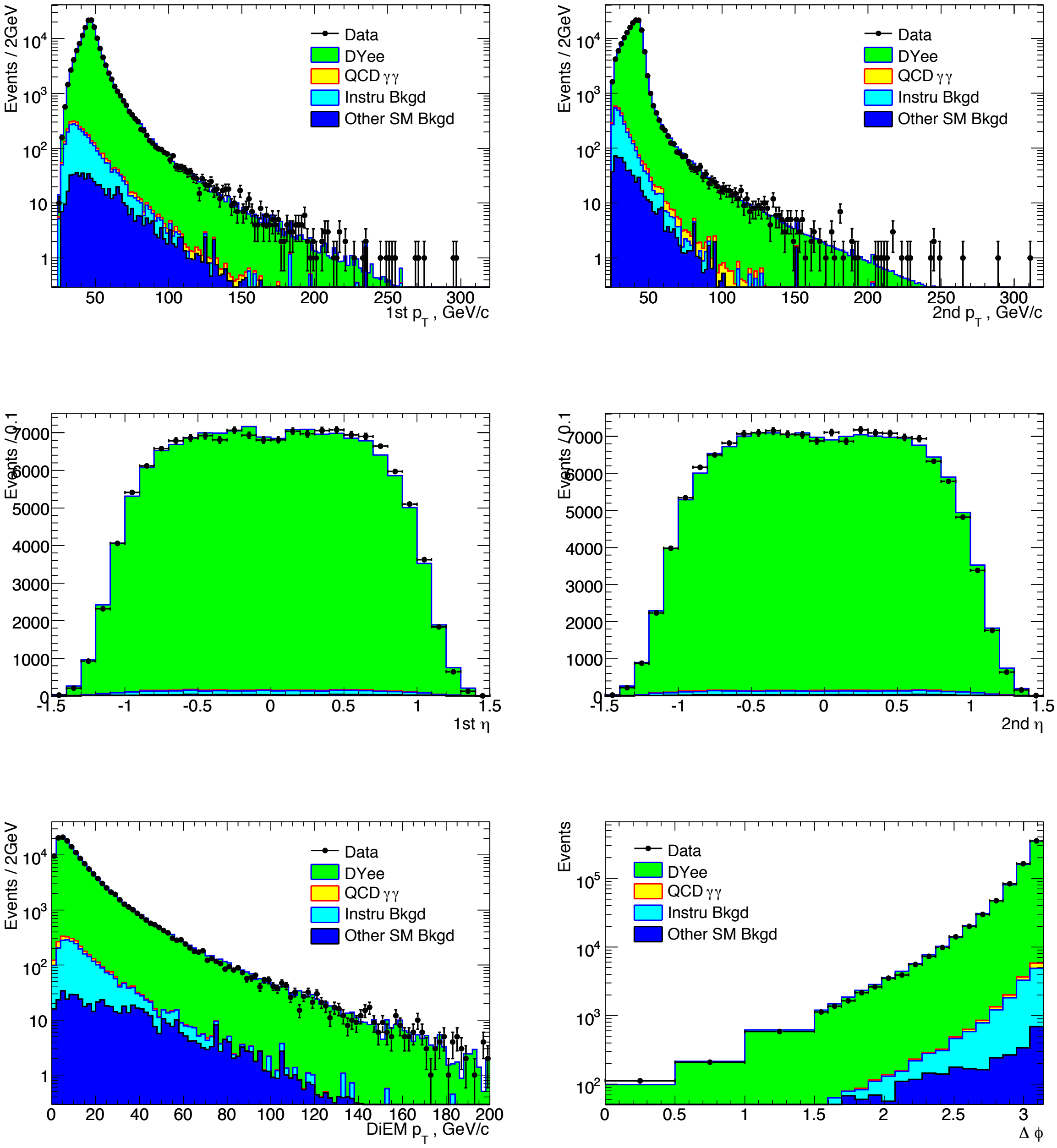

Figure B.6: Various distributions for p20 Category I events.

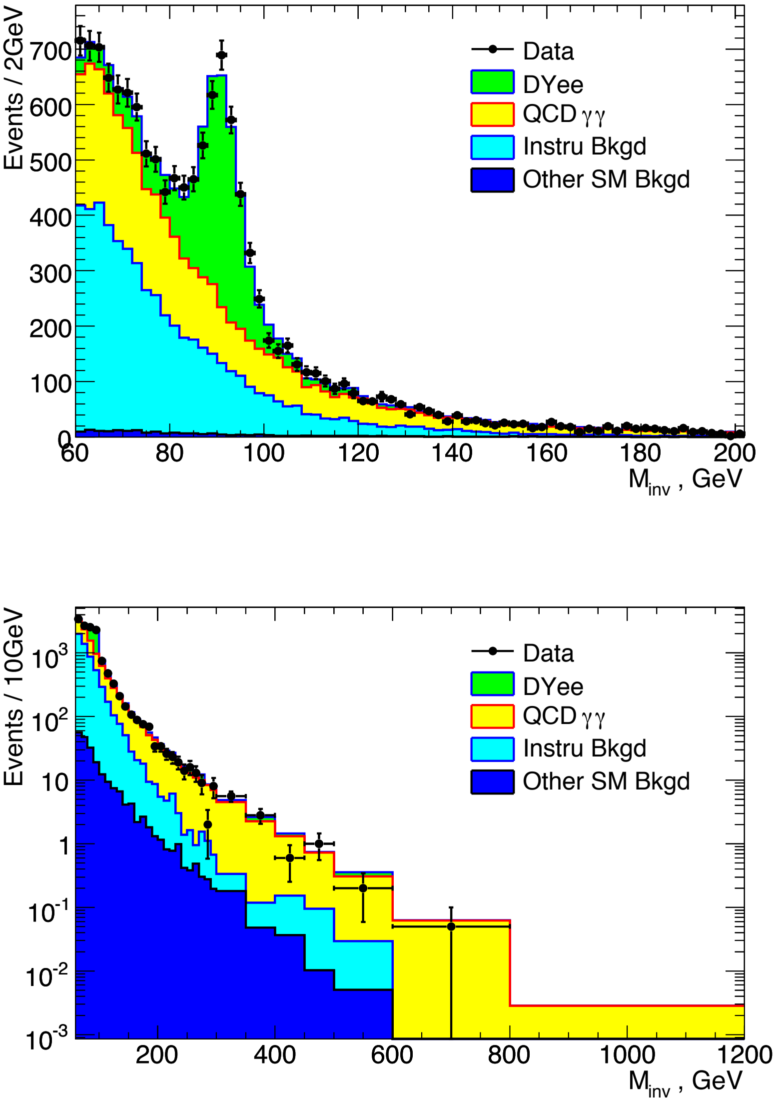

Figure B.7: p20 Category II invariant mass spectrum.

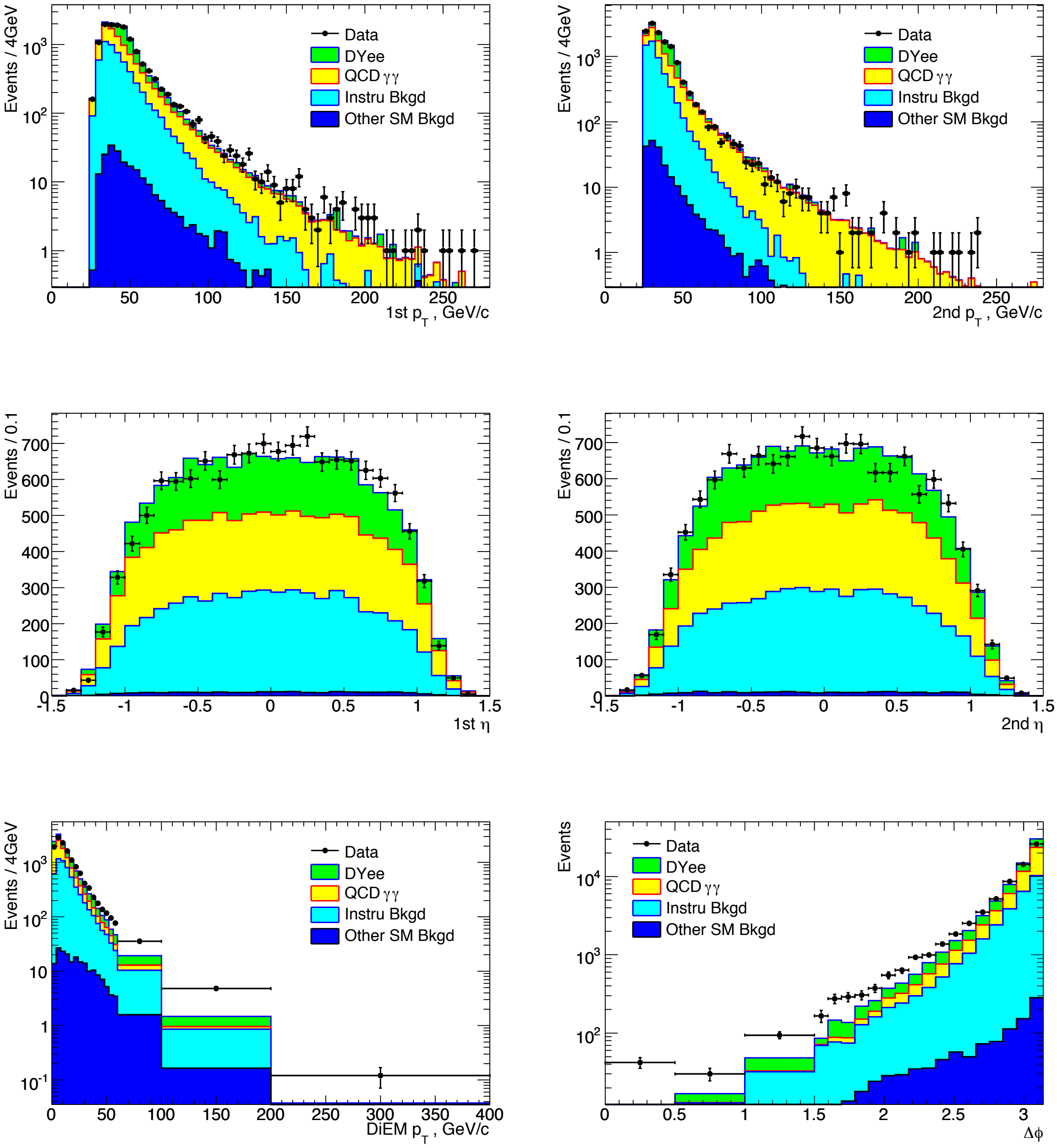

Figure B.8: Various distributions for p20 Category II events.

Appendix C

Other Versions of the Limit Plots

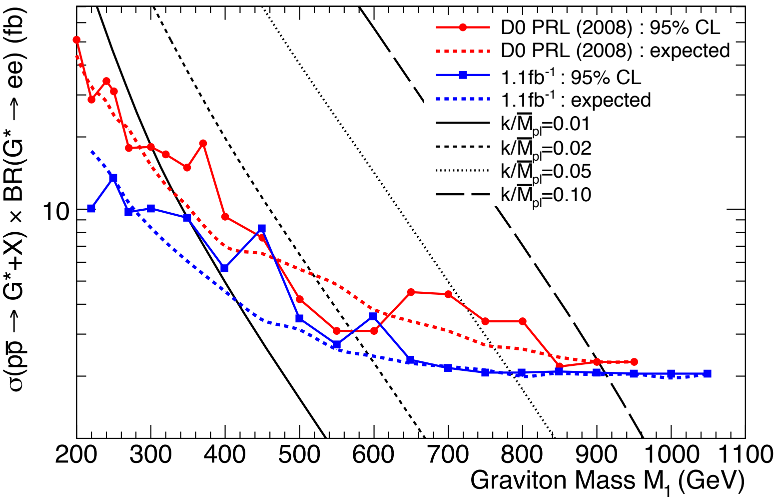

Figure C.1: 95% CL upper limit on $\sigma \cdot BR(p\bar{p} \rightarrow G^* \rightarrow e^+e^-)$ and $k/\overline{M}_{\mathrm{Pl}}$ versus graviton mass from 1.1 fb^{-1} of data. The limits are shown separately for the previous published results and that from the strategy used in this analysis.

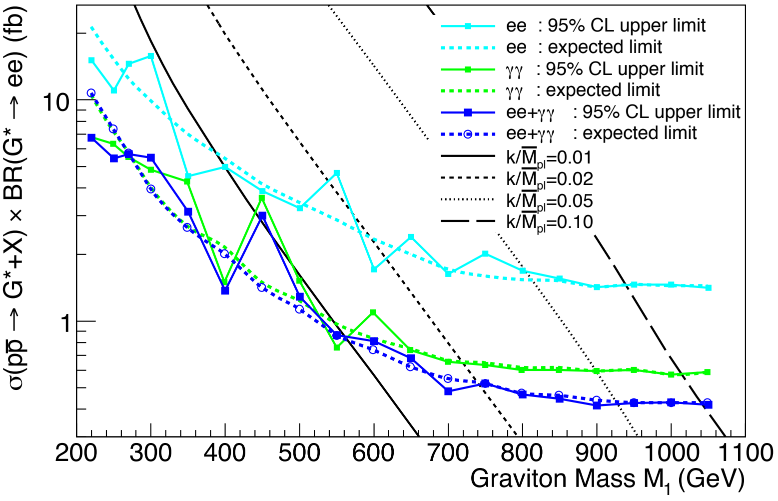

Figure C.2: 95% CL upper limit on $\sigma \cdot BR(p\bar{p} \rightarrow G^* \rightarrow e^+e^-)$ and $k/\overline{M}_{\rm Pl}$ versus graviton mass from 5.4 fb^{-1} of data. The limits are shown separately for Category I, Category II and the combination of the two categories.

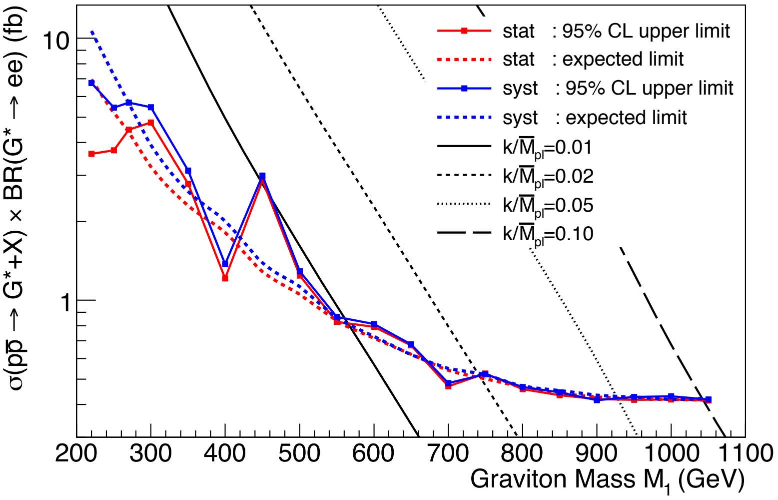

Figure C.3: 95% CL upper limit on $\sigma \cdot BR(p\bar{p} \rightarrow G^* \rightarrow e^+e^-)$ and $k/\overline{M}_{\rm Pl}$ versus graviton mass from 5.4 fb^{-1} of data. The limits are shown separately for statistical errors only and for full (ie. statistical plus systematic) errors.

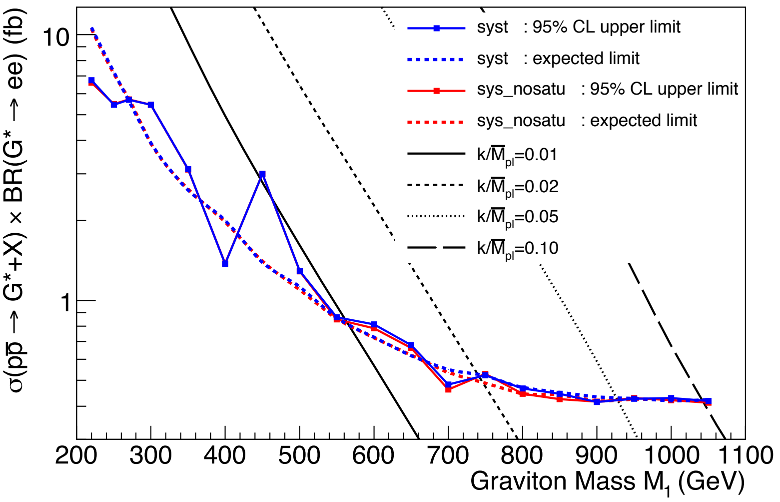

Figure C.4: 95% CL upper limit on $\sigma \cdot BR(p\bar{p} \rightarrow G^* \rightarrow e^+e^-)$ and $k/\overline{M}_{\mathrm{Pl}}$ versus graviton mass from 5.4 fb^{-1} of data. The limits are shown for the final analysis including saturation effects as well as for the case if the saturation effects were ignored.

Appendix D

Angular distribution

In addition to being detectable via a narrow resonance signal in the invariant mass spectrum, the RS graviton would distinguish itself in the final state angular distribution, due to its spin-2 nature. Table 2.1 lists the expected angular distributions for various RS graviton production and decay modes, as well as for the DY *ee* background process. These distributions are plotted in Figure 2.6.

One sees that most of the discrimination power between signal (a,b,c) and background (d) lies in the high $\cos(\theta^*)$ region. However, by requiring both EM objects in the CC region, the differences in angular distribution between signal and background are significantly diluted. Figure D.1 shows the final state angular distribution for diEM invariant mass above 200 GeV, separately for Category I and Category II.

Given the rather modest differences between the signal and background angular distributions after cuts, as evidenced in Figure D.1, one would not expect a very large improvement in the sensitivity by including the angular distribution along with the invariant mass distribution in the limit setting. To include angular distribution, a two dimensional distribution (invariant mass vs $cos\theta^*$) is created as input to Collie. For the background angular distribution, each background source is normalized according to the invariant mass fitting described in this analysis. Figure D.2 shows the exclusion limits with and without including angular information, which indeed con-

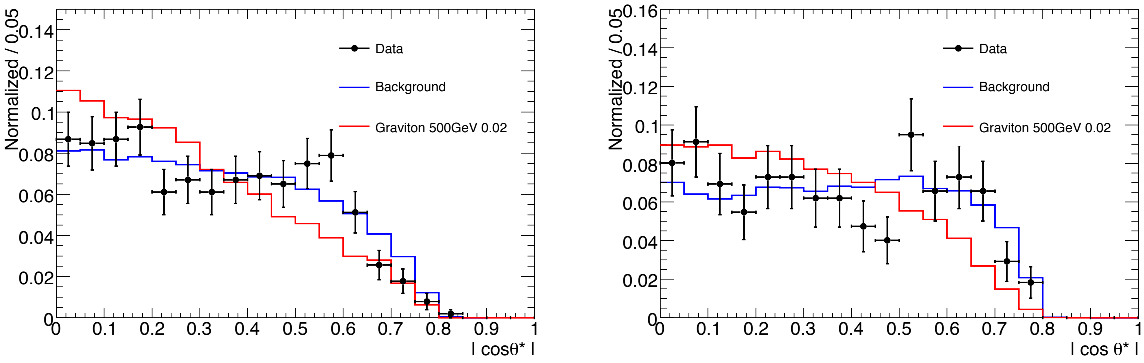

(a) Category-I

(b) Category-II

Figure D.1: Angular distribution for CC-CC events with invariant mass greater than 200 GeV in Category I (upper plot) and Category II (lower plot).

firms that including the angular information does not lead to a large improvement. In Figure D.2, only the statistical error on the angular information is considered. Any improvement would be even further reduced once the systematic errors on the angular distribution are included.

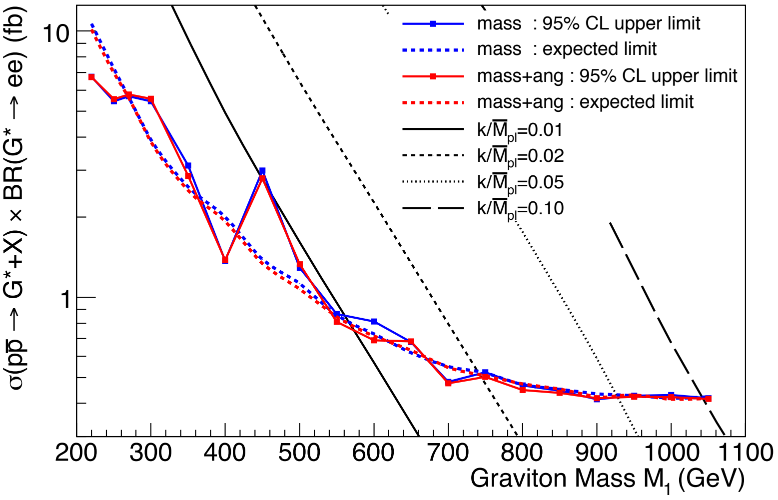

Figure D.2: 95% CL upper limit on $\sigma \cdot BR(p\bar{p} \rightarrow G^* \rightarrow e^+e^-)$ and $k/\overline{M}_{\rm Pl}$ versus graviton mass from 5.4 fb^{-1} of data. The limits are shown separately for the analysis using only the invariant mass distribution and for the case of using both the mass and angular distributions.